

Rift and salt-related multi-phase dolomitization: example from the northwestern Pyrenees

Motte Geoffrey ^{1,2,*}, Hoareau Guilhem ¹, Callot Jean-Paul ¹, Revillon Sidonie ³, Piccoli Francesca ⁴, Calassou Sylvain ², Gaucher Eric C. ²

¹ Univ Pau & Pays Adour, UMR5150, LFCR, TOTAL,UPPA E2S, F-64000 Pau, France.

² CSTJF, TOTAL, F-64018 Pau, France.

³ Inst Univ Europeen Mer, SEDISOR, F-29280 Plouzane, France.

⁴ Univ Bern, Inst Geol Sci, CH-3012 Bern, Switzerland.

* Corresponding author : Geoffrey Motte, email address : geoffreymotte@gmail.com

Abstract :

The Meillon (Callovo-Oxfordian) and Mano (Tithonian) Formations are dolomitized carbonate reservoirs that actively produce oil and gas (Aquitaine Basin, France). In this study, the dolomitization conditions of their counterparts exhumed in the northwestern Pyrenees are detailed using a combination of field observations, petrography, fluid inclusion microthermometry, elemental and isotopic geochemistry, and carbonate U-Pb geochronology. Dolomitization occurred in several stages spanning from the Neocomian (pre-rift) to the Albian (syn-rift, associated with mantle exhumation and active salt tectonics). Both formations were first massively dolomitized in near-surface to shallow burial conditions during the Berriasian-Valanginian, likely triggered by the influx of marine-derived waters. Between the Barremian and the Albian, the Early Cretaceous rifting caused the upward influx of hot fluids associated with the partial to complete recrystallization of the initial dolomites. During the Albian, subsequent dolomites precipitated in both formations as high-temperature ($T > 160$ degrees C) vein and pore-filling cement. Distinct fluid inclusion chlorinities and rare earth element patterns between the Meillon and Mano Formations point to fluid compartmentalization during this stage. Whereas dolomite cements indicate the involvement of evaporite-derived brines in the Meillon Formation, precipitation was likely related to clay derived water in the Mano Formation. Lastly, a final episode of dolomite cementation occurred only in the vicinity of faults and volcanic intrusions during the Albian when the highest temperatures were recorded in both formations ($T > 250$ degrees C). These saddle dolomites precipitated from hydrothermal water with a mixture of mantle, crustal-, and evaporite-derived waters channeled by faults and active diapirs. Subsequent quartz and calcite cement precipitation reveals a temperature decrease in a post-rift to inversion setting (post-Cenomanian) and indicates fluid compartmentalization between both formations. This study highlights the major control exerted by rifting, combined with the presence of diapiric salt, on dolomitization, making carbonate platforms of modern salt-rich passive margins potential targets for exploration.

Highlights

► The northwestern Pyrenean carbonates were affected by multi-phase dolomitization. ► U–Pb dating and SIMS with a conventional diagenetic approach highlight the control exerted by rifting and salt tectonics. ► Different fluids such as marine-, evaporite-, crustal-, mantle-, and clay-derived waters were involved in dolomitization. ► The distinct diagenetic evolution of the Meillon and Mano Formations reveals the presence of fluid compartmentalization.

Keywords : Carbonate diagenesis, Dolomite, Breccias, Hydrothermalism, U-Pb dating, Hyperextension, Salt tectonics, Jurassic

Dolomitization processes have been the subject of numerous studies in the last few decades, driven by the large number of hydrocarbon reservoirs made of dolomitized carbonate platforms (Braithwaite et al., 2004; Duggan et al., 2001; Nader and Swennen, 2004; Warren, 2000; White and Al-Aasm, 1997; Wierzbicki et al., 2006; Zenger and Dunham, 1980). Most investigations into the mechanisms responsible for dolomite precipitation, either as a cement or as a calcite replacement, are based on the study of ancient examples with a predominance of carbonate platforms (Barale et al., 2016; Barbier et al., 2015; Carmichael et al., 2008; Martín-Martín et al., 2015; Sharp et al., 2010). This is due to the absence of modern analogues of platforms impacted by massive dolomitization as well as the difficulty of precipitating dolomite at low temperatures in the laboratory within a reasonable timescale (Land, 1998, 1980). Despite the variety of genetic interpretations, these diagenetic studies generally agree that the main parameters required for dolomitization are (1) good rock permeability that allows (2) a high water-rock ratio and (3) the input of Mg into the system (Hardie, 1987; Jonas et al., 2015; Kaczmarek and Sibley, 2011; Land, 1985; Lovering, 1969; Machel and Mountjoy, 1986; Sibley et al., 1994). The combination of these factors results in

a variety of dolomitization models (see [Machel, 2004](#); [Warren, 2000](#)). Examples of dolomitization are restricted to a single event either in an ancient carbonate platform with a well-known geodynamic evolution or in a modern carbonate platform, which provides the opportunity to identify the key control factors responsible for this diagenetic transformation and thus predict the distribution of dolomite in the carbonate platform ([Adam and Rhodes, 1960](#); [Barbier et al., 2015, 2012, 2011](#); [Butler et al., 1982](#); [Choquette and Hiatt, 2008](#); [Deffeyes et al., 1965](#); [Illing, 1964, 1959](#); [Land, 1973](#); [Sharp et al., 2010](#); [Spencer-Cervato and Mullis, 1992](#); [Stoakes, 1987](#); [Wendte et al., 1998](#)). In recent decades, many authors have described cases of pervasive dolomitization, which tends to be multi-phased, first relating to seawater in a near-surface to shallow burial environment and then caused by hydrothermal fluids channeled by structural pathways ([Beckert et al., 2015](#); [Biehl et al., 2016](#); [Breesch et al., 2010](#); [Cantrell et al., 2004](#); [Di Cuia et al., 2011](#); [Garaguly et al., 2018](#); [Guo et al., 2016](#); [Haeri-Ardakani et al., 2013a](#); [Lukoczki et al., 2018](#); [Nader et al., 2004](#); [Tortola et al., 2020](#); [Ye et al., 2019](#)). In these numerous studies, temperature is one of the most critical parameters in the dolomitization reaction.

The foothills of the northwestern Pyrenees (southern Aquitaine basin) provide good examples of dolomitized carbonate platforms, which were used in the exploration of major oil and gas prospects in the 1950s, including the world-renowned Lacq gas field ([Biteau et al., 2006](#)). The platform contains two dolomite reservoirs deposited from the Bathonian to the Oxfordian (Meillon Formation) and during the Tithonian (Mano Formation). Their conditions of dolomitization, which were poorly characterized ([Biteau et al., 2006](#); [Grimaldi, 1988](#); [Péré, 1987](#)), have been recently revisited by [Elias Bahnan \(2019\)](#), [Renard et al. \(2018\)](#), and [Salardon et al. \(2017\)](#). These studies were accompanied by a complete reevaluation of the geodynamic evolution of the Pyrenees, highlighting the importance of Cretaceous rifting ([Jammes et al., 2010a, 2009](#); [Lagabrielle and Bodinier, 2008](#); [Masini et al., 2014](#); [Tugend et al., 2015](#) and many other studies) as the source of anomalous thermal regimes ([Clerc et al., 2015](#); [Hart et al., 2017](#); [Incerpi et al., 2020](#); [Jourdon et al., 2020](#); [Lagabrielle et al., 2016](#);

Lescoutre et al., 2019; Saspiturry, 2019; Vacherat et al., 2014). The inheritance of salt tectonic structures and the role played by salt at various scales were also emphasized in recent studies (Izquierdo-Llavall et al., 2020; Jourdon et al., 2020; Labaume and Teixell, 2020).

This Jurassic carbonate platform crops out in the *Chaînons Béarnais*, which constitute a succession of E-W-oriented salt-cored anticlines with several salt diapirs and ridges (Izquierdo-Llavall et al., 2020; Labaume and Teixell, 2020). In the *Chaînons Béarnais*, the dolomitization of the peritidal deposits that make up the Mano Formation is interpreted as occurring in several stages, beginning with an early limestone replacement followed by a dolomite cementation associated with tectonic fracturing and meteoric water circulation (Biteau et al., 2006; Elias Bahnan, 2019; Grimaldi, 1988). The Meillon Formation was also affected by multi-phase dolomitization with a complete replacement of the barrier-facies limestones followed by cementation associated with brecciation and fracturing at high temperatures (Péré, 1987). Very recently, Salardon et al. (2017), Incerpi et al. (2020), and Corre et al. (2018) demonstrated the role played by extensive hot fluid circulation during the Cretaceous rifting phase. As a result of these events, the two reservoirs present a fairly similar diagenetic evolution despite their distinct sedimentological facies (Grimaldi, 1988; Péré, 1987; Salardon et al., 2017). Nonetheless, the mechanism and origin of each dolomite event have yet to be studied in detail.

Using detailed mapping and petrography as well as conventional and more sophisticated analytical techniques such as carbonate U-Pb dating and secondary ion mass spectrometry (SIMS), this paper updates the diagenetic evolution of the northwestern Pyrenean Jurassic carbonate platform based on the study of the northernmost and most prominent ridge of the *Chaînons Béarnais*: the Mail Arrouy. The aims of this study are as follows: (1) to detail the diagenetic evolution of this carbonate platform, especially at the reservoir scale; (2) to unravel the mechanisms and fluids responsible for each dolomitization event; and (3) to assess the sedimentological and structural controls affecting the

precipitation of dolomite.

2. Geological setting and stratigraphic framework

The Pyrenean orogen is an 450 km long E-W trending belt resulting from the N-S convergence of the European and Iberian Plates from the Late Santonian to the Miocene (Choukroune, 1992; Gong et al., 2008; Mouthereau et al., 2014; Puigdefàbregas and Souquet, 1986; Rosenbaum et al., 2002; Sibuet et al., 2004; Tugend et al., 2014). Separating the two foreland basins (Aquitainian and Ebro Basins), this ridge is subdivided into three structural domains: the North Pyrenean Zone comprised of pre-orogenic Paleozoic and Mesozoic deposits; the Axial Zone represented by Paleozoic rocks; and the South Pyrenean Zone formed by pre-rift to syn-orogenic Mesozoic and Cenozoic deposits (Fig. 1A; Choukroune, 1976). The Pyrenees exhibit a shortening gradient decreasing from E to W, which preserves the pre-orogenic structure of the western part (Masini et al., 2014; Mouthereau et al., 2014; Muñoz, 1992; Vergés et al., 1995). The Jurassic dolomite Meillon and Mano reservoir units crop out in the *Chaînon Béarnais*, located in the western North Pyrenean Zone (Fig. 1A).

The *Chaînon Béarnais* are the first landforms of the northwestern Pyrenees, located about 30 km from the Lacq gas field. These ridges include three salt-cored anticlines with an E-W trend. These structures that affect the Mesozoic deposits are interpreted as being partly inherited from pre- to syn-rift salt tectonics (Canérot et al., 2005; Izquierdo-Llavall et al., 2020; Labaume and Teixell, 2020; Lenoble and Canérot, 1992). The majority of the structural geometry of the most spectacular folds occurred in response to downbuilding in the salt and gravitational gliding of the cover along the margin slope prior to the shortening phase (Izquierdo-Llavall et al., 2020; Labaume and Teixell, 2020). This study focuses on the northernmost ridge, the Mail Arrouy Ridge, which was most affected by this shortening during the Eocene (Fig. 1B). This north-dipping monoclinical structure extends over 15 km between the Ossau and Aspe Valleys. It presents deposits spanning from the Triassic (ante-rift) to the

Cenomanian (post-rift). Above the Upper Triassic deposits composed of evaporites, clays, and ophites, more than 1000 m of carbonates were deposited in a relatively stable tectonic context (James, 1998; Lenoble, 1992; Puigdefàbregas and Souquet, 1986). During the Lias, the depositional environment evolved from continental to open marine, with deposits passing from breccias during the Hettangian to belemnite marls and limestones during the Toarcian–Aalenian (Aussurucq Limestones; Canérot et al., 1990; Fauré, 2002; James, 1998; Lenoble, 1992; Fig. 1C). From the Bajocian to the early Bathonian, the morphology of the carbonate platform gradually shifted from a ramp to a rimmed shelf at the base of the dolomite Meillon Formation. The recurrence of a ramp morphology took place during the deposition of the end of the Meillon Formation and the Kimmeridgian Lons limestone Formation (James, 1998; Lenoble, 1992; Péré, 1989). During the Tithonian, the development of the dolomite Mano Formation, characterized by peritidal to supratidal environment deposits, was related to a widespread regression. The formation emerged in the late Tithonian to the Neocomian (Grimaldi, 1988), as evidenced by the presence of bauxites (Canérot et al., 1999; Combes et al., 1998; Grimaldi, 1988). The exposure was generalized in the *Chaînon Béarnais*, and increased southwestward, as evidenced by incision variations in the Upper Jurassic deposits (Fig. 1B; Castéras, 1970). Emersion probably resulted from both the relative sea-level fall and the regional uplift due to asthenospheric upwelling (Cox, 1989; Hallam, 2001; Haq et al., 1987; Ziegler and Cloetingh, 2004). In addition, salt tectonics, initiated at the beginning of the extension, resulted in the reactive salt diapir and ridge development, associated with the strong folding of the pre-rift deposits and favoring local emersion (Canérot et al., 2005; Canérot and Lenoble, 1993; Izquierdo-Llavall et al., 2020; James and Canérot, 1999). From the Barremian to the Aptian, transgression took place from N to S, progressively flooding the emerged deposits. In the Mail Arrouy, it was first associated with the development of Annelid Limestones above the Jurassic deposits (Grimaldi, 1988; Lenoble, 1992), followed by the deposition of the Sainte-Suzanne Marls (Early Aptian), the ultimate seal of the Mano Formation (Biteau et al., 2006). All the Cretaceous deposits were controlled by a major rifting episode resulting from the rotation of the Iberian plate (Choukroune et al., 1973; Gong et al.,

2008; Rosenbaum et al., 2002; Sibuet et al., 2004). The crust was first stretched and thinned by the ductile deformation of the lower crust, thus creating sedimentary space for the Aptian carbonates (Clerc et al., 2016; Clerc and Lagabriele, 2014; Jammes et al., 2010b, 2009; Masini et al., 2014; Saspiturry et al., 2019). In the *Chaînons Béarnais*, the Early Aptian Sainte-Suzanne Marls are overlaid by a Late Aptian shallow carbonate platform mainly consisting of rudist build-ups (so-called Urgonian Limestones). These massive carbonates pass laterally to the Aptian Black Marls. From the Albian to the Cenomanian, the rifting led to the extreme thinning of the crust associated with mantle exhumation (Clerc and Lagabriele, 2014; Corre et al., 2016; Jammes et al., 2010b, 2009; Lagabriele et al., 2010; Lagabriele and Bodinier, 2008; Masini et al., 2014; Tugend et al., 2014). The basin subsided heavily, with the widespread deepening of the depositional environments passing from reef to deep basinal deposits. From the Albian to the Maastrichtian, about 4000 m of turbidite deposits accumulated (Castéras et al., 1970). The thinning of the crust was associated with high geothermal gradients, causing high temperatures, low pressure metamorphism, and alkaline volcanism (Albarède and Michard-Vitrac, 1978; Azambre et al., 1992; Azambre and Rossy, 1976; Clerc et al., 2015; Ducoux et al., 2019; Golberg and Leyreloup, 1990; Hart et al., 2017; Izquierdo-Llavall et al., 2020; Lagabriele et al., 2016; Lescoutre et al., 2019; Vacherat et al., 2016, 2014). From the early rifting at 125 Ma to the mantle exhumation, the thermal gradients increased by up to 80–100°C/km in the central part of the basin (Hart et al., 2017). Starting during the Campanian, the convergence of the European and Iberian Plates resulted in a collision that reached a paroxysm during the Eocene (Choukroune, 1992; Choukroune et al., 1990; Mouthereau et al., 2014; Puigdefàbregas and Souquet, 1986; Teixell et al., 2018, 2016). The thermal gradients remained high during the post-rift and convergence stages. The thermal relaxation only occurred during the collision (50 Ma; Vacherat et al., 2014). During the contraction phase, tectonic lenses composed of crustal and mantle materials were incorporated into the Pyrenean orogenic wedge, leading to the exhumation of mantle bodies as in Urdach, *Turon de la Técoùère*, and Lherz (Lagabriele et al., 2010).

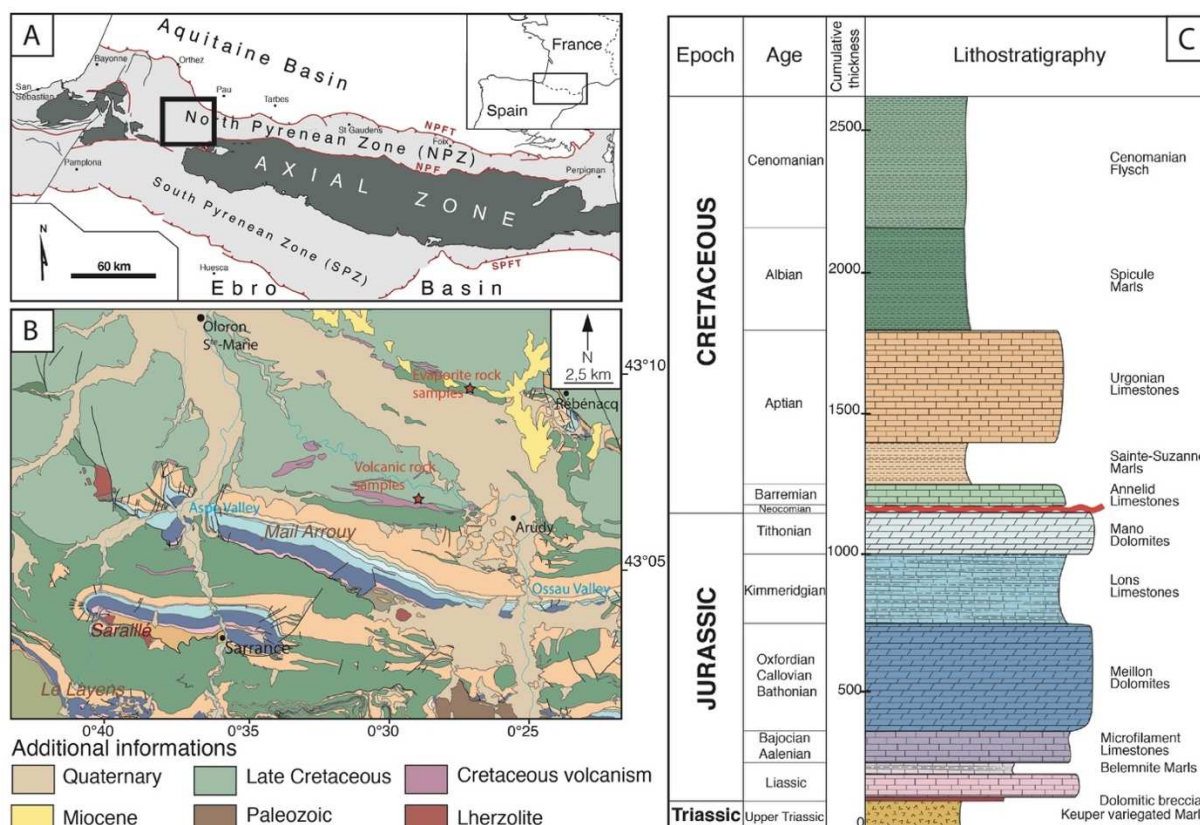


Fig. 1 A) Main structural domains of the Pyrenees with the location of the *Chaînon Béarnais* (after Clerc et al., 2016b); B) Geological map of the *Chaînon Béarnais* (modified after Castéras, 1970); the colors correspond to the lithostratigraphic log; C) Simplified lithostratigraphic log showing the different stratigraphic formations present in the Mail Arrouy.

3. Methods

3.1. Field observations and sampling

Based on previous research (Castéras et al., 1970; Grimaldi, 1988; James, 1998; Lenoble, 1992) and our own observations, a 10 km² mapping of the study area was carried out in the Mail Arrouy, including the boundaries of sedimentary formations, faults, magmatic dykes and sills, and breccia bodies (Fig. 2). The breccia description was based on Morrow (1982). Four stratigraphic sections were logged to constrain the lithologies of each formation. The sampling (n = 242) focused on the entire Mano and Meillon Formations outcropping in the Mail Arrouy, including the various brecciated bodies in the vicinity of faults. To obtain reference geochemical values, samples of volcanic rocks and evaporites were also collected (n = 8). A basaltic sill intercalated in the Cretaceous mapped near the Mail Arrouy Ridge was also sampled (Fig. 1B). Due to the lack of outcropping evaporites, we obtained samples

directly from cores provided by Total SA, extracted from the Belair 1 well located 10 km north of the study area (Fig. 1B).

3.2. Analytical techniques

In total, 80 samples were selected for polished thin section preparation. Thin sections were partly stained with alizarin Red S solution to distinguish dolomite from calcite. The petrographic studies were performed using a Nikon Eclipse LV100ND optical microscope at the Laboratoire des Fluides Complexes et leurs Réservoirs (LFCR) (Pau, France). Overall, 50 thin sections were observed under cathodoluminescence (CL) using a Cathodyne system (OPEA) with an operating condition of 15 kV-18 kV and a gun current of 300-350 mA under a 60 mTorr vacuum at the LFCR. The limestone description was based on the Dunham (1962) classification, updated by Embry and Klovan (1971) and Wright (1992). The dolomite textures were described according to Gregg and Sibley (1987).

Fluid inclusion (FI) petrography was performed on 40 doubly-polished thick sections to identify FI assemblages according to Goldstein and Reynolds (1994) for each dolomite and calcite cement. The microthermometric measurement of dolomites only allowed homogenization temperatures to be determined due to the small size of the inclusions (< 5-10 μm). Measurements were performed on a Linkam THMSG600 heating-cooling stage connected to a Nikon Eclipse LV100ND microscope at the LFCR. The equipment was calibrated using the following: (1) synthetic H_2O pure fluid inclusion standard (ice melting ($T_{\text{m ice}}$) at 0.0°C , homogenization temperature (T_{h}) at 374.1°C); (2) synthetic H_2O - CO_2 inclusions (CO_2 melting at -56.6°C , hydrate melting at $+9.9^\circ\text{C}$); and (3) synthetic H_2O - NaCl inclusions (eutectic temperature at -21.2°C). The phase transition temperature had an uncertainty of around ± 1 - 2°C because of the small size of the inclusions.

Due to the lack of $T_{\text{m ice}}$ measurements, Raman spectroscopy was performed to determine the chlorinity of the fluid inclusions (Burke, 2001; Dubessy et al., 2002; Frezzotti et al., 2012). Analyses were performed in the Georessources laboratory (Nancy, France) with a LabRAM HR spectrometer (Horiba Jobin Yvon) equipped with a 600 g.mm^{-1} grating and an

edge filter, as well as an excitation light provided by an Ar⁺ laser at 457 nm at a power of 200 mW. Chlorinity was determined using the calibration of [Caumon et al. \(2013\)](#) following the procedure outlined in [Caumon et al. \(2015\)](#) to avoid the effect of mineral birefringence.

Major element compositions were measured in dolomite and calcite with an electron probe microanalyzer using a CAMECA SX100 from the PLateforme Aquitaine de CARactérisation des MATériaux (Pessac, France). The standard microprobe conditions were 40nA and 20kV using natural (andradite and celsian) and synthetic in-house standards.

Rare earth elements (REE) were measured on three thin sections by LA-ICP-MS with a Resonetics Resolution-SE 193nm excimer laser system equipped with a S-155 large volume constant geometry chamber (Laurin Technic, Australia) at the Institute of Geological Sciences, University of Bern, Switzerland. Four transects were made across the dolomites, covering a total of 26 points in distinctive cement/matrix phases. The laser system was coupled to an Agilent 7900 quadrupole ICP-MS instrument. Samples were ablated in a He atmosphere and the aerosol mixed with Ar carrier gas before being transported to the ICP-MS. Measurement beam size was set at 80 µm, and the surface area of each measurement spot was cleaned with a pre-ablation of four pulses with a larger spot size. Total acquisition time for each analysis was 65 seconds (s), consisting of 30 s of gas background acquired with the laser switched off, 10 s of washout after pre-ablation cleaning, and 25 s of ablation signal. External calibration was performed using trace element-doped basaltic glasses GSD-1g ([Jochum et al., 2010](#)) and NIST 612 ([Jochum et al., 2011](#)), while Mg concentration, preliminarily determined by the electron probe microanalyzer, was used as the internal standard recovery. Standard controls were made every 10 measurements. Data were reduced by employing Iolite Igor Pro (version 7.08). The REE concentrations were normalized to the World Shale Average (WSA) as calculated by [Piper \(1974\)](#).

Bulk stable oxygen and carbon isotopes were analyzed on 13 powdered carbonate samples at the Institut des Sciences de la Terre de Paris (Paris, France). Due to the size of the microdrill bit (800 µm minimum), only four samples corresponded to a single phase of

dolomite, with the others being a mixture of cement and dolomite matrix material. The dolomite samples were reacted under vacuum with 100% phosphoric acid at 70°C for 10 min. CO₂ was purified in an automatic cryogenic trapping system and analyzed on the Kiel IV device coupled to a Delta V Advantage Thermo-Scientific. The measurements were reported as per mil (‰) deviation relative to the Vienna Pee Dee Belemnite (VPDB) standard and normalized to the NBS19 and NBS18. The acid fractionation of [Rosenbaum and Sheppard \(1986\)](#) was applied to the dolomite and [Kim et al. \(2007\)](#) to the calcite.

In situ oxygen and carbon isotope measurements were also performed on six polished and gold-coated thin sections with a SIMS Cameca IMS 1270 located at the Centre de Recherche Pétrographique et Géochemique (Nancy, France). Eight transects were made across calcite and dolomite cements, covering a total of 189 points. To do so, two parallel transects (one for each isotope) were measured for each region of interest. Samples were sputtered with the 10kV Cs⁺ primary beam of 3 (for oxygen) and 2.7 (for carbon) nA intensity focused on 20 µm spots. Secondary negative ions of C and O were accelerated at 10 kV and analyzed at a mass resolution of about 5000 using the circular focusing mode of the IMS 1270 and a transfer optic of 150 µm ([Rollion-Bard et al., 2003](#)). The instrumental mass fractionation was determined using two standards analyzed conventionally for O and C isotopes: an ankerite standard (G119) for the dolomite ($\delta^{18}\text{O}_{\text{SMOW}} = +23.83 \pm 0.28\text{‰}$; $\delta^{13}\text{C}_{\text{VPDB}} = -0.38 \pm 0.17\text{‰}$) and a calcite standard (CC CigA) for the calcite ($\delta^{18}\text{O}_{\text{SMOW}} = +18.94 \pm 0.14\text{‰}$; $\delta^{13}\text{C}_{\text{VPDB}} = +1.04 \pm 0.10\text{‰}$) according to [Rollion-Bard et al. \(2003\)](#). The instrumental stability was verified regularly during each session. In the event of instrumental drift, a linear correction constrained by the difference in the standard value was applied to the measurements. The internal precision for a single measurement was $\pm 0.1\text{--}0.2\text{‰}_{\text{(VPDB)}}$ for ¹³C/¹²C and ¹⁸O/¹⁶O ratios. [Rollion-Bard et al. \(2003\)](#) experimented the reproducibility based on the repeated standard measurements and obtained $\pm 0.4\text{‰}_{\text{(VPDB)}}$ for oxygen and $\pm 0.65\text{‰}_{\text{(VPDB)}}$ for carbon. The bulk values of large areas of cement were used to correct the $\delta^{18}\text{O}$ values obtained by the SIMS of the matrix effects ([Rollion-Bard and Marin-Carbonne,](#)

2011). Regarding the oxygen isotope values obtained by bulk analysis, the SIMS values are outlined in permil deviation from the VPDB standard (‰_{VPDB}).

The $^{87}\text{Sr}/^{86}\text{Sr}$ ratio was performed on 25 microdrilled samples: 18 were from dolomites and calcites in the Mano and Meillon Formations and 7 from volcanic rocks and evaporites. The Sr isotope analyses were performed at the Pole de Spectrométrie Ocean/Institut Universitaire Européen de la Mer (Plouzané, France). The Sr fractions were chemically separated following standard column chemistry procedures (Révillon et al., 2011). The Sr isotope compositions were measured in static mode on a Thermo TRITON and normalized to natural $^{86}\text{Sr}/^{88}\text{Sr} = 0.1194$ and to the standard solution NBS987 (recommended value of 0.710250). The standard deviation for laboratory standards within the samples was less than ± 0.000005 (2σ).

Calcite U-Pb geochronology was conducted via a LA-ICPMS isotope mapping approach at the Institut des Sciences Analytiques et de Physico-Chimie pour l'Environnement et les Matériaux (Pau, France). All the samples were analyzed with a femtosecond laser ablation system (Lambda3, Nexeya, Bordeaux, France) coupled to an ICPMS Element XR (ThermoFisher Scientific, Bremen, Germany) fitted with the jet interface. This method is based on the construction of isotopic maps of the elements of interest for dating (U, Pb, Th) from ablation along lines, with ages calculated from the pixel values (Drost et al., 2018; Hoareau et al., in press). The laser and ICPMS parameters used for U-Pb dating are detailed in the Supplementary Material. Isotope maps were built from linear scans of 1.1 mm length at a repetition rate of 500 Hz. These lines of 25 μm height, separated by a distance of 25 μm , were obtained with a stage movement rate of 25 $\mu\text{m.s}^{-1}$, corresponding to 44 s of analysis per line, followed by 15 s of break. There were 27 to 28 lines, resulting in a total analysis time ranging from 26.5 to 27.5 min for a surface of 0.74 to 0.77 mm^2 . Prior to analysis, the samples were pre-cleaned with the laser using a stage movement rate of 200 $\mu\text{m.s}^{-1}$. Only ^{238}U , ^{232}Th , ^{208}Pb , ^{207}Pb , and ^{206}Pb were selected, reaching a total mass sweep time of about ~ 60 ms. The selected unknowns were bracketed with the glass SRM NIST612

316 to normalize the lead ratios and drift correction of U/Pb ratios, followed by the WC1 calcite
 317 standard (Age 254.4 ± 6.4 Ma) for the final correction of the U/Pb ratio based on [Roberts et
 318 al. \(2017\)](#). The standards were analyzed in conditions similar to the unknowns, except that
 319 the isotopic maps were of smaller surface (~ 0.2 mm²), corresponding to an analysis time of
 320 ~ 5 min. The Duff Brown Tank limestone (age 64.04 ± 0.67 ; [Hill et al., 2016](#)) was used as a
 321 secondary standard. To calculate the age, two approaches were followed. The first
 322 approach, less precise, consists of dividing the map into squares with a dimension of 5 x 6
 323 pixels, equivalent to 125 μ m x 150 μ m and 15 s of analysis, and then calculating the mean
 324 and its uncertainty for each square. The second approach, similar to that of [Drost et al.
 325 \(2018\)](#), involves sorting the pixel ratio values using the $^{207}\text{Pb}/^{235}\text{U}$ ratio, clustering the data
 326 into discrete steps with a given number of pixels (here 30 pixels corresponding to 15 s of
 327 signal), and then calculating the mean and its uncertainty for each cluster. For both
 328 approaches, the age was obtained through a regression across the corresponding ellipses in
 329 the newly defined total-Pb/U–Th plot of [Vermeesch \(2020\)](#) using IsoplotR ([Vermeesch,
 330 2018](#)). The goodness-of-fit to the data was assessed by calculating the mean squared
 331 weighted deviation (MSWD) on the discretized data. Ages are considered valid when
 332 statistical parameters are satisfying, and when similar ages (within uncertainty) are obtained
 333 for the two approaches. The calculated ages have uncertainties quoted as age $\pm x/y$, where x
 334 corresponds to the confidence interval of the regression and y is with (1) additional analytical
 335 uncertainties (on $^{238}\text{U}/^{206}\text{Pb}$ of glass SRM NIST612) and (2) systematic uncertainties (on
 336 decay constant of ^{238}U (0.05%, 1s) on the $^{238}\text{U}/^{206}\text{Pb}$ ratio of WC1 as estimated by [Roberts et
 337 al. \(2017\)](#) (1.35%, 1s) and long-term excess uncertainty (1%, 1s)).

4. Results

4.1. Field observations

4.1.1. Sedimentology

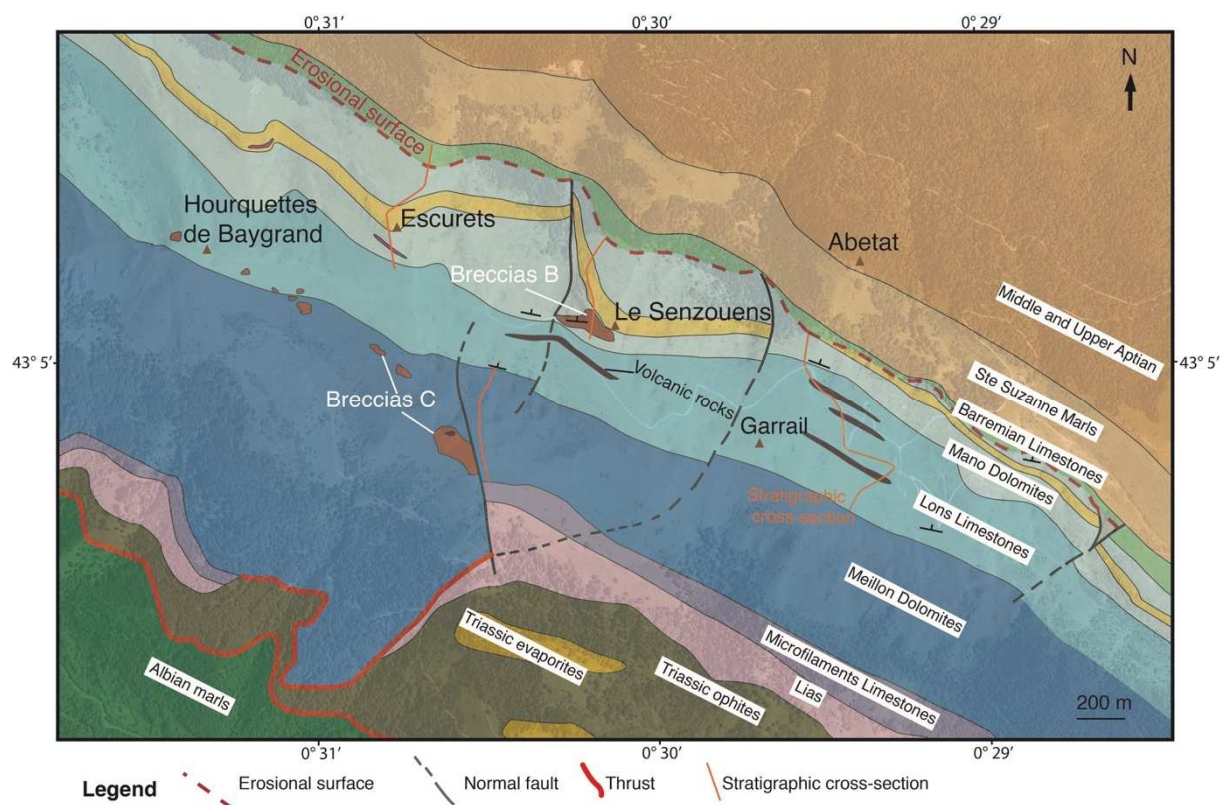


Fig. 2 Geological map of the studied area modified after [Castéras \(1970\)](#) and [Grimaldi \(1988\)](#). Note the differential erosion at the top of the Mano Formation due to the development of normal faults after deposition. Brecciated bodies (B and C) are present in the vicinity of faults and near the upper boundary of the Meillon Formation (see the text for details). Sedimentary breccias (A) are located near the base of the Mano Formation but are not visible at this scale. The color scale is the same as in Fig.1.

On its crest, the Mail Arrouy Ridge includes the Meillon and Mano dolostones as well as the Lons and Annelid Limestones. Over the 15 km length of the Mail Arrouy, dolomitization affects the entire volume of the Meillon and Mano Formations.

The Meillon Formation is characterized by around 350 m of high-energy environment deposits (Fig. 3A). In the lower and upper parts of the formation, the deposits range from wackestone (WST) to packstone (PST) with peloidal and oolitic content. In the middle part of the formation, they mainly consist of oolitic grainstone (GST; Fig. 3B). The entire Meillon Formation is affected by a fabric-destructive dolomitization. Distinguishing the initial texture is

difficult in the presence of this pervasive pluri-micrometric sucrosic dolomite (Fig. 3C). Veins filled with white dolomite cement are present throughout the formation.

The Lons Formation consists of 250 m of barely changing argillaceous mudstone deposits (Fig. 3A). The formation boundaries with the Meillon and Mano Formations are evident, with a clear transition from limestone to dolostone without evidence of geometrical unconformity. No evidence of dolomite was observed.

Most deposits in the Mano Formation consist of dolomudstone (doloMST) or dolowackestone (doloWST) with pellets and oolites (Fig. 3D). Along the entire ridge, variations in thickness (from 250 to 30 m) are controlled by differential erosion during the Neocomian emersion. Dolograinstone (doloGST) with oolites represents the highest energy deposits (Fig. 3E). Interbedded monogenic or rarely polygenic sedimentary breccias (Breccia A) are present at the base of the Mano Formation (Fig. 3F). Breccia A exhibits a particulate rubble packbreccia morphology *sensu* Morrow (1982) (Fig. 4A-B). These carbonate mud-filled breccias have been interpreted as the result of emersion and an arid climate, which induced brecciation caused by karstification or even *Wadi* flows with a very low transport rate (Grimaldi, 1988). The morphology of the dolomite crystals replacing the carbonate matrix depends on the initial facies. In doloMST- or doloWST-type deposits, dolomites are micrometric in size and light-colored (Fig. 3D). As the energy of deposition increases, the size of the dolomites increases from several tens of micrometers to several hundreds of micrometers, becoming increasingly dark. In addition, veins cemented by pluri-micrometric white dolomites are present throughout the formation. Whereas veins have a width of several centimeters, the size of the dolomite cement crystals increases toward the center of the veins, ranging from micrometric to millimetric or centimetric in size.

Above the erosional truncation, the Annelid Formation was deposited in a shallow depositional environment during the flooding of the emerged platform. These 25 m thick limestone deposits range from WST to PST with annelid contents (Fig. 3A). No trace of dolomite was observed in these carbonates.

4.1.2. Structural observations

The Mail Arrouy Ridge presents numerous N-S trending normal faults, which affect the entire Jurassic strata (Fig. 2) and are sealed by the Barremian Annelid Limestones (Grimaldi, 1988). The absence of any sedimentary wedge in the Mano Formation implies that fault activity occurred after the Jurassic carbonate deposition. Fault activity led to the differential erosion of the Mano Formation during the general uplift and exposure after the Tithonian. In the vicinity of the faults, morphologically distinct breccias are present in dyke-like geometries in both the Meillon and Mano Formations (Fig. 2 and Fig. 3A).

In the Mano Formation, these breccias (Breccia B) have monogenic angular clasts that rework the surrounding host rock (Fig. 4C-D), supported by a white dolomite cement (Fig. 3G). These breccias pass laterally to the aforementioned sedimentary breccias (Breccia A). As the distance from the fault zone increases, white dolomite cements become increasingly rare, leaving the initial organization of sedimentary Breccia A with monogenic clasts supported by carbonate mud (Fig. 4A-B). Breccia B presents a cemented rubble floatbreccia morphology. The partial to complete replacement of the initial millimetric elements and the dolomite carbonate mud supported by the white dolomite cement occurs over a distance of 200 to 300 m from the faults (Fig. 2 and Fig. 3A). Due to this intense dolomitization, the initial sedimentary facies of the breccias is not easily identifiable. In some cases, the white dolomite cement is followed by quartz cementation.

In the Meillon Formation, the breccias (Breccia C) have monogenic, unsorted, and angular to sub-angular clasts supported by a white dolomite cement (Fig. 3H and Fig. 4E-F). The network of cemented veins is closely spaced to Breccia B of the Mano Formation, resulting in a cemented mosaic floatbreccia morphology. In some cases, quartz was also precipitated after the dolomite. Locally, these dolomite breccias are affected by a second brecciation event associated with calcite cementation. Breccia C is also observed near the upper boundary of the Meillon Formation in contact with the Lons Formation (Fig. 2 and Fig. 3A-I). Outside this domain and the faulted areas, breccia bodies are very limited in volume,

and white dolomite cements are rarely observed except in tiny veins.

Finally, volcanic rocks are present as sills and dykes in the vicinity of the faults. They are injected into the fault zones in the Meillon, Lons, and Mano Formations (Fig. 2 and Fig. 3A).

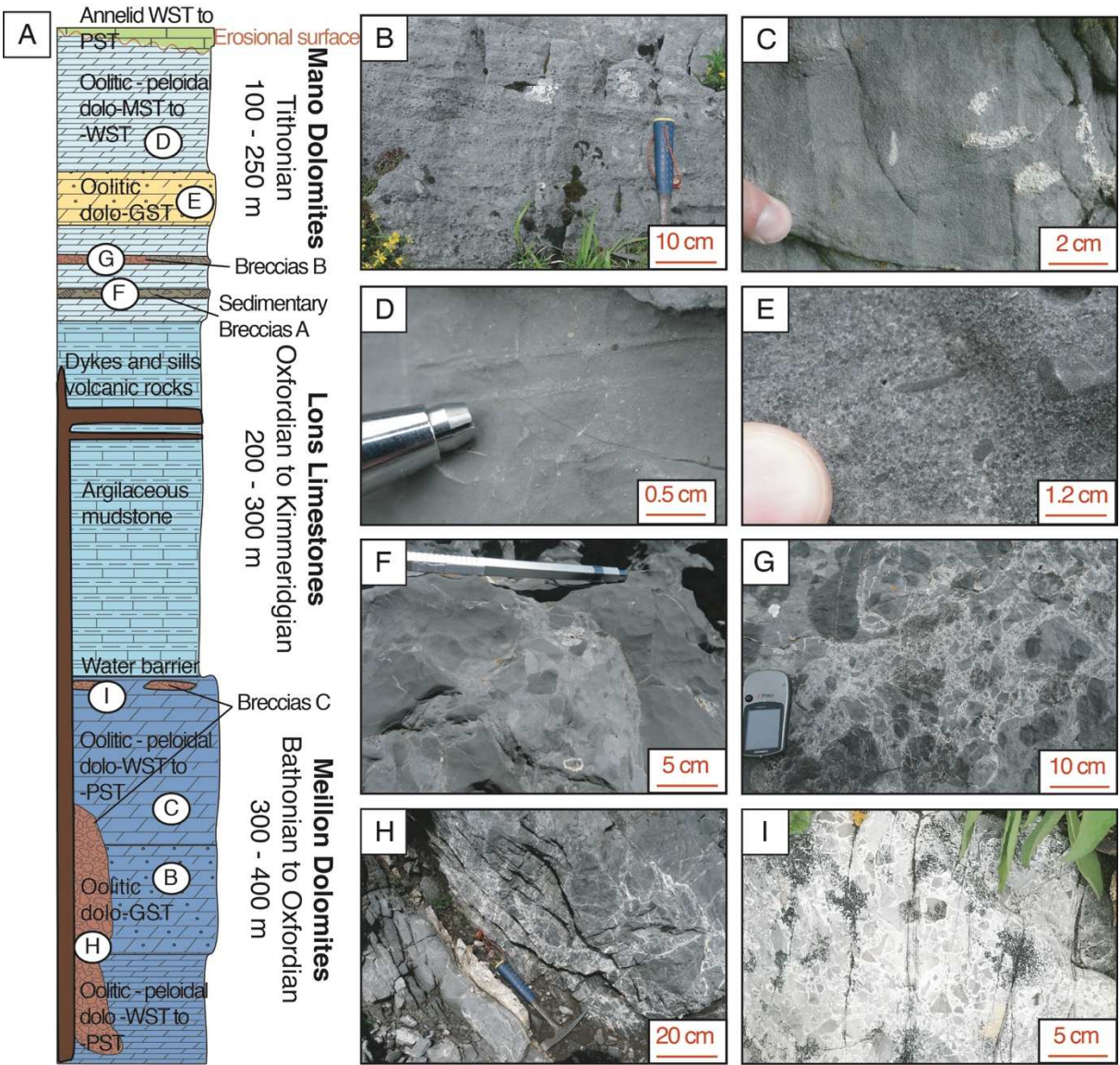


Fig. 3. A) Simplified sedimentological log of the Meillon, Lons, and Mano Formations with the location of the photographs; B to I) Field photographs of sedimentological facies and breccias of the Mail Arrouy. B) Oolitic doloGST with moldic porosity (Meillon Formation); C) Massive doloGST (Meillon Formation); D) DoloMST to doloWST with lenticular bedding (Mano Formation); E) Massive oolitic doloGST (Mano Formation). The dolomite oolite grains are dark, whereas white dolomite cemented the primary porosity; F) Polygenic breccia with sub-rounded clasts supported by a dolomite carbonate mud (Mano Formation); G) Breccias with monogenic unsorted dolomite clasts supported by a white dolomite cement (Mano Formation). This breccia (Breccia B) is located in the vicinity of the fault and passes laterally to the sedimentary breccia (Breccia A); H) Breccia C observed in the vicinity of a N-S fault (Meillon Formation); I) Angular dolomite clasts supported by white dolomite cement near the upper boundary of the Meillon Formation (Breccia C).

426 In this study, the host rock and three distinct breccia types are used to characterize
427 the diagenetic evolution of the entire Mano and Meillon Formations as well as that specific to
428 the fault zones.

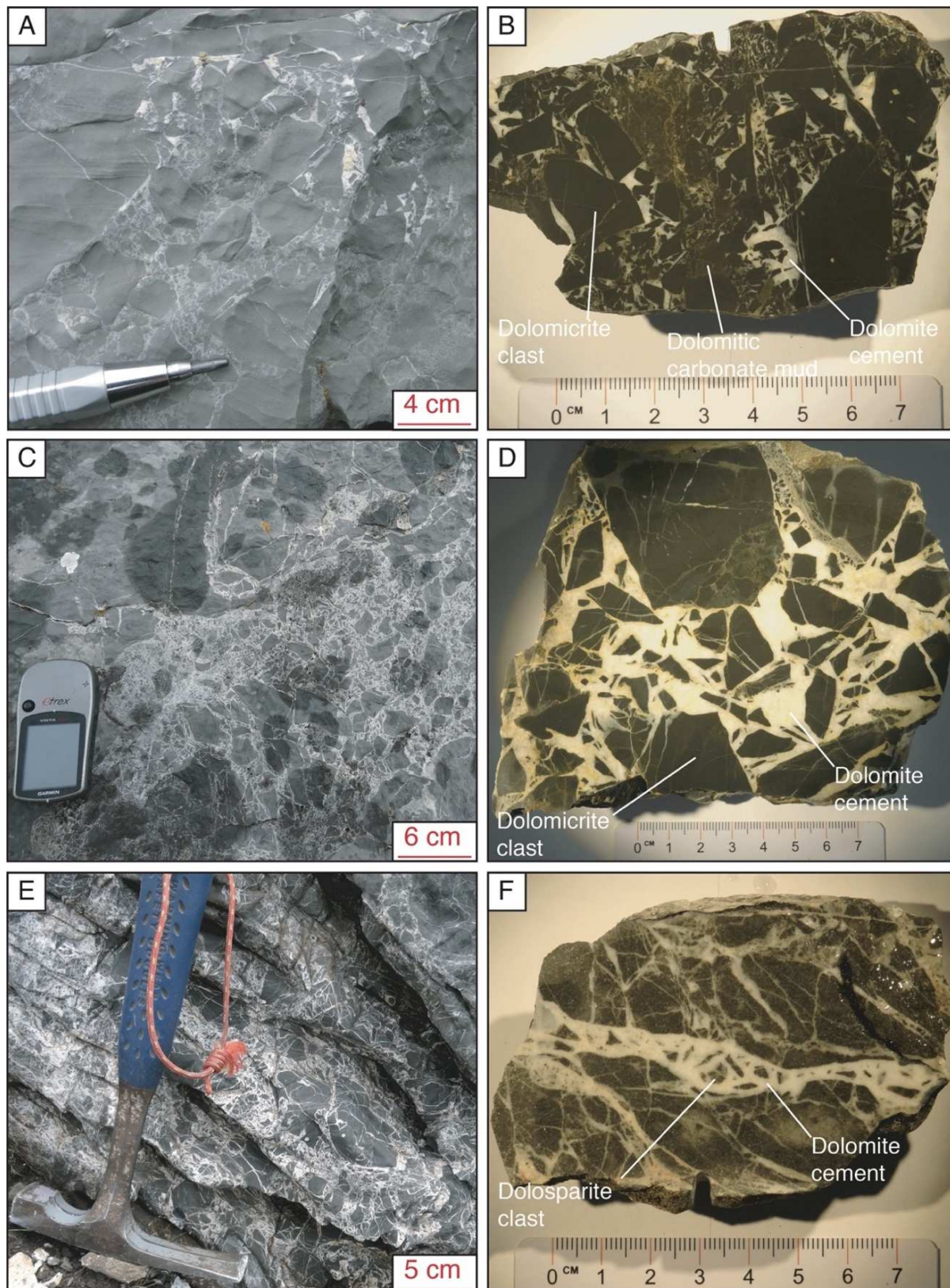


Fig. 4. Field photographs and corresponding polished samples illustrating the progressive transition from sedimentary Breccia A to dolomite Breccia B (A to D) as well as the texture of Breccia C (E, F). A and B) Sedimentary Breccia A with carbonate mud and tiny clasts partly replaced by white dolomite cement; C and D) Example of an almost complete replacement of the initial carbonate mud by white dolomite cement, located closer to a fault, forming a mosaic breccia texture (Breccia B); E and F) Breccia C with angular clasts supported by a white dolomite cement. Breccia C differs from B by the abundance of diffuse fracturing.

4.2. Petrographical observations

4.2.1. Mano Formation

4.2.1.1. Early diagenetic features

In the grainstone facies, oolitic and peloidal grains have been partially dissolved, creating secondary porosity (Fig. 5A). The undissolved parts were also micritized before being dolomitized.

4.2.1.2. Replacive dolomite

The Mano Formation is affected by widespread dolomitization. In the mudstone and wackestone facies, the replacive dolomite crystals (RD1_{Mano}) are planar-S and range from 10 to 50 µm in size. They are gray to dark gray in color, turbid, and inclusion-rich. Under CL, the RD1_{Mano} has a dull to dark-red luminescence.

RD1_{Mano} completely overprints and thus postdates the sedimentary breccia (Fig. 5B). In the grainstone facies, the oolites and peloids are dolomitized by RD1_{Mano}, leaving the original fabric preserved (Fig. 5A).

4.2.1.3. Dolomite cements

Three dolomite cements can be distinguished on the basis of their crystal morphologies, size ranges, and CL luminescence. They occur as porosity-filling phases in grainstone facies (Fig. 5A), vein filling (Fig. 5C), and clast-supported cements in the diagenetic Breccia B (Fig. 5D). All cements are light gray to white in plane polarized light (PPL) and variably limpid. The grains do not exhibit compaction patterns (Fig. 5B), suggesting that the dolomite cementation affected the Mano Formation in a shallow burial context.

The first dolomite cement to precipitate (DC2_{Mano}) consists of planar-S crystals

between 50 and 150 μm in size (Fig. 6A). It forms a thin rim located at the edge of the clasts or the host rock, with a light gray color. Locally in the breccias, DC2_{Mano} replaces the host rock (Fig. 6B). Under CL, DC2_{Mano} displays a dark red luminescence. Very small ($\leq 5 \mu\text{m}$) aqueous and solid inclusions are present in large quantities. DC2_{Mano} was impacted by subsequent brecciation (Fig. 6C).

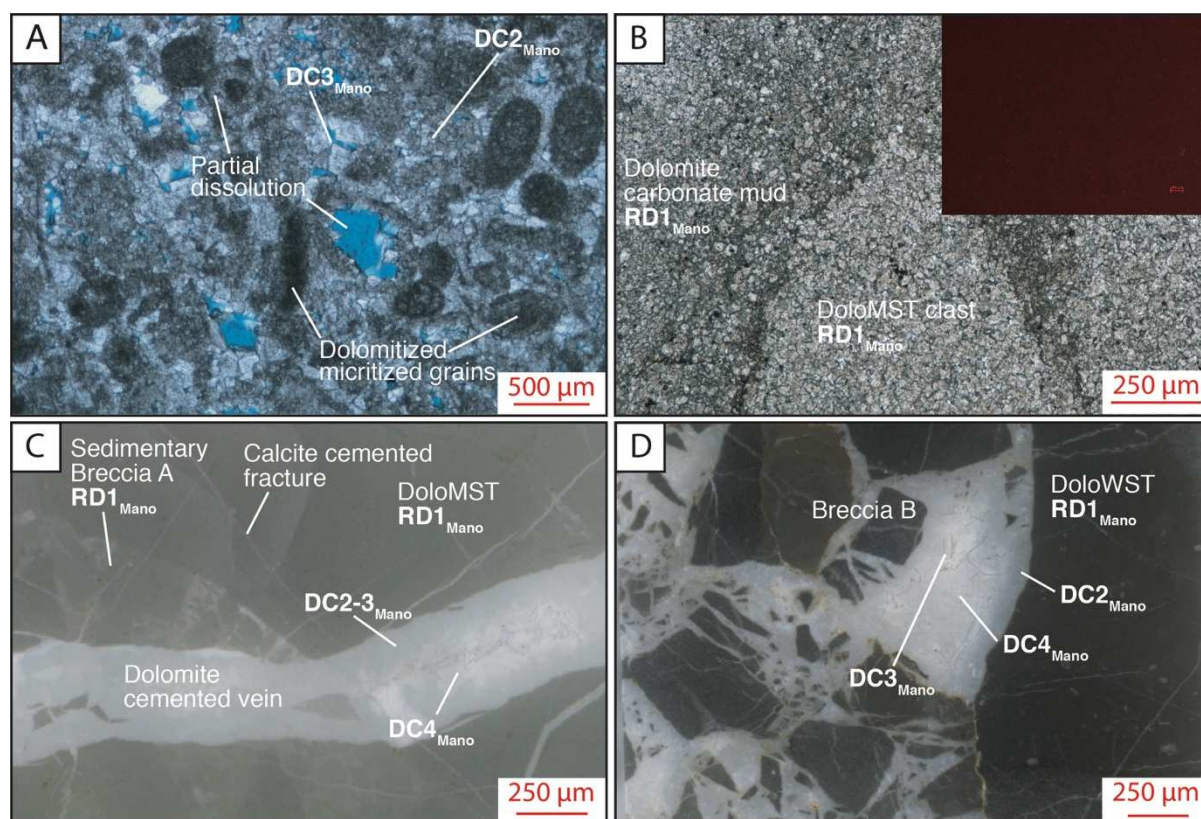


Fig. 5. Overview of the facies and breccias present in the Mano Formation in PPL with a scan of thin sections. A) DoloGST with fully micritized and partially dissolved dolomitized grains. The primary porosity is cemented by a white dolomite cement in planar-S to planar-E texture (DC2_{Mano}). Some planar-E dolomite crystals (DC3_{Mano}) precipitated in residual porosity; B) DoloMST in sedimentary Breccia A dolomitized by fine non-planar dolomite (RD1_{Mano}). Under CL, both the matrix and the mud share common CL luminescence; C) Thin section scan of a sedimentary breccia cross-cut by a dolomite-cemented vein. The matrix and Breccia A are fully dolomitized by RD1_{Mano}. The vein is cemented by a multi-phase dolomitization. In the center of the vein, dolomite crystals (DC4_{Mano}) are more limpid than near the edge (DC2-3_{Mano}); D) Example of dolomite cements observed in Breccia B comprising DC2_{Mano}, DC3_{Mano}, and DC4_{Mano}.

The second dolomite cement (DC3_{Mano}) precipitated after DC2_{Mano}, as shown by its common presence as DC2_{Mano} crystal overgrowth (Fig. 6C). DC3_{Mano} crystals are light gray, have a planar-E texture, and range from 300 to 1000 μm in size (Fig. 6A, B, D, and Fig. 5D). Locally, DC3_{Mano} has a saddle texture due to its curved faces (Fig. 6D). CL observations highlight three successive growth zones characterized by distinct luminescence: DC3a in

dark red, DC3b in red, and DC3c in alternating bright orange to red bands (Fig. 6A, B, D). The DC3b growth zone displays numerous primary fluid inclusions aligned along the crystal boundaries (Fig. 6A).

The third dolomite cement (DC4_{Mano}) is observed only locally. It mainly occurs as large (300 µm to 2000 µm) saddle blocky crystals in the breccias and the center of veins (Fig. 5C, D and Fig. 6E). This cement is limpid and contains only a few fluid inclusions. Under CL, it is characterized by a dull red luminescence (Fig. 6E, D). Locally, DC4_{Mano} is impacted by dedolomitization, which is more pronounced along the crystal growth planes (Fig. 6F).

4.2.1.4. Calcite and quartz cements

Calcite cements are scarce. Locally, the stainings reveal calcite inside the dolomite crystals, which is interpreted as resulting from dedolomitization (Fig. 6F). These calcite crystals (5 to 20 µm) are non-luminescent under CL. Given their tiny size, they cannot be related to other calcite cements.

Calcite cements (CC1_{Mano}) are also observed in veins and breccias. They are made of limpid, large (> 1 mm) blocky crystals with a dull-brown CL luminescence (Fig. 6G).

Quartz (Qtz_{Mano}) is more common than calcite, but it is only observed locally. It is made of limpid, large (> 500 µm) blocky crystals postdating DC4_{Mano} in the veins and breccias (Fig. 5C, D). Dedolomitization features are often observed in the vicinity of the contacts between quartz and dolomite crystals (Fig. 6H).

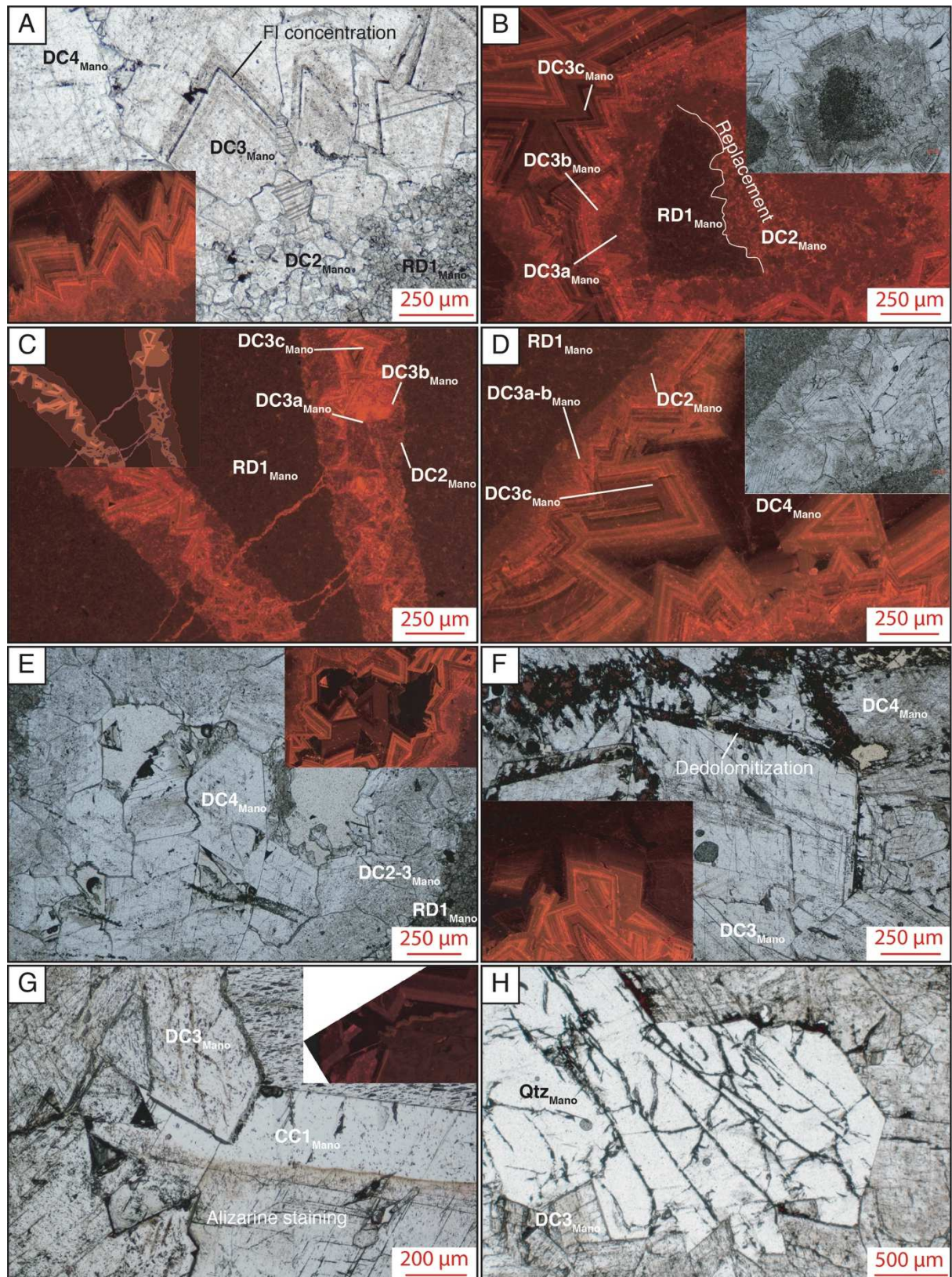


Fig. 6: Main characteristics of the cements present in the Mano Formation. A) Example of multi-phase dolomitization. The matrix was replaced by a fine non-planar dolomite RD1_{Meillon}. Vein-filling cements are made of fine planar-S to planar-E dolomite DC2_{Mano} with planar-E dolomite DC3_{Mano} overgrowths, followed by limpid saddle dolomite DC4_{Mano}; B) RD1_{Mano}, DC2_{Mano}, and DC3_{Mano} observed under CL. In Breccia B, a clast initially dolomitized by RD1_{Mano} is partially replaced by DC2_{Mano}; C) Dolomite-cemented veins in the host rock. The veins are similar to those in Breccia B except for the absence of DC4_{Mano}; D) Complete dolomite cementation with DC3_{Mano} in saddle configuration; E) Large DC4_{Mano}

saddle crystals within Breccia B; F) Local dedolomitization of dolomite fringes as revealed by staining; G and H) Local cementation of the remaining intercrystalline porosity by dull-brown calcite CC1_{Meillon} (G) or quartz Qtz_{Meillon} (H).

4.2.2. Meillon Formation

4.2.2.1. Early diagenetic features

The wackestone facies located at the top of the Meillon Formation has not been completely dolomitized. The grains are partly micritized (Fig. 7A). Under CL, the micritic envelopes and the unaffected parts of the grains display an orange and dark orange luminescence, respectively (Fig. 7A). The remaining parts of the Meillon Formation, mainly made of oolitic packstone to grainstone, are completely dolomitized. The oolites were micritized before dolomitization and partially dissolved (Fig. 7B, C).

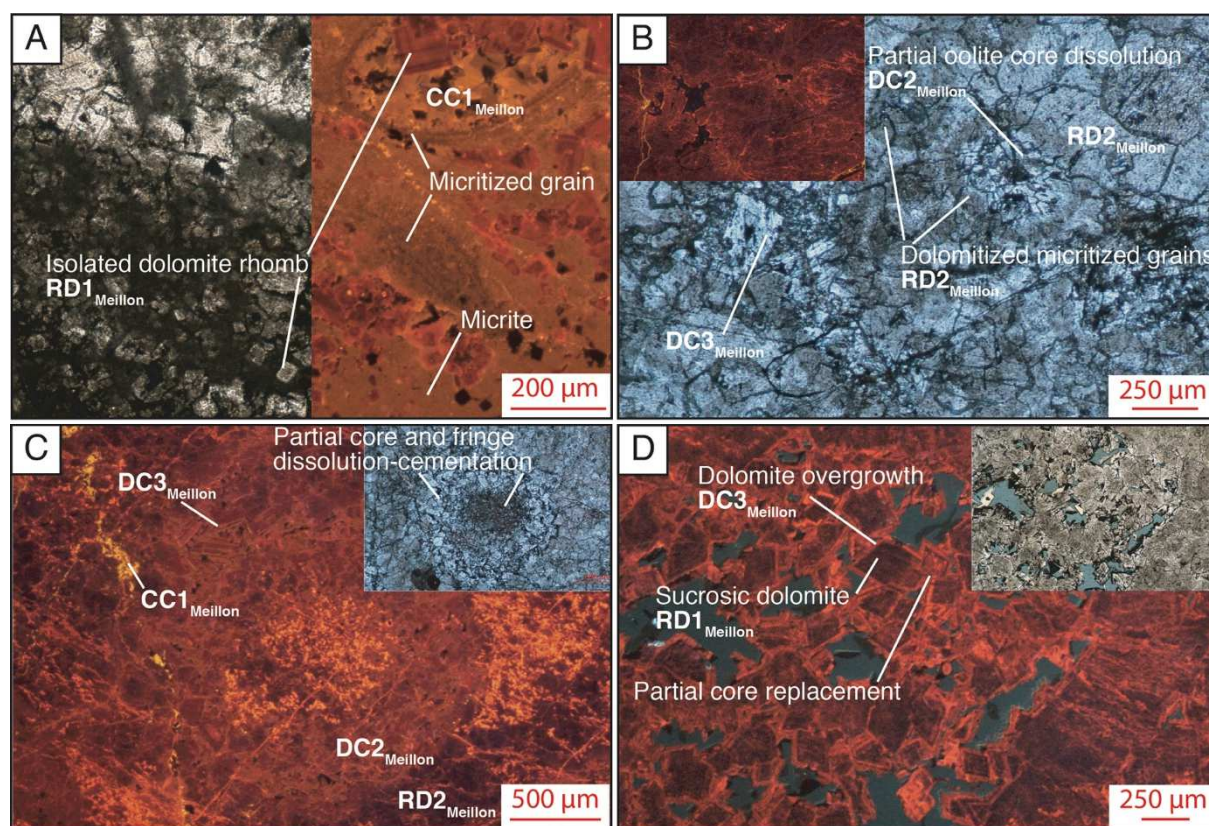


Fig. 7. Overview of cements and replacive dolomites present in the Meillon Formation. A) Near the upper boundary of the Meillon Formation, the dolomitization is partial, leaving the initial texture with isolated RD1_{Meillon} rhombs in micrite. Calcite cements are also present (CC1_{Meillon}); B) Planar-S RD2_{Meillon} dolomite in the oolitic grainstone facies. Secondary porosity was cemented by planar-S DC2_{Meillon} and planar-E DC3_{Meillon} dolomites; C) Example of oolite dissolution before dolomitization; D) Planar-E sucrosic dolomite RD1_{Meillon}. Secondary intercrystalline porosity was partially filled by DC2_{Meillon} overgrowths. DC2_{Meillon} locally replaces the core of RD1_{Meillon} crystals.

528 4.2.2.2. *Replacive dolomites*

529 The Meillon Formation presents two dolomite crystal textures that are non-fabric-
530 preserving to partially fabric-preserving. First, a sucrosic replacive dolomite (RD1_{Meillon}) is
531 observed locally (Fig. 7D). RD1_{Meillon} crystals have a planar-E texture and range from 50 to
532 100 µm in size. The crystals have cloudy cores and clear fringes. Under CL, the cores
533 generally have a dull red luminescence, whereas the outer fringes are bright red. However,
534 some rhombs display irregular patches of red CL luminescence inside the cores, which is
535 indicative of partial replacement (Fig. 7D). In the wackestone facies, the RD1_{Meillon}
536 dolomitization is not always complete, leaving isolated dolomite rhombs in the micrite matrix
537 (Fig. 7A). In the grainstones, the dolomitization is complete, leaving an important
538 intercrystalline porosity. Second, a replacive dolomite (RD2_{Meillon}) that commonly replaces
539 and thus postdates RD1_{Meillon} dolomite, affects almost the entire Meillon Formation. RD2_{Meillon}
540 crystals are light gray in PPL, have a planar-S texture, and range from 50 to 200 µm in size
541 (Fig. 7B). In CL, they display a homogeneous dark red luminescence (Fig. 7C). RD2_{Meillon}
542 dolomite replaces all the uncompacted grains, leaving dark gray ghosts (Fig. 7B).

543 4.2.2.3. *Dolomite cements*

544 Dolomite cements are present in the intercrystalline porosity or veins of the host rock
545 and Breccia C. These cements have three distinct crystal textures and CL luminescence.

546 Dolomite cement 2 (DC2_{Meillon}) is the first cement observed at the edge of the
547 intercrystalline, moldic porosity, and veins of the host rock (Fig. 7C and Fig. 8A, B). DC2_{Meillon}
548 is also present in the brecciated bodies (Fig. 8A). This cement has a light gray color in PPL
549 as well as a planar-S to planar-E dolomite crystal texture, ranging from 50 to 200 µm in size
550 (Fig. 8B). Under CL, it displays a dark red luminescence.

551 Dolomite cement 3 (DC3_{Meillon}) occurs as an overgrowth of DC2_{Meillon}, partially or
552 completely filling the remaining intercrystalline and moldic porosity of the host rock (Fig. 7C,
553 D and Fig. 8B, C). This limpid cement is also associated with fractures that postdate

DC2_{Meillon} in the host rock and Breccia B (Fig. 8D, E). DC3_{Meillon} crystals have a planar-S to planar-E dolomite texture and range from 50 to 300 µm in size. Under CL, DC3_{Meillon} generally displays bright red luminescence (Fig. 8B). Locally, distinct CL fringes are observed in larger cement (Fig. 8C). DC3_{Meillon} also forms an overgrowth on RD1_{Meillon} crystals (Fig. 7D).

Dolomite cement 4 (DC4_{Meillon}) is the last in the Meillon Formation. DC4_{Meillon} has a saddle dolomite crystal texture and ranges from 500 to 3000 µm in size. This light gray to limpid dolomite cement is only present locally in breccias as an overgrowth of DC3_{Meillon} (Fig. 8D, F). Under CL, this cement displays a dark red luminescence with large bright fringes.

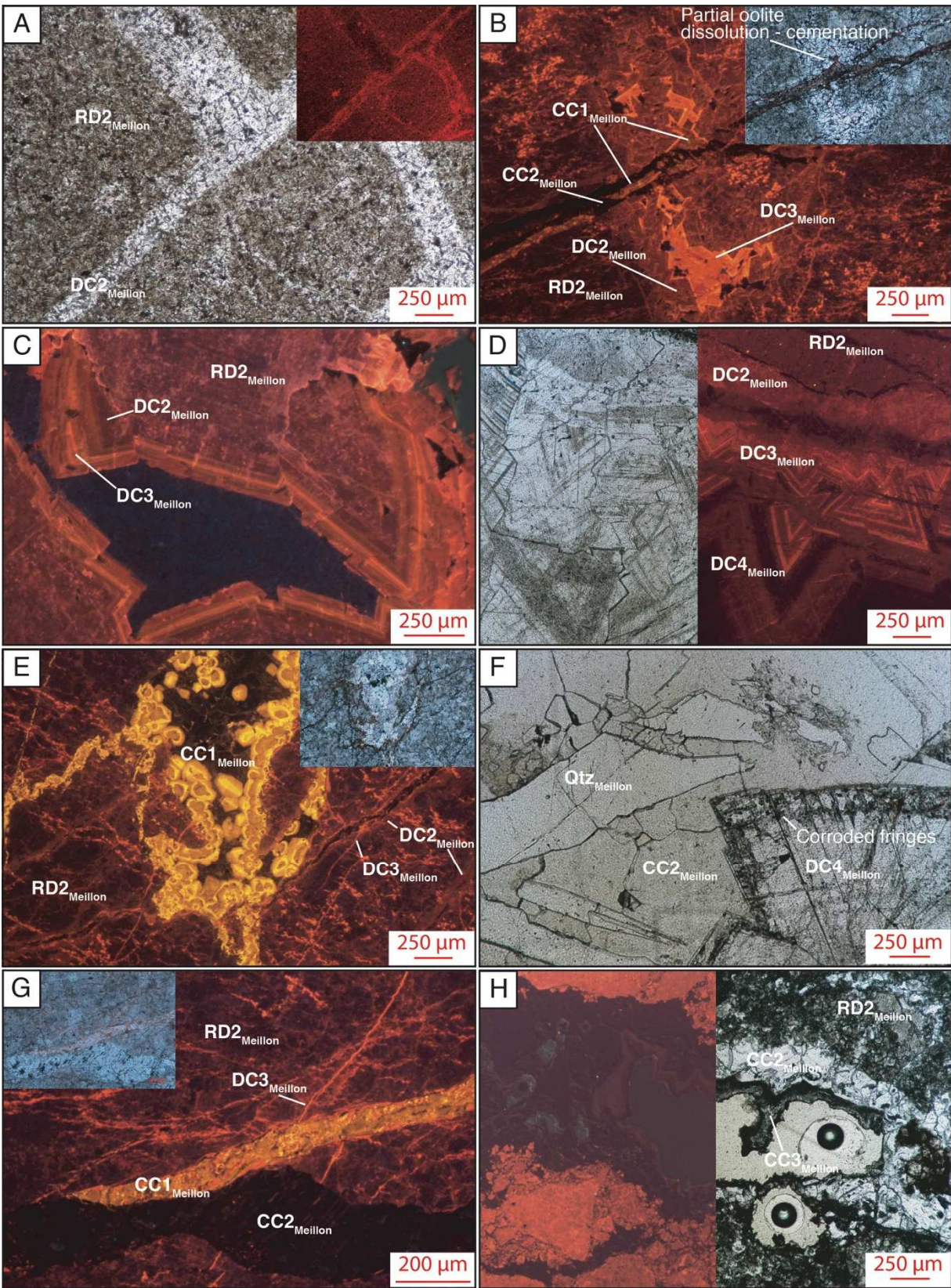
4.2.2.4. Calcite and quartz cements

The first calcite cement (CC1_{Meillon}) to precipitate in the Meillon Formation occurs in veins (Fig. 8G) and as pore-filling (Fig. 8B). It displays a drusy fabric with sub-euhedral to euhedral crystals ranging from 30 to 300 µm. Under CL, CC1_{Meillon} exhibits three successive growth bands with distinct luminescence: an orange luminescence, followed by a bright yellow external fringe, and in the coarsest pores or veins (up to 200 µm wide), a dull-brown color. Locally, CC1_{Meillon} fills pores generated by the previous dolomite dissolution or directly replaces existing dolomite (Fig. 8E).

CC2_{Meillon} is commonly observed as cement filling the residual intercrystalline porosity present in large veins of the host rock or in breccia cements (Fig. 8F, G, H). CC2_{Meillon} fills fractures that postdate CC1_{Meillon} and quartz cements (Fig. 8F, G). Locally, CC2_{Meillon} supports dolomitized clasts in breccia C (Fig. 8H). It has a blocky fabric with limpid crystals ranging from 100 to 1000 µm in size. Under CL, CC2_{Meillon} is non-luminescent (Fig. 8F, G, H). Locally, CC2_{Meillon} replaces DC4_{Meillon}, leaving corroded rims (Fig. 8F). A last calcite cement with a dripstone fabric (CC3_{Meillon}) is observed only rarely in remnant pores (Fig. 8H).

Quartz cement (Qtz_{Meillon}) occurs in Breccia C (Fig. 8F), where it clearly postdates DC4_{Meillon} but predates CC2_{Meillon}. The relative chronology between Qtz_{Meillon} and CC1_{Meillon} is

580 not clear. The crystals are limp with a size up to 500 μm .



581
582 Fig. 8. Main characteristics of the cements present in the Meillon Formation (PPL and CL). A)
583 RD2_{Meillon} planar-S dolomite pervasively replacing the initial matrix. A vein affecting the host rock is
584 filled by the planar-S dolomite cement DC2_{Meillon}; B) Illustration of the relative timing of dolomite and
585 calcite cements in the grainstone facies. DC2-3_{Meillon} dolomite cements postdate the replacive dolomite

RD1_{Meillon}. They are followed by CC1_{Meillon} calcite in veins and remnant porosity. CC2_{Meillon} is the last vein-filling cement; C) Example of the succession of RD2_{Meillon}, DC2_{Meillon}, and DC3_{Meillon} dolomites filling a vein; D) An additional saddle dolomitization stage DC4_{Meillon} is observed in Breccia C; E) Dedolomitization or solution-cavity fills associated with CC1_{Meillon} can locally affect the RD2_{Meillon} dolomite matrix. Note the three distinct CL luminescences of CC1_{Meillon}; F) Additional CC2_{Meillon} cements are observed in Breccia C. DC4_{Meillon} cement presents corroded rims. The remaining intercrystalline porosity was first partially cemented by quartz Qtz_{Meillon}. After the Qtz_{Meillon} fracturing, CC2_{Meillon} has blocked the remnant porosity; G) Another illustration of the relative timing of cementation between dolomite and calcite. DC3_{Meillon} is cross-cut by a vein filled by CC1_{Meillon}, which is cross-cut by a vein filled by CC2_{Meillon}; H) Calcite cement CC2_{Meillon} supports clasts in Breccia C. It is followed by dripstone calcite CC3_{Meillon}.

4.3. Geochemistry

4.3.1. Composition

The Mano dolomites are nearly stoichiometric (Table 1). Their Mg and Ca contents are consistent among the cements (less than 0.7 weight (wt) % variation). RD1_{Mano} exhibits high contents of Fe and Si (around 3300 and 5800 ppm, respectively, in mean values) compared to DC2-3_{Mano} dolomite cements (around 850 and 250 ppm, respectively, in mean values). The high Fe and Si values are likely a marker of detrital contamination. DC4_{Mano} has the highest Fe content value (up to 3000 ppm) and the lowest Si content value (less than 200 ppm) of all the dolomite cements. Mn and Sr values remain low (< 100 and < 200 ppm, respectively) in all the dolomites.

The Meillon dolomites are also nearly stoichiometric (Table 1). RD1_{Meillon} exhibits high Fe and Si contents (around 1800 and 2307 ppm, respectively, in mean values) compared to RD2_{Meillon} (around 400 and 650 ppm, respectively, in mean values). DC2_{Meillon} is Si-rich (around 2000 ppm) and presents a low content of Fe and Sr (around 300 and 150 ppm, respectively). CC1_{Meillon} exhibits higher Mn and Sr contents (around 550 and 650 ppm, respectively) and low Si and Fe contents (around 350 and 300 ppm).

		Ca (wt%)	Mg (wt%)	Si (ppm)	Mn (ppm)	Fe (ppm)	Sr (ppm)
RD1 _{Mano}	Max.	21.1550	13.268	24729	266	83810	512
	Min.	16.85	11.198	168	bdl	97	bdl
	Mean	20.3301	12.5831	5793	59	3275	74
Normalized to six oxygens		0.965	0.985	0.039	0	0.011	0
DC2 _{Mano}	Max.	21.834	13.167	834	322	1940	323
	Min.	20.563	12.531	103	51	223	bdl
	Mean	21.0479	12.8617	269	171	747	96
Normalized to six oxygens		0.994	1.001	0.002	0.001	0.003	0
DC3 _{Mano}	Max.	21.486	13.648	1279	370	3588	466
	Min.	14.787	11.322	bdl	53	bdl	bdl
	Mean	20.8001	12.7671	233	216	996	101
Normalized to six oxygens		0.990	1.004	0.002	0.001	0.004	
DC4 _{Mano}	Max.	21.354	13.236	455	292	8245	170
	Min.	18.24	11.7180	38	bdl	354	bdl
	Mean	20.4447	12.6566	183	106	3050	6
Normalized to six oxygens		0.984	1.004	0.001	0	0.011	
RD1 _{Meillon}	Max.	24.4488	12.58	21991	3265	6891	512
	Min.	17.937	10.011	2	bdl	607	bdl
	Mean	20.7248	11.4378	2307	296	1765	74
Normalized to six oxygens		1.035	0.941	0.016	0.001	0.006	
RD2 _{Meillon}	Max.	25.853	12.976	904	398	671	715
	Min.	21.9303	10.0012	327	bdl	135	bdl
	Mean	22.9991	12.0602	652	129	368	173
Normalized to six oxygens		1.070	0.925	0.004	0	0.001	
DC2 _{Meillon}	Max.	23.045	14.193	6980	607	418	371
	Min.	21.804	13.355	612	210	119	bdl
	Mean	22.5138	13.7310	2250	396	247	120
Normalized to six oxygens		0.989	0.995	0.014	0.001	0.001	
CC1 _{Meillon}	Max.	41.252	0.3753	845	3158	831	1186
	Min.	38.286	bdl	52	bdl	bdl	168
	Mean	40.3069	0.0758	364	567	287	665
Normalized to six oxygens		1.990	0.005	0.003	0.002	0.001	

bdl: below detection limit

Table 1. Elemental composition (microprobe data) of the investigated cements in both the Mano and Meillon Formations.

4.3.2. Stable isotopes

Selected SIMS transects for the Meillon and Mano Formations are shown in Fig. 9 and Fig S3, while the mean $\delta^{18}\text{O}$ and $\delta^{13}\text{C}$ SIMS values of each diagenetic phase are presented in Fig. 10 and Table 2. Both SIMS and bulk data were obtained for RD1_{Mano} and DC4_{Mano}. For RD1_{Mano}, the mean $\delta^{18}\text{O}$ and $\delta^{13}\text{C}$ values obtained by SIMS are -3.2 and +3.1‰, respectively, whereas for bulk samples they are -0.80 and +1.55‰, respectively. For DC4_{Mano}, the mean $\delta^{18}\text{O}$ and $\delta^{13}\text{C}$ values obtained by SIMS are -12.45 and 2.9‰, respectively, whereas for bulk samples they are -9.8 and +1.2‰, respectively. The differences between the values measured by SIMS and on bulk samples are +2.41‰ for RD1_{Mano} and +2.68‰ for DC4_{Mano}. The mean (+2.54‰) was used to correct for the matrix

effect on $\delta^{18}\text{O}$ SIMS data for the other dolomite cements.

In the Mano Formation (Fig. 9), the $\delta^{18}\text{O}$ and $\delta^{13}\text{C}$ of RD1_{Mano} (n = 7) range from -3.0 to +0.7‰ (mean = -0.7‰; median = -0.5‰) and from +0.6 to +4.6‰ (mean = +3.1‰; median = +3.3‰), respectively. A significant negative shift in the $\delta^{18}\text{O}$ is measured between RD1_{Mano} and DC2_{Mano}. The $\delta^{18}\text{O}$ and $\delta^{13}\text{C}$ of DC2_{Mano} (n = 22) range from -14.7 to -11.5‰ (mean = -13.6‰; median = -13.7‰) and from -1.7 to +5.7‰ (mean = +3.2‰; median = +3.5‰), respectively. The $\delta^{18}\text{O}$ and $\delta^{13}\text{C}$ of DC3_{Mano} (n = 43) range from -14.6 to -9.4‰ (mean = -11.9‰; median = -11.9‰) and from +0.8 to +5.2‰ (mean = +3.4‰; median = +3.5‰), respectively. The last cement DC4_{Mano} is characterized by a positive shift in oxygen isotope values (Fig. 9). The $\delta^{18}\text{O}$ and $\delta^{13}\text{C}$ of DC4_{Mano} (n = 29) range from -13.1 to -7.9‰ (mean = -9.9‰; median = -10.0‰) and from +0.3 to +4.9‰ (mean = +2.9‰; median = +3.3‰), respectively.

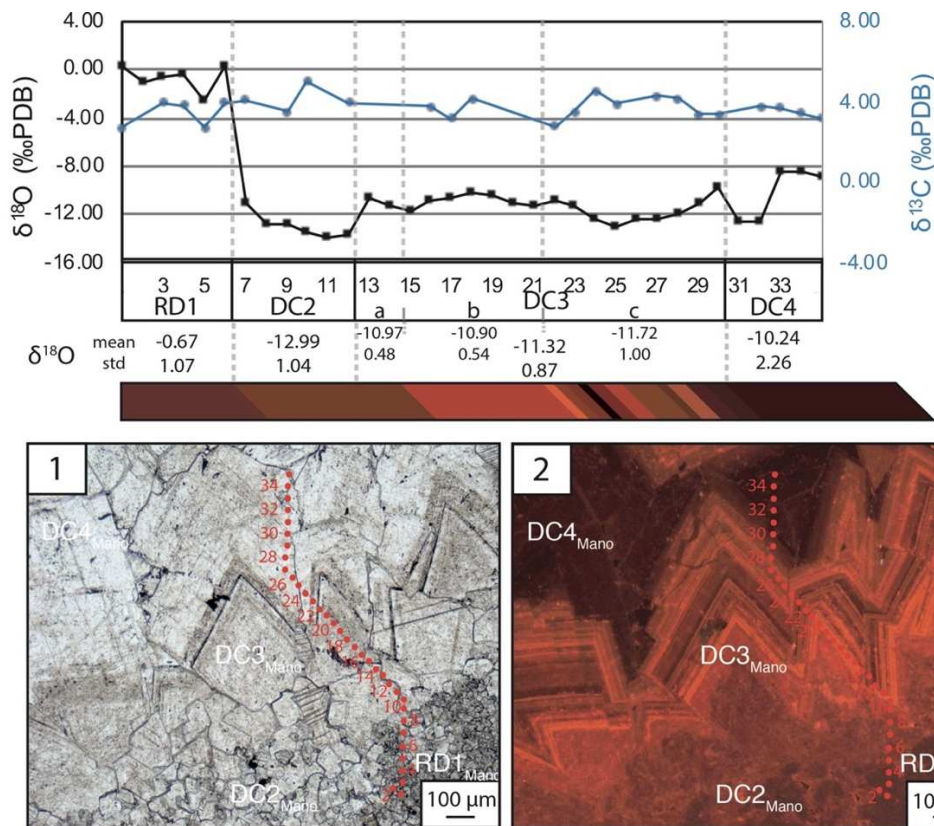


Fig. 9. Detailed SIMS $\delta^{18}\text{O}$ and $\delta^{13}\text{C}$ values obtained from a transect of Mano dolomite cements. The location of the transect is shown in images 1 (PPL) and 2 (CL). $\delta^{18}\text{O}$ exhibits a significant negative shift between RD1_{Mano} matrix and DC2_{Mano}, whereas the $\delta^{13}\text{C}$ has constant values along the entire transect.

In the Meillon Formation, five SIMS transects were performed, covering all the dolomites, CC1_{Meillon} and CC2_{Meillon}. Similar to the Mano Formation, the Meillon dolomites exhibit strong oxygen isotopic variations. The $\delta^{18}\text{O}$ and $\delta^{13}\text{C}$ of RD1_{Meillon} (n = 4) range from -4.5 to -3.3‰ (mean = -4.0‰; median = -4.0‰) and from -0.7 to +7.4‰ (mean = +3.9‰; median = +4.5‰), respectively, while RD2_{Meillon} (n = 3) has $\delta^{18}\text{O}$ values between -14.5 and -12.6‰ (mean = -13.4‰; median = -13.2‰) and $\delta^{13}\text{C}$ values between -1.4 and +3.7‰ (mean = +1.1‰; median = +1.1‰). DC2_{Meillon} (n = 21) exhibits $\delta^{18}\text{O}$ values close to RD2_{Meillon}, ranging from -16.5 to -11.1‰ (mean = -14.3‰; median = -14.5‰). The associated $\delta^{13}\text{C}$ values range from -3.4 to +5.1‰ (mean = +1.2‰; median = +1.2‰). The $\delta^{18}\text{O}$ and $\delta^{13}\text{C}$ of DC3_{Meillon} (n = 4) range from -10.8 to -8.6‰ (mean = -9.6‰; median = -9.5‰) and from -1.4 to +4.1‰ (mean = +1.3‰; median = +1.2‰), respectively. The last dolomite cement DC4_{Meillon} (n = 29) has fewer negative $\delta^{18}\text{O}$ values ranging from -10.1 to -5.7‰ (mean = -7.7‰; median = -8.0‰). The associated $\delta^{13}\text{C}$ values range from -2.9 to +4.5‰ (mean = +1.0‰; median = +1.6‰). The $\delta^{18}\text{O}$ values of CC1_{Meillon} (n = 13) and CC2_{Meillon} (n = 11) range from -5.6 to -0.5‰ (mean = -2.6‰; median = -1.9‰) and -12.5 to -6.8‰ (mean = -9.5‰; median = 8.9‰), respectively ($\delta^{13}\text{C}$ could not be measured).

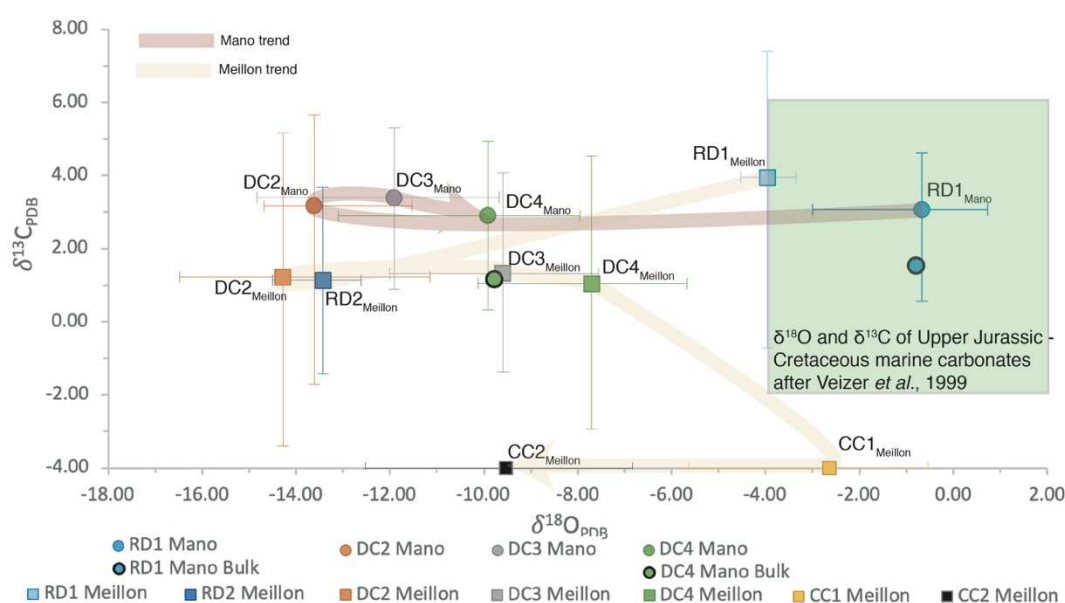


Fig. 10. Mean $\delta^{18}\text{O}$ and $\delta^{13}\text{C}$ values of all the dolomites measured by SIMS, with the minimum and maximum values represented by bars. The Upper Jurassic and Cretaceous marine carbonate values are represented in the green box (Veizer et al., 1999).

4.3.3. Strontium isotopes

For the Mano Formation, the Sr isotope ratio of RD1_{Mano} varies from 0.707461 to 0.707798 (Fig. 11 and Table 2). The small size of the DC2_{Mano} and DC3_{Mano} cements prevented their separate analysis. The mixture of these two cements (n = 2) shows ⁸⁷Sr/⁸⁶Sr ratios of 0.708484 and 0.709001. The two measurements made for the final dolomite cement DC4_{Mano} give values of 0.710043 and 0.710130.

For the Meillon Formation, RD2_{Meillon} dolomite (n = 2) exhibits ⁸⁷Sr/⁸⁶Sr ratios of 0.707630 and 0.707780. The analysis of the mixture between RD1_{Meillon} and DC2_{Meillon} (n = 2) gives a Sr isotope ratio between 0.707520 and 0.707590. The mixture of DC2_{Meillon} and DC3_{Meillon} (n = 2) gives ⁸⁷Sr/⁸⁶Sr ratios of 0.707821 and 0.707929. For DC4_{Meillon} (n = 2), the Sr isotope ratios vary from 0.707900 to 0.708120. The Sr isotope ratio of one calcite cement CC2_{Meillon} was 0.707770. The calcite matrix present in the upper part of the Meillon Formation (n = 2) has Sr isotope ratios varying from 0.707715 to 0.707770.

The ⁸⁷Sr/⁸⁶Sr ratios of anhydrite (n = 2) and halite samples (n = 2) of Triassic evaporites from the Belair well vary from 0.707825 to 0.707827 and from 0.708560 to 0.708565, respectively.

The Sr isotope ratios of the volcanic sills sampled in the Lons Formation (n = 2) are 0.705322 and 0.705348. The ⁸⁷Sr/⁸⁶Sr ratio of the basaltic rocks embedded in the Albian turbidites (n = 1) is 0.705851.

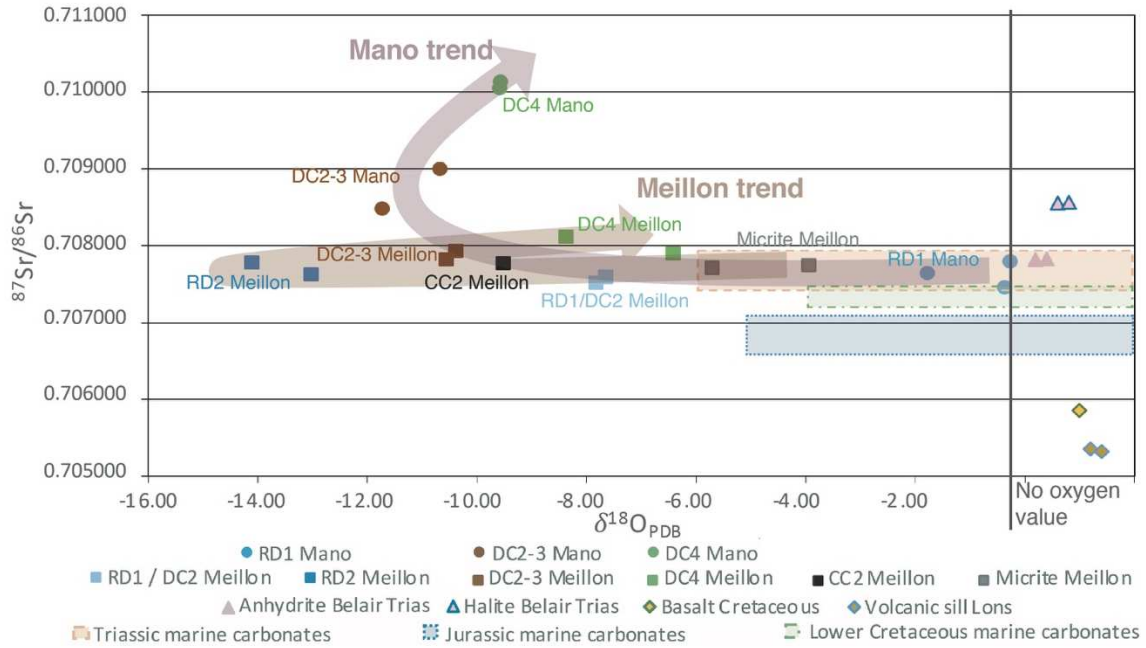


Fig. 11. $^{87}\text{Sr}/^{86}\text{Sr}$ vs $\delta^{18}\text{O}$ plot of the different cements and rocks. The arrows represent the chronological trend deduced from petrographical observations. The Jurassic and Triassic marine carbonate values are also indicated (McArthur et al., 2001).

4.3.4. U-Pb dating

Accurate total-Pb/U-Th ages could be obtained for six samples corresponding to RD1_{Mano}, DC2_{Mano}, RD2_{Meillon}, and DC4_{Meillon}. These results, presented on Tera-Wasserburg plots, are provided in Fig. S1 for the first approach (subdivision of the isotopic image in 150 $\mu\text{m} \times 125 \mu\text{m}$ squares), and in Fig. 12 for the second approach inspired by Drost et al. (2018). For RD1_{Mano}, two samples could be analyzed. For one sample, 136.4 \pm 6.8 Ma (MSWD = 0.3) was obtained with the first approach, while a similar but slightly more precise age of 136.7 \pm 4.7 Ma (MSWD = 1.95) was found with the second approach. For the other sample, ages of 127.0 \pm 7.3 Ma (MSWD = 0.6) and 132.6 \pm 4.5 Ma (MSWD = 1.5) were calculated with the first and second approaches, respectively. For DC2_{Mano}, the large dispersion of individual pixel isotopic ratio values should lead us to consider these ages with caution, despite the acceptable statistics. The ages correspond to 101.3 \pm 12.6 Ma (MSWD = 1) (first approach) and 106.2 \pm 8.1 Ma (MSWD = 1.1) (second approach). For RD2_{Meillon}, two samples gave reliable ages. For the first sample, taken directly from Meillon doloGST in the vicinity of major fault and dolomite breccias, two images were analyzed. Ages of 140.8 \pm 9.2 Ma (MSWD = 0.4) and 136.6 \pm 9.3 (MSWD = 0.5) were calculated with the first

701 approach, whereas ages of 136.9 ± 4.8 Ma (MSWD = 1.1) and 134.0 ± 4.7 Ma (MSWD =
702 0.8) were obtained with the second. For the second sample, corresponding to a dolomite
703 clast embedded in fault-related calcite cemented breccia, less precise ages of 113.8 ± 16.6
704 Ma (MSWD = 0.5) and 107.0 ± 5.6 Ma (MSWD = 1.3) were calculated depending on the
705 approach used. Finally, for DC4_{Meillon}, ages of 112.7 ± 13.4 Ma (MSWD = 0.5) and $106.1 \pm$
706 5.5 Ma (MSWD = 1.6) were obtained for the first and second approaches, respectively.

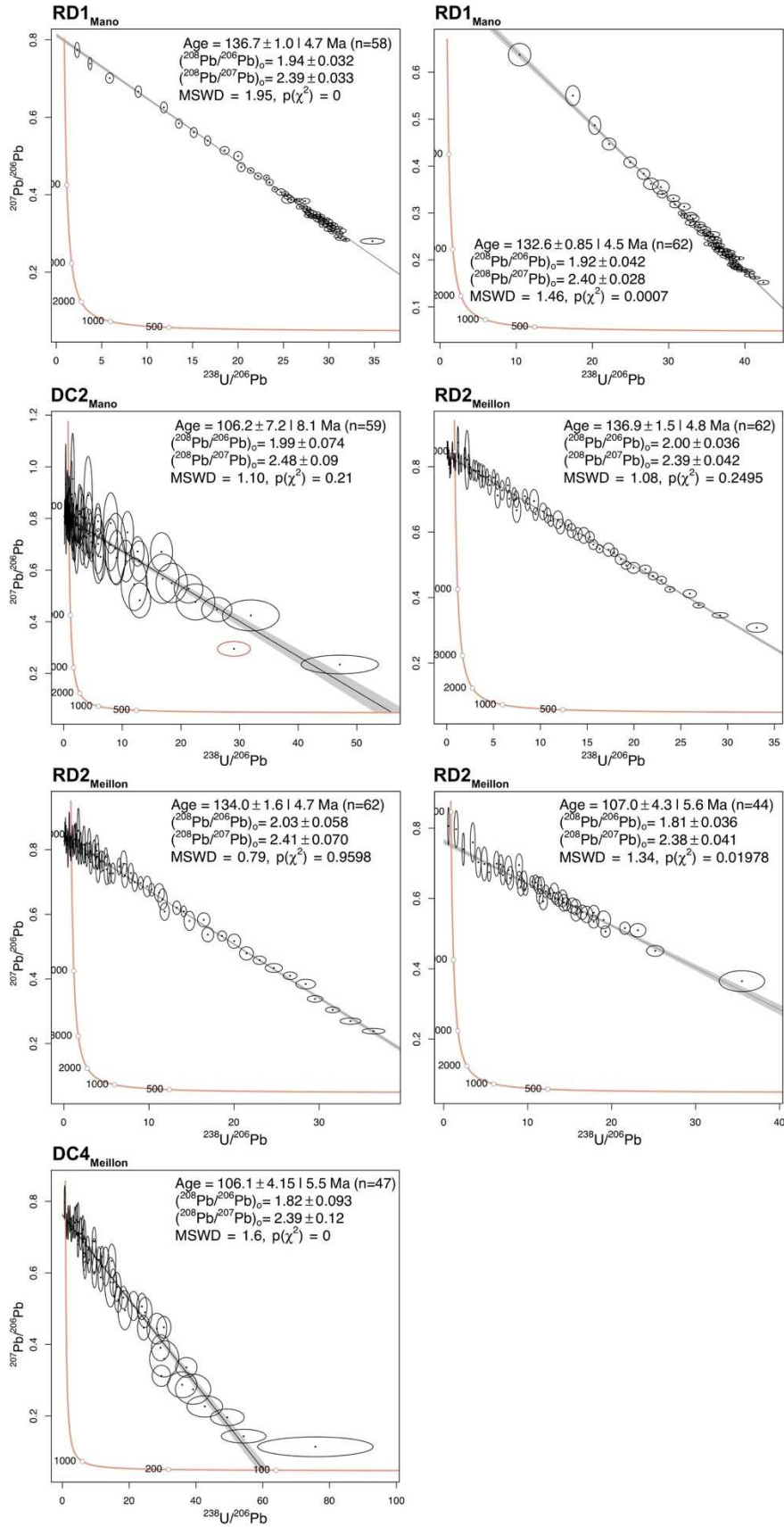


Fig. 12. Total-Pb/U-Th plots for the dolomites successfully dated by the U-Pb method of Drost et al. (2018). All ellipses correspond to two sigma uncertainties. For DC2_{Mano}, the red ellipse was not considered in the age calculation.

4.3.5. Fluid inclusions

4.3.5.1. Petrography of fluid inclusions

The investigated dolomite cements in the breccias of the Meillon and Mano Formations have a high content of aqueous fluid inclusions (FIs). For RD1 and RD2 dolomites, the dark cloudy appearance of the crystals in both formations is due to the presence of numerous primary FIs of less than 2 μm in size.

In the DC2 dolomites of both formations, the dolomite crystals have a cloudy appearance due the presence of presumably primary FIs of less than 5 μm in size, which have a rectangular to oval shape (Fig. 13A). Most FIs are too small to distinguish their phase content (one or two phases). Only seven two-phase (water and gas) FIs could be analyzed.

In the DC3 dolomites of both formations, the FIs have a size of around 4-8 μm with an oval to elongated shape. Most are located along the crystal growth planes and are therefore primary (Fig. 13B). All the aqueous FIs have two phases (water and gas). The presence of very clear growth plans allowed us to precisely locate the FI positions in the crystal subdivision in order to link the measured temperatures to the oxygen isotope values specific to this area. Secondary fluid inclusion assemblages (FIAs) located on the planes intersecting the dolomite growth have been observed. Several FIAs stop at DC4_{Mano} (Secondary A), while others intersect all the dolomite generations (Secondary B). These two-phased FIs postdate DC3 and were trapped before or during the DC4 precipitation.

In DC4_{Mano} dolomites, only a few primary FIs are observed on crystal growth zones. These FIs have a rectangular to elongated shape with a size ranging from 2 to 10 μm (Fig. 13C). About half of these FIs are too small to be reliably described. The others have two phases (water and gas). In the Meillon Formation, several DC4_{Meillon} crystals have a very high primary FI content. These have a rectangular shape ranging from 4 to 20 μm in size (Fig. 13D). Around 90% of these FIs have a size of less than 5 μm , and their content cannot be clearly assessed due to their small dimensions. The larger FIs all have two phases (water and gas).

In quartz, isolated FIs are interpreted as primary inclusions, whereas other FIs aligned along the healed fractures are interpreted as secondary. Both FIs have a two-phase aqueous content (water and gas).

In CC1_{Meillon}, no inclusions exceeding 2 µm could be observed. Finally, CC2_{Meillon} contains a small amount of FIs. These are isolated, not aligned on the fracture planes, and interpreted as primary with two phases.

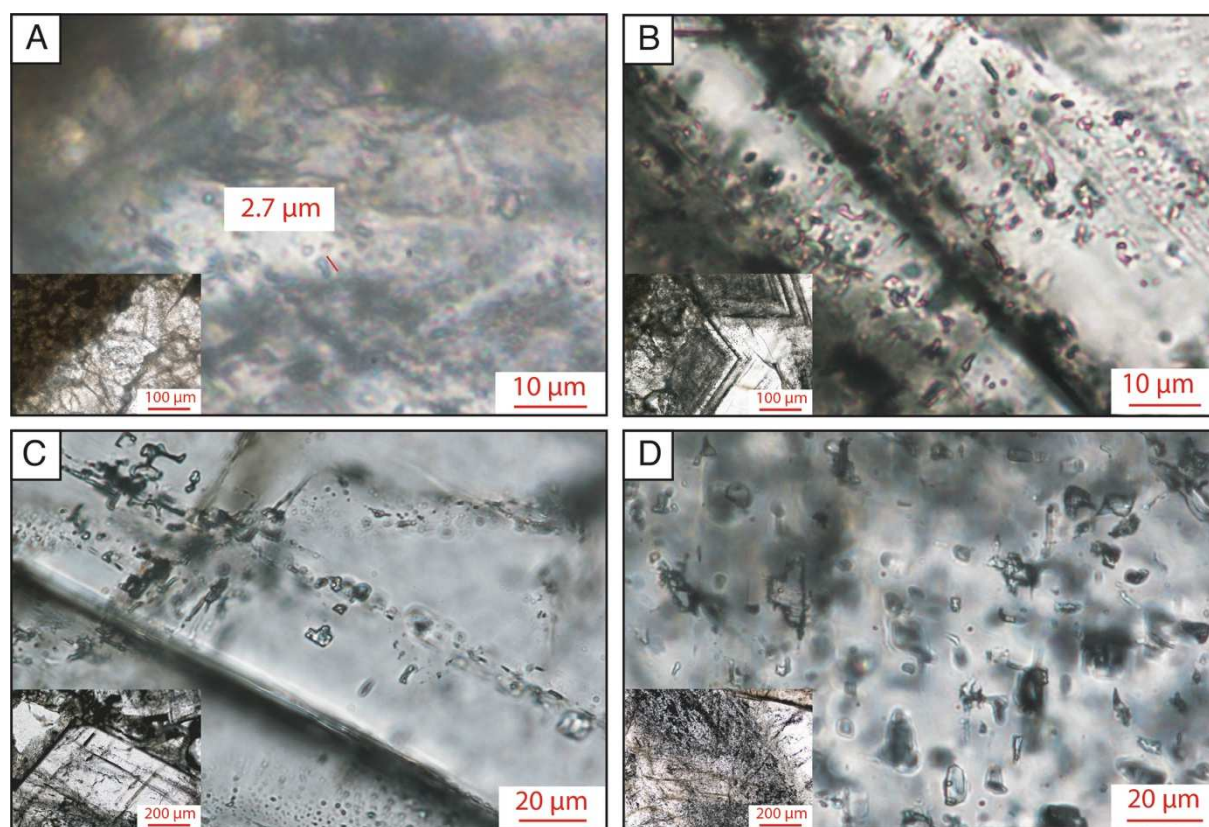


Fig. 13. Overview of the FIs present in the Mano and Meillon dolomite cements. A) Small oval FIs give a cloudy appearance to DC2_{Mano}; B) Primary FIs are located on the crystal growth plans of DC3_{Mano}; C) Rectangular FIs are found along a crystal growth zone in DC4_{Mano}; D) A high number of rectangular FIs occur in DC4_{Meillon}.

4.3.5.2. Microthermometry

The T_h values obtained in the Mano cements are shown in Fig. 14A. DC2_{Mano} yields T_h values ($n = 7$) between 169 and 204°C. The T_h values of DC3a-b_{Mano} range from 146 to 192°C (mode = 157°C; $n = 21$), whereas the T_h values of DC3c_{Mano} vary from 171 to 196°C (mode = 196°C; $n = 20$). The highest T_h values observed in the Mano Formation are in DC4_{Mano} FIs, ranging from 196 to 320°C ($n = 12$). The large distribution of these values

makes it difficult to determine a mode for T_h . Secondary FIs in DC3_{Mano} have T_h values around 200°C (n = 19). Secondary FIs that do not cross DC4_{Mano} have T_h values around 265°C (n = 4).

The T_h values obtained in the Meillon cements are shown in Fig. 14B. In the Meillon Formation, DC2_{Meillon} yields T_h values between 230 and 232°C (n = 4). The T_h values of DC3_{Meillon} range from 179 to 210°C (mode = 207.5°C; n = 18). Similar to the Mano Formation, the highest T_h values measured in the Meillon Formation are in DC4_{Meillon}, the last dolomite cement. These T_h values vary from 237 to 260°C (mode = 260°C; n = 6). Primary FIs of Qtz_{Meillon} have T_h values ranging from 135.5 to 205°C (mode = 205°C; n = 19), whereas the values of secondary FIs vary from 143.5 to 157.5°C (mode = 148.5°C; n = 12). The calcite cement CC2_{Meillon} has T_h values between 141.5 and 157.5°C (n = 5).

4.3.5.3. Raman analysis: Chlorinity

The chlorinity values obtained by Raman analysis are detailed in Fig. 14C. DC2_{Mano} yields chlorinity values comprised between 0 and 3.6‰_{eqNaCl} (mean = 1.6‰_{eqNaCl}; n = 3). For DC3, the values vary from 0 to 4.9‰_{eqNaCl} (mean = 1.5‰_{eqNaCl}) in DC3a-b (n = 4) and from 0 to 12.4‰_{eqNaCl} (mean = 4.9‰_{eqNaCl}) in DC3c (n = 11). The saddle dolomite DC4_{Mano} has the highest chlorinity between 10.2 and 26.9‰ (mean = 19.7‰_{eqNaCl}; n = 4).

In the Meillon Formation, chlorinity was only measured in the DC4_{Meillon} dolomite with values between 12.7 and 23.6‰_{eqNaCl} (mean = 18.2‰_{eqNaCl}; n = 6). The primary and secondary FIs of quartz have a chlorinity ranging from 2.5 to 7.5‰_{eqNaCl} (mean = 5.6‰_{eqNaCl}; n = 12) and 7.7 to 23.9‰_{eqNaCl} (mean = 20‰_{eqNaCl}; n = 12), respectively. CC2_{Meillon} (n = 2) has a chlorinity between 17.7 and 18.2‰_{eqNaCl}.

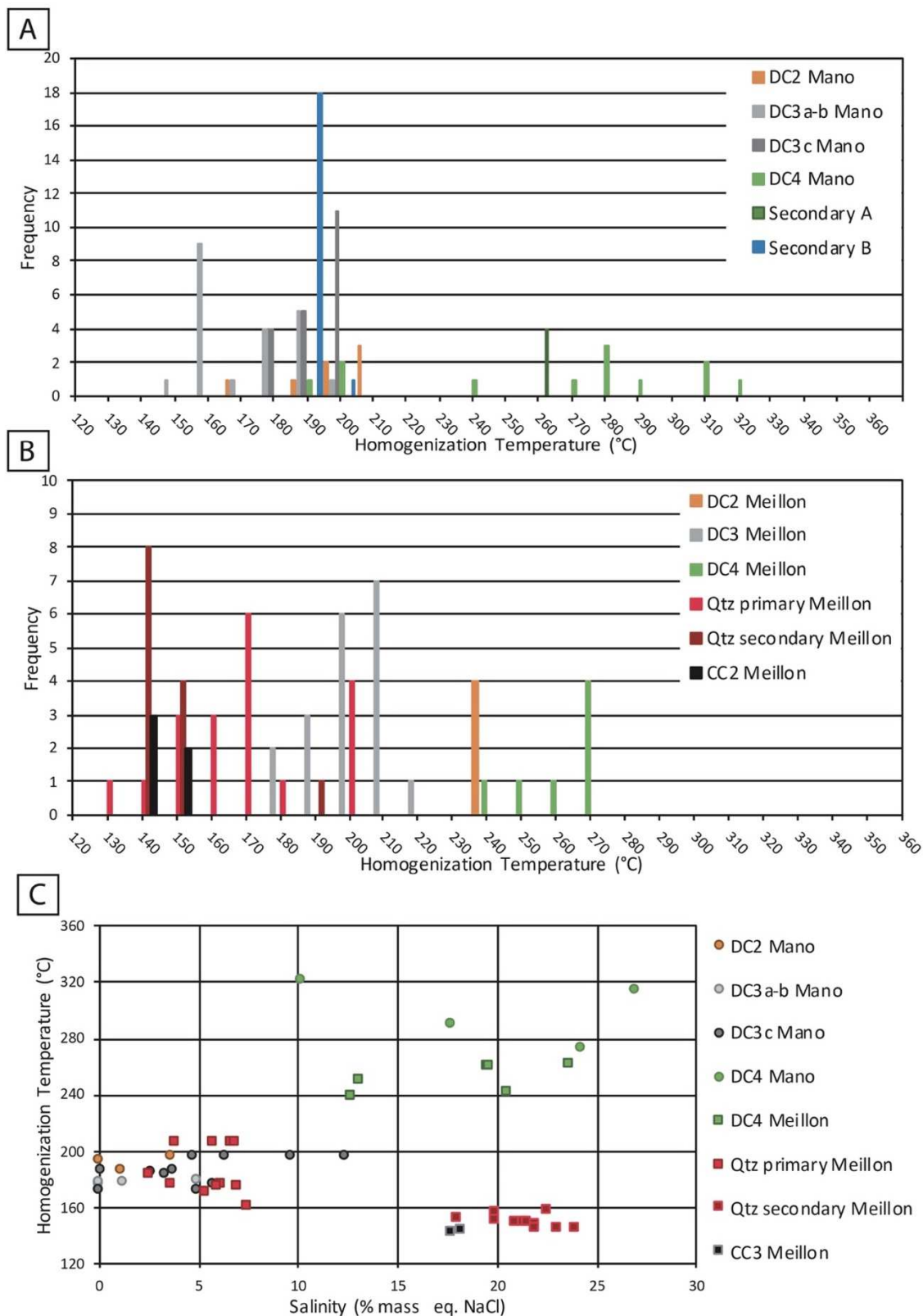


Fig. 14. Results of FI analysis. A) Histogram of homogenization temperatures of aqueous FIs measured in dolomite cements present in Breccia B in the Mano Formation; B) Histogram of homogenization temperatures of aqueous FIs measured in cements present in Breccia C in the Meillon Formation; C) Homogenization temperatures versus chlorinity measured by Raman spectroscopy in Mano and Meillon cements.

4.3.6. Rare earth elements

In the Mano Formation, the shale-normalized REE patterns of all the dolomite phases are similar, except for DC4_{Mano} (Fig. 15A). The low REE (LREE) patterns are flat and thus consistent with the WSA, whereas the high REE (HREE) patterns tend to slightly decrease, being closer to the pattern of hydrothermal fluids. DC4_{Mano} has a distinctive REE pattern, with a strong positive Eu anomaly and a greater decrease in HREE. This entire profile is more consistent with that of hydrothermal vents.

Except for RD1_{Meillon}, the REE patterns of the Meillon dolomites partly differ from those of the Mano dolomites (Fig. 15B). Their LREE patterns present a strong negative Ce anomaly, which is consistent with seawater. By contrast, their HREE patterns are similar to those of the Mano dolomites and thus more consistent with hydrothermal fluids. In addition, the DC4_{Meillon} presents some distinction with a slightly positive Eu anomaly and a greater HREE decrease, closer to the profile of DC4_{Mano}.

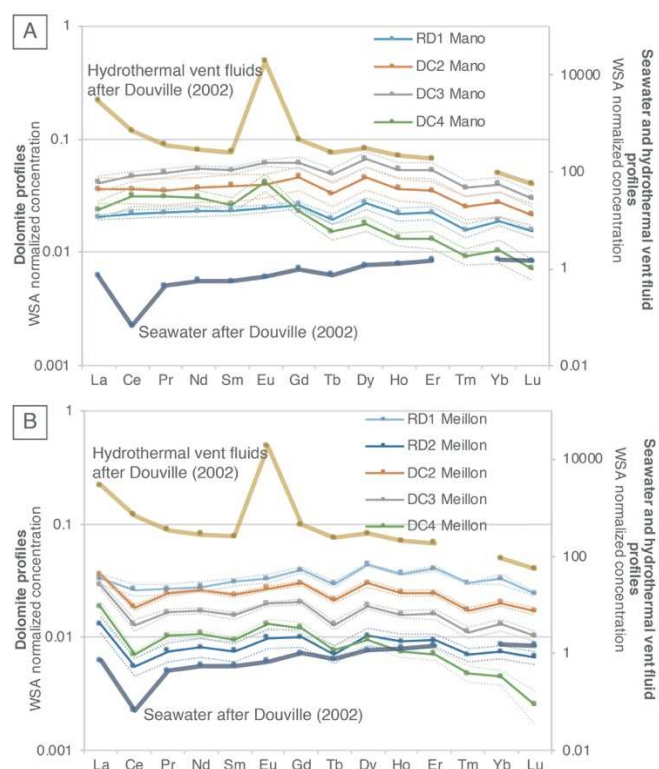


Fig. 15. REE profiles normalized to WSA in Mano (A) and Meillon (B) Formations with standard errors (1s) in dashed lines.

5. Discussion

5.1. Paragenetic sequence

Our study on textural relationships, geochemical trends, FI microthermometry, and absolute age of the precipitation of diagenetic phases allows us to propose a complete paragenetic sequence of the Mano and Meillon Formations from the Early Cretaceous to the Cenozoic (Fig. 16).

The Mano and Meillon carbonate deposits were initially affected by early marine micritization as well as partial oolitic and peloidal grain dissolution. Thereafter, both formations were massively dolomitized during the Early Cretaceous, which is consistent with a near-surface to shallow burial context. In the Mano Formation, only one dolomitization event is recorded (RD1_{Mano}). In the Meillon Formation, remnants of a first dolomitization stage (RD1_{Meillon}) are locally preserved in the wackestone to packstone facies, whereas in the grainstone facies, the initial textures were completely overprinted by a second stage of massive dolomitization (RD2_{Meillon}). Widespread dolomitization probably occurred coevally to dolomite cementation (DC2 and DC3) in both the intercrystalline pores of the dolostones (including breccias) and the tectonic veins. A final stage of saddle dolomite cementation (DC4) occurred locally in the fault zones where it supports the breccias clasts. All dolomite cements, including the dolomite matrix (RD1_{Mano} and RD2_{Meillon}), were either locally dissolved, thus creating solution-enhanced porosity, or directly replaced by calcite cement (CC1). In the residual porosity, subsequent quartz precipitated in the largest voids of several veins and breccias. The final cementation stage identified was only found in the Meillon Formation, with CC2 calcite blocking the residual porosity in large veins and filling new fractures. Finally, a last calcite cement with a rarely observed dripstone fabric (CC3_{Meillon}) filled the residual porosity of the Meillon Formation.

calcite grains is also common, especially in platforms exposed to the ingress of meteoric water during emersion (Bathurst, 1971; James and Choquette, 1984).

5.2.2. Widespread dolomitization in near-surface to shallow burial conditions

In the Mano Formation, an age of $\sim 135 \pm 5$ Ma obtained for RD1_{Mano} indicates that widespread dolomitization occurred between the Berriasian and the Hauterivian. Present-day sedimentary thickness suggests that the maximum burial of the Mano Formation did not exceed 500 m at that time (Castéras et al., 1970), assuming that compaction was limited due to the essential presence of high energy carbonate deposits in the Jurassic and pre-Albian units (dolostones and GST; Croizé et al., 2013; Goldhammer, 1997). We can use the maximum burial to propose an approximate precipitation temperature between $\sim 20^\circ\text{C}$ at the surface to $\sim 35^\circ\text{C}$ at 500 m, assuming a normal geothermal gradient of $30^\circ\text{C}/\text{km}$ (Fig. 17A). The parent water $\delta^{18}\text{O}$ ($\delta^{18}\text{O}_w$) of RD1_{Mano} dolomite calculated for this temperature range, the measured dolomite $\delta^{18}\text{O}$ (-3 to $0.74\text{‰}_{\text{PDB}}$), and the dolomite–water fractionation factor of Horita (2014) range from -5.9 to $+1.2\text{‰}_{\text{SMOW}}$ (Fig. 18). The lowest values are compatible with meteoric water, whereas slightly negative to positive values are more consistent with Early Cretaceous seawater to slightly evolved basinal waters (Longstaffe, 1987; Veizer and Prokoph, 2015). The Sr isotope values are higher than Early Cretaceous seawater (Fig. 11), suggesting an interaction with radiogenic components such as clays or bauxites deposited above the erosive truncation of the Mano Formation or the mixture of marine-derived water and groundwater (e.g., Adams et al., 2019; Nader et al., 2004; Railsback and Hood, 2001). The shale-like LREE pattern corroborates the interactions between radiogenic components, inducing a high water-rock interaction, whereas the HREE tends to slightly decrease and thus is in line with a hydrothermal fluid pattern. Although not fully diagnostic, dolomite and water $\delta^{18}\text{O}$ values, measured $^{87}\text{Sr}/^{86}\text{Sr}$ values, and LREE patterns are in line with RD1_{Mano} dolomitization enhanced by the near-surface reflux of marine-derived water, which interacted with radiogenic components such as clay or mixed with groundwater (Fig. 17A). This mechanism of dolomitization is common in recently emerged carbonate platforms (Adam and

Rhodes, 1960; Adams et al., 2019; Machel, 2004; Warren, 2000). This hypothesis is also consistent with previous studies on the Mano dolostones, which pointed to the presence of an early dolomitization phase linked to emersion and fed by seawater (Grimaldi, 1988). Although this interpretation is preferred, the hypothesis of higher temperature precipitation cannot be ruled out in the absence of more precise thermal constraints. In this case, the fluids causing dolomitization would have had higher $\delta^{18}\text{O}_w$ values, tending toward evaporative or basin signatures. Sr values higher than marine seawater could then be explained by the interaction with radiogenic components such as clay or crustal material (Longstaffe, 1987).

In the Meillon Formation, the U-Pb dating of the main replacive dolomite (RD2_{Meillon}) gives different ages in two distinct samples ($\sim 136 \pm 5$ Ma and 107 ± 5.6 Ma; Fig. 12). The first U-Pb age (Berriasian to Hauterivian), obtained from a dolomite clast embedded in calcite-cemented breccia, is similar within uncertainties to that of RD1_{Mano} (Fig. 16). It is thus interpreted as reflecting the timing of the first dolomitization stage (RD1_{Meillon}), not reset during the subsequent recrystallization to RD2_{Meillon}. Taking this age, RD1_{Meillon} would have formed in near-surface to shallow burial conditions (≤ 1000 m). Using its $\delta^{18}\text{O}$ values (-4.5 to -3.3‰ _{PDB}) with a precipitation temperature between 20°C at the surface and 50°C at 1000 m ($\delta^{18}\text{O}$ ranging from -4.5 to -3.3‰ _{PDB}), $\delta^{18}\text{O}_w$ values of -5 to $+0.2\text{‰}$ are calculated (Fig. 18). These values as well as the REE pattern are very similar to those obtained for RD1_{Mano} dolomite, suggesting similar conditions of formation in near-surface to shallow burial conditions. These simultaneous massive dolomitizations imply a non-compartmentalized hydrologic system (Fig. 17A).

The second U-Pb age of RD2_{Meillon} (Albian) was measured in a dolomite host rock located in the vicinity of a fault-related dolomite breccia. It is comparable within uncertainties to dolomite cement ages obtained in similar breccias in both formations (DC2-3_{Mano} and DC4_{Meillon}; Fig. 16). It is thus interpreted as recording the timing of the recrystallization of

891 RD1_{Meillon} to RD2_{Meillon}, which was more pronounced at the vicinity of major faults. As detailed
892 in the next section, such recrystallization occurred at a higher burial.

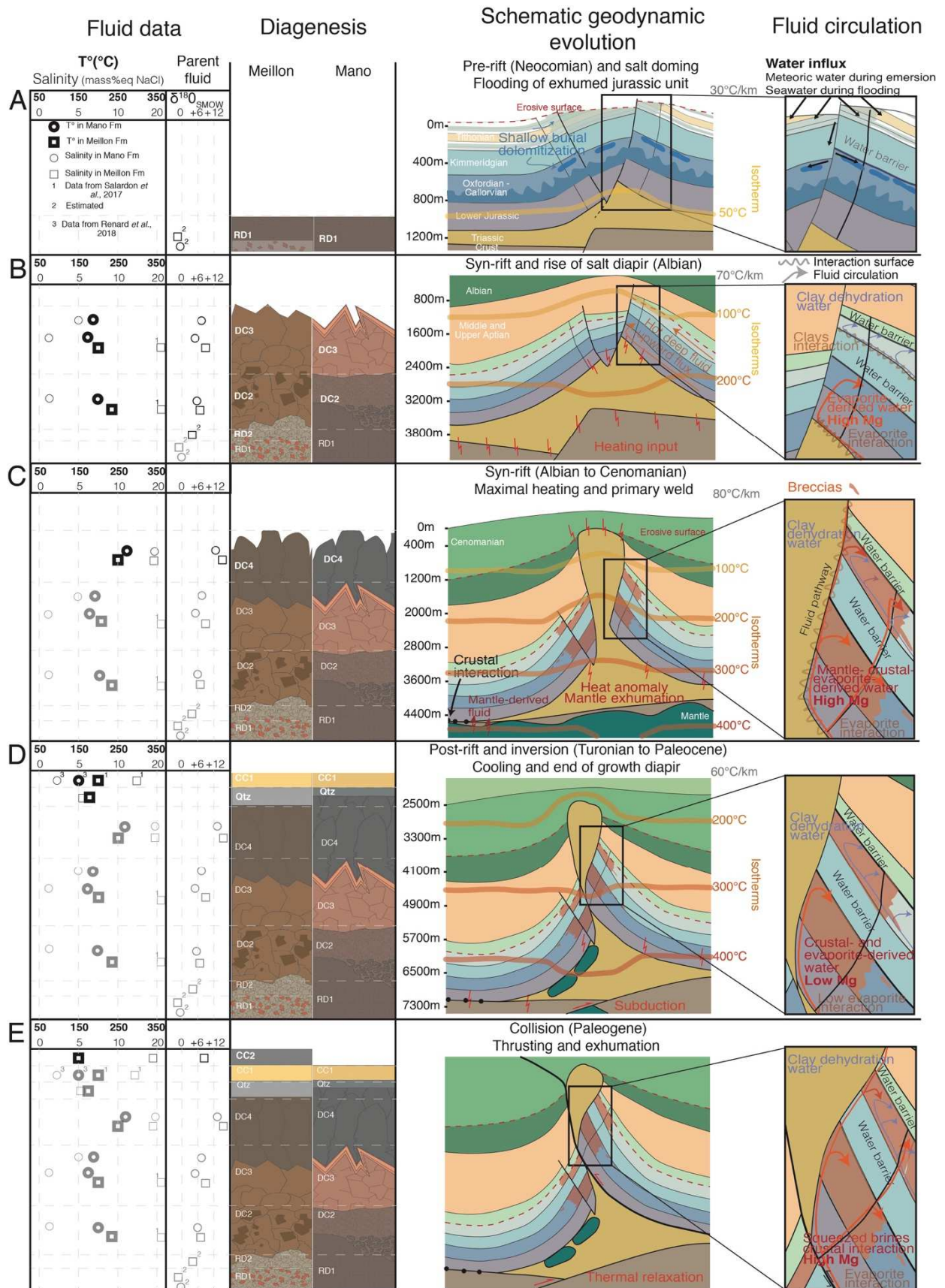


Fig. 17. General model of the evolution of fluid chemistry, fluid circulation, and diagenesis phases set in the schematic reconstruction of the Mail Arrouy *chaînon* and its structural and geochemical evolution. The rightmost sketches detail the inferred fluid circulations in the near-sampled area. The

isotherms were developed based on Corre (2017), Hart et al. (2017), and Vacherat et al. (2014). The thermal anomalies around the salt structures were interpreted from Grunnaleite and Mosbron (2019), Jensen (1983), Kaiser et al. (2011), Mello et al. (1995), Peterson and Lerche (1995), and Selig and Wallick (1966).

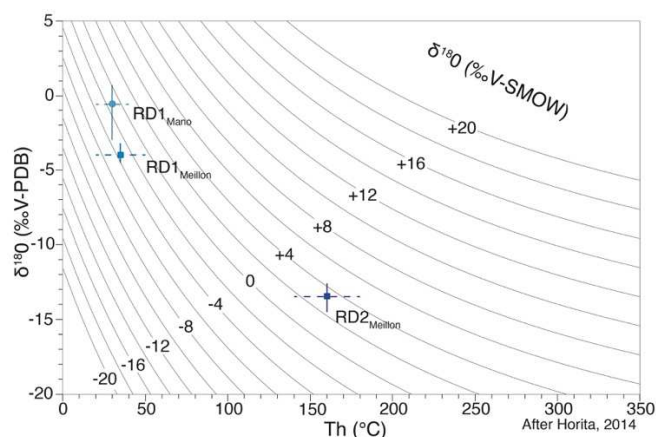


Fig. 18. Fractionation diagram for replacive dolomites using the dolomite–water fractionation factor of Horita (2014). The values of the parent water $\delta^{18}\text{O}$ are calculated from an expected temperature range (dashed lines) and the measured dolomite $\delta^{18}\text{O}$.

5.3. Shallow to deep burial: Toward the widespread influx of crustal fluids

5.3.1. Massive recrystallization of dolomites in the Meillon Formation

In the Meillon Formation, the U-Pb dating of the RD2_{Meillon} points to a recrystallization during the Albian under a burial found at approximatively 1500 to 2000 m (Castéras et al., 1970; Fig. 16). The strongly negative $\delta^{18}\text{O}$ (mean = -13.4‰_{PDB}) makes the precipitation conditions clearly distinct from those of RD1_{Mano} and RD1_{Meillon}. If the precipitation temperature was only controlled by burial (~1500 to 2000 m) under the high geothermal gradient expected during the Albian due to the rifting (~ 80°C/km), RD2_{Meillon} would have formed at a maximum temperature of ~180°C (Corre, 2017; Hart et al., 2017; Vacherat et al., 2014). The corresponding $\delta^{18}\text{O}_w$ values of the RD2_{Meillon} parent water (considering a $\delta^{18}\text{O}$ ranging from -14.5 to -12.6‰_{PDB}) would then range from +0.6 to +5‰_{SMOW}, pointing to the heavy basinal water interacting with the host rock (Longstaffe, 1987; Fig. 18). This would be consistent with the Sr isotope ratio measured in RD2_{Meillon}, similar to the Triassic marine carbonate values (Fig. 11). Hot water would have possibly interacted with the Triassic evaporites located only 500 m below and flowed up in the Meillon Formation (Castéras et al., 1970; Fig. 17B). The seawater-like REE pattern measured in RD2_{Meillon} is in line with this

interpretation, pointing to an interaction with marine water. In this case, these waters would not have reached the Mano Formation due to the presence of poorly permeable Lons Limestones, which were compacted at that time (Biteau et al., 2006). Thus, RD2_{Meillon} dolomitization occurred as the hydrologic systems of the Mano and Meillon Formations were compartmentalized.

5.3.2. DC2 and DC3 cementations in compartmentalized reservoirs

In the Mano Formation, the first two cements (DC2_{Mano} and DC3_{Mano}) are ubiquitous. The U-Pb dating of DC2_{Mano} constrains the timing of the precipitation to between ~114 and ~98 Ma, corresponding to the Aptian to Albian time interval (Fig. 16). FIs indicate cementation at temperatures of at least 160°C, higher than those estimated in the host rock at this age (100 to 140°C at 1000 to 1500 m). The dolomite cementations probably occurred under the hydrothermal regime, which is consistent with previous studies on dolomitization in the northwestern Pyrenees (Corre et al., 2018; Iriarte et al., 2012; Lopez-Horgue et al., 2010; Nader et al., 2012; Renard et al., 2018; Salardon et al., 2017).

These dolomites are characterized by a significant negative shift in the $\delta^{18}\text{O}$ values compared with the host rock and previous cements (Table 2). Considering FI temperatures (146 to 204°C) and the oxygen isotope ratio measured in DC2_{Mano} and DC3_{Mano} (-14.7 to -9.4‰_{PDB}), the calculated $\delta^{18}\text{O}_w$ ranges from +1 to +10‰_{SMOW} (mean = +5.9‰_{SMOW}; Fig. 19). Such positive values are consistent with heavy basinal water interacted with the host rock (Longstaffe, 1987). The high Sr isotope ratios measured in these cements are in line with this interpretation (Fig. 11). In addition, the low chlorinity measured in the FIs (Fig. 17B) points to an absence of interaction with the underlying Triassic evaporites. Low chlorinities are better explained by a meteoric water source or clay dehydration (Chaudhuri and Clauer, 1992; Longstaffe, 1987 and reference therein; Mountjoy et al., 1992; Wilkinson et al., 1992). The REE profiles of both DC2_{Mano} and DC3_{Mano} dolomite cements are very similar to that of RD1_{Mano}, which has a shale-like pattern. These REE patterns, in addition to the high $\delta^{18}\text{O}_w$ values, tend to favor clay dehydration as the main source of dolomite-saturated water. In this

case, the Lons Formation, located just below the Mano unit, could be a source of clay-related water. Clay dehydration could have provided some Mg in addition to the existing RD1_{Mano} (e.g., Elias Bahnan et al., 2020; McHargue and Price, 1982; Mountjoy et al., 1992).

In the Meillon Formation, the U-Pb dating of the previous and later cements suggests a Barremian to Albian age development for DC2_{Meillon} and DC3_{Meillon} (Fig. 16; RD2_{Meillon} and DC4_{Meillon}, with ages of ~136 Ma and ~106 Ma, respectively), which explains the high primary FI temperatures (180-230°C). The similar $\delta^{18}\text{O}$ values between RD2_{Meillon} and DC2_{Meillon} suggests precipitation in close conditions. The calculated $\delta^{18}\text{O}_w$ of DC2_{Meillon} ranges from +4.6 to +10.1‰_{SMOW} (mean = +6.9‰_{SMOW}), whereas in DC3_{Meillon}, it ranges from +7.4 to +11.6‰_{SMOW} with a higher mean value of +9.7‰_{SMOW} (Fig. 19). This indicates a change to the heavier parent water $\delta^{18}\text{O}$ values over time at a constant temperature. The Sr isotopic ratio of the mixture of both cements lies in the range of the Triassic marine cement values (Fig. 11). Although the chlorinity of the parent fluid could not be measured, it can be expected to be high based on the study of Salardon et al. (2017), who found water with high chlorinity in similar dolomite cements of the Meillon Formation. The REE profiles measured in these cements are similar to that obtained in RD2_{Meillon} with a seawater pattern. However, our data and those of Salardon et al. (2017) strongly suggest that DC2_{Meillon} and DC3_{Meillon} cements precipitated from isotopically heavy evaporite-derived water with high chlorinity. This interpretation differs from that of Salardon et al. (2017), who suggested a magmatic water source. This highlights once again a clear compartmentalization between the Mano and Meillon reservoirs (Fig. 17B). For RD2_{Meillon}, DC2_{Meillon}, and DC3_{Meillon}, it is likely that the Mg was provided in part locally by RD1_{Meillon} (e.g., Gao et al., 1995; Gisquet et al., 2013; Guo et al., 2016; Montanez, 1994; Zhang et al., 2009). However, the external brines with a Triassic signature could have supplied part of the Mg necessary for precipitation, which would not be surprising in a context of salt tectonics (Davies and Smith Jr, 2006; Krupp, 2005; Quesnel et al., 2019; Wendte et al., 1998).

5.3.3. Saddle dolomite DC4: Last dolomite cementation in the connected reservoirs

This last dolomite cement could only be dated to the Meillon Formation (DC4_{Meillon}), where it also formed during the Albian (Fig. 16). In both formations, saddle dolomites are characterized by higher precipitation temperatures (> 250°C) and oxygen isotope ratios compared to previous cements (Table 2). In the Mano Formation, the corresponding parent water oxygen isotope ratios range from +6.1 to +16.8‰_{SMOW} (mean = +12.8‰_{SMOW}), whereas in the Meillon Formation, they range from +11.4 to +17.1‰_{SMOW} (mean = +14.5‰_{SMOW}; Fig. 19). In both formations, the chlorinity measured in the FIs reaches 20‰_{eqNaCl}. Although this corresponds to a very strong increase in the Mano Formation, it is more in line with the values measured in previous cements in the Meillon Formation, as evidenced by Salardon et al. (2017) (Fig. 17C). These high chlorinities as well as the high $\delta^{18}\text{O}_w$ suggest the influence of Triassic evaporites, added to the significant increase in the water-to-rock ratio (Land and Prezbindowski, 1981; Longstaffe, 1987). Given the absence of clastic rocks in the Mano Formation and the Triassic evaporites, the very high Sr isotope ratios measured in DC4_{Mano} (> 0.71; Fig. 11) necessarily imply contributions from the Paleozoic basement (Banner, 1995; Chaudhuri and Clauer, 1992). The low Sr ratios of the volcanic rocks exclude any interactions with magmatic-related fluids (Fig. 11). Moreover, the REE profiles of both DC4 dolomite cements differ from those measured in other dolomites. They present a positive Eu anomaly (very strong for DC4_{Mano} and less pronounced for DC4_{Meillon}) and a decrease in the HREE content compared to LREE (Fig. 15). These characteristics mimic those of the fluids hosted by ultramafic rocks like peridotites (e.g., Douville et al., 2002, 1999; Tostevin et al., 2016). It is thus likely that dolomitizing waters also interacted with the mantle located below the thinned continental crust or even exhumed. Mantle serpentinization reactions are known to release large amounts of Mg, which may have contributed to dolomite precipitation (Breesch et al., 2010; Chen et al., 2016; Debure et al., 2019; Koeshidayatullah et al., 2020; Pinto et al., 2017; Salardon et al., 2017). Finally, DC4 precipitated from water resulting from a mixture of evaporite-, crustal-, and mantle-derived waters, each of which was able to

provide part of the Mg necessary for precipitation to occur. A simple scenario would be that mantle-derived fluids migrated upward through the residual crust and Triassic evaporites. These saddle dolomites are located near faults, indicating that these fluids were channeled by the fault network, which acted as pathways between the Mano and Meillon reservoirs (Fig. 17C). This interpretation is consistent with several studies on dolomitized carbonate platforms, which highlight similar diagenetic evolutions, especially the role of faults on high temperature dolomitization (Barale et al., 2016; Duggan et al., 2001; Haeri-Ardakani et al., 2013a, 2013b; Lopez-Horgue et al., 2010; Mozafari et al., 2019).

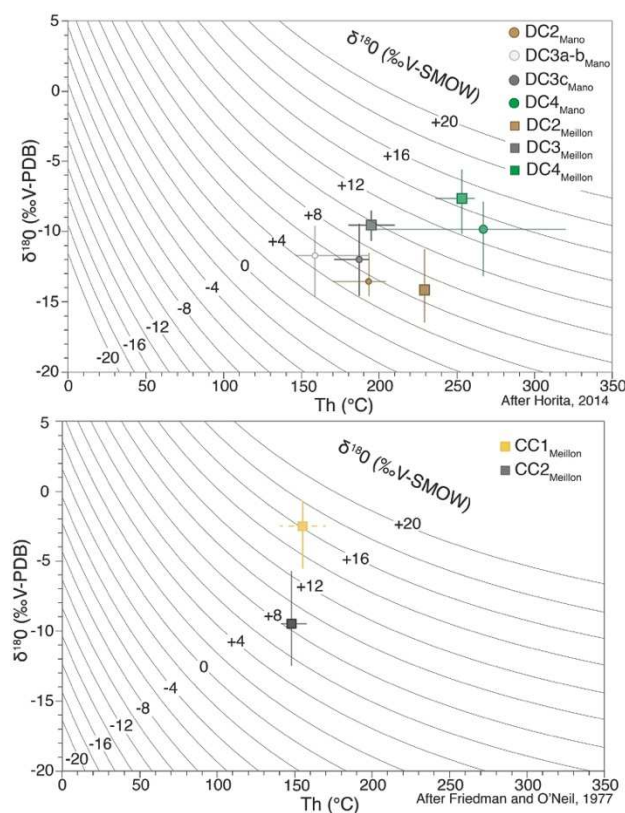


Fig. 19. Fractionation diagram for dolomite cements using the dolomite–water fractionation factor of Horita (2014) and calcite cements using the calcite–water fractionation factor of Friedman and O'Neil (1977). The dashed line for CC1_{Meillon} values corresponds to the expected temperatures using the data of Salardon et al. (2017).

5.4. Deep burial to exhumation: From dolomite- to quartz- and calcite-saturated waters

5.4.1. Quartz precipitation: Influx of diluted waters in the Meillon Formation

Following the dolomite cementation, both the Mano and Meillon Formations were affected by local dedolomitization. This marks a change in the composition of the waters

and/or of pressure-temperature conditions, leading to dolomite undersaturation (e.g., Brauer and Baker, 1984). According to the U-Pb dating of DC4 cement, the dolomite dissolution or replacement occurred after ~100 Ma, corresponding to the post-rift phase and/or Pyrenean shortening (Puigdefàbregas and Souquet, 1986). This evolution of the water composition is also recorded during the subsequent precipitation of quartz, which partially blocked the residual intercrystalline porosity (Table 2). FIs measured in quartz from the Meillon Formation record a significant decrease in chlorinity and lower temperatures compared with DC4, which is compatible with precipitation during shortening (Vacherat et al., 2016, 2014). These lower values may explain the transition from carbonate to silica-saturated waters due to the retrograde solubility of dolomite. The low chlorinity also shows a decreasing interaction with Triassic evaporites, clearly indicating a change in the water migration pathways. This would be better explained by the influx of meteoric waters or by clay dehydration. The latter is preferred given (1) the still high temperatures recorded by primary FIs (~170°C), which is compatible with significant burial at the time of quartz precipitation, and (2) the nearby presence of clay-rich formations (Lons Limestones and overlying flysch deposits). Silica necessary for quartz precipitation was provided by these formations (e.g., Hesse, 1987) or interaction with the basement (e.g., Bustillo, 2010), but neither of these hypotheses can be excluded based on the available data.

5.4.2. Calcite cementation: Second stage of reservoir compartmentalization

The paragenetic relationships between quartz and calcite cements CC1 to CC3 could not be firmly established. However, based on the presence of calcite-cemented dissolution vugs in quartz, Salardon et al. (2017) proposed that quartz precipitated before calcite in the study area. This would constrain calcite to have likely precipitated during the Pyrenean shortening.

The first calcite cement CC1 is characterized by $\delta^{18}\text{O}$ values of around -2.6‰, the highest value of all the calcite cements. The absence of FI data prevents the characterization of the parent water composition. However, considering the T_h of ~170°C measured in quartz

and the T_h of $\sim 140^\circ\text{C}$ measured in CC2, it is likely that the precipitation temperature of CC1 is in the range of 140 to 170°C . Using these temperatures and the calcite-water oxygen isotope fractionation factor of [Friedman and O'Neil \(1977\)](#), this gives an isotopic value in the range of +11.5 to +17.2‰_{SMOW} ([Fig. 19](#)), pointing to a very high water-to-rock ratio. In the Mano Formation, the study of [Renard et al. \(2018\)](#) shows that the first calcite cementation after dolomitization took place at $\sim 150^\circ\text{C}$ with very low chlorinity water (range between 1.2 and 4.4‰_{eqNaCl}). In the Meillon Formation, according to [Salardon et al. \(2017\)](#), the calcites formed at $\sim 200^\circ\text{C}$ with high chlorinity water (range between 13 and 16‰_{eqNaCl}). Such contrasting chlorinities imply that the Mano and Meillon Formations were once again compartmentalized during the calcite precipitation. Whereas the low chlorinities in the Mano Formation may indicate dilution with clay-dehydration water, the high chlorinities and temperatures in the Meillon Formation point again to the influx of water interacting with the Triassic evaporites in contrast with the previous quartz cements ([Fig. 17D](#)).

The CC2 calcite cement, which is only observed in the Meillon Formation, is mainly associated with breccias located near the fault zones, suggesting fluid circulation during fault activity ([Heydari, 1997](#); [Oliver, 1986](#); [Fig. 17E](#)). The CC2 cement was formed from high chlorinity water, similar to CC1_{Meillon} but at a lower temperature ($< 150^\circ\text{C}$), which is consistent with the decreasing depth during exhumation ([Table 2](#)). The calculated $\delta^{18}\text{O}$ of the parent water ranges from +4.5 to +9.8‰_{SMOW} ([Fig. 19](#)). This parent water has the same characteristics as that described for the cement CC2 of [Salardon et al. \(2017\)](#). These authors suggested that given the negative $\delta^{13}\text{C}$ values, the parent water of this cement was of meteoric origin. Assuming that their CC2 cement is the same as our CC2 calcite, this interpretation is not consistent with the calculated $\delta^{18}\text{O}_w$ or their very high chlorinity, which is more typical of the heavy basinal water and still points to interactions with evaporites at a depth.

The last CC3 calcite cement was observed in the intercrystalline porosity of the Meillon Formation. This cement has a dripstone fabric (microstalactitic cement), which is

1075 consistent with a vadose environment ([Moore and Wade, 2013](#); [Scholle and Ulmer-Scholle,](#)
1076 [2003](#)). The CC3 cement probably marks the final exhumation of the area with the influx of
1077 meteoric water (e.g., [Martín-Martín et al., 2015](#)).

Sample	Stable isotopes												Sr isotopes				Primary fluid inclusions							
	Corrected $\delta^{18}\text{O}_{\text{PDB}}$				Parent water $\delta^{18}\text{O}_{\text{SMOW}}$			$\delta^{13}\text{C}_{\text{PDB}}$					$^{87}\text{Sr}/^{86}\text{Sr}$				Microthermometry				Chlorinity			
Type	Mean	Min	Max	n	Mean	Min	Max	Mean	Min	Max	n	Mean	Min	Max	n		Mode	Min	Max	n	Mean	Min	Max	n
RD1 _{Mano}	-0.7	-3.0	0.7	7				3.1	0.6	4.6	6	0.707633	0.707461	0.707798	3									
DC2 _{Mano}	-13.6	-14.7	-11.5	22	5.4	2.7	8.2	3.2	-1.7	5.7	18						200	169	204	7	1.6	0	3.6	3
DC3a _{Mano}	-13.1	-14.4	-10.2	7				4.1	3.4	4.9	3													
DC3b _{Mano}	-11.0	-12.6	-9.7	9	5.6	0.9	9.6	3.9	2.5	5.1	5	0.708743	0.708484	0.709001	2		160	146	193	21	1.5	0	4.9	4
DC3c _{Mano}	-12.0	-14.6	-9.4	19	6.8	3.0	9.9	3.5	0.8	5.2	17						200	171	196	20	4.9	0	12.4	11
DC4 _{Mano}	-9.9	-13.1	-8.0	29	12.8	6.2	16.8	2.9	0.3	4.9	23	0.710087	0.710043	0.710130	2		280	196	320	12	19.7	10.2	26.9	4
RD1 _{Meillon}	-4.0	-4.5	-3.3	4				3.9	-0.7	7.4	4	0.707555	0.707520	0.707590	2									
RD2 _{Meillon}	-13.4	-14.5	-12.6	3				1.1	-1.4	3.7	2	0.707705	0.707630	0.707780	2									
DC2 _{Meillon}	-14.3	-16.5	-11.1	21	6.9	4.6	10.1	1.2	-3.4	5.2	12						230	230	232	4				
DC3 _{Meillon}	-9.6	-10.8	-8.6	4	9.7	7.4	11.6	1.3	-1.4	4.1	3	0.707875	0.707821	0.707929	2		200	179	210	18				
DC4 _{Meillon}	-7.7	-10.1	-5.7	12	14.5	11.4	17.1	1.0	-2.9	4.5	7	0.708010	0.707900	0.708120	2		260	238	260	6	18.2	12.7	23.6	6
Qtz _{Meillon}																	170	136	205	19	5.6	2.5	7.5	12
CC1 _{Meillon}	-2.6	-5.6	-0.6	13																				
CC2 _{Meillon}	-9.5	-12.5	-6.8	11	8.1	4.5	9.8					0.707770			1		140	142	158	5	18	17.7	18.2	2

1078 Table 2. Geochemical characterization of all the diagenetic phases observed in the Mano and Meillon Formations of the Mail Arrouy *chaînon*, including stable
1079 isotopes ($\delta^{18}\text{O}$, $\delta^{13}\text{C}$, $^{87}\text{Sr}/^{86}\text{Sr}$ measured, and $\delta^{18}\text{O}$ parent water calculated) and FI analysis (microthermometry and chlorinity determination).

5.5. Local controls on dolomitization

5.5.1. Limited role of the carbonate facies

The carbonate matrix of the Mano and Meillon Formations has been largely affected by dolomitization, occurring as replacive dolomite (RD1_{Mano}, RD1_{Meillon}, and RD2_{Meillon}) or porosity-infilling cement (DC2 and DC3). In the Mano Formation made of MST and WST facies, early dolomitization by RD1_{Mano} was ubiquitous. On the contrary, in the Meillon Formation, early dolomitization (RD1_{Meillon}) was more pronounced in the oolitic and peloidal grainstones compared to mudstone and packstone facies, with the latter showing isolated rhombs. Thus, despite relatively similar conditions of deposition, the two formations considered here show the contrasting impact of carbonate facies on early dolomitization. The same applies to late dolomites (RD2_{Meillon}, DC2, and DC3). Whereas RD1_{Mano} was largely preserved in the Mano Formation, with only small volumes of DC2_{Mano} and DC3_{Mano} cements in veins and residual porosity, RD1_{Meillon} was almost entirely overprinted in the Meillon Formation by RD2_{Meillon} (and locally affected by DC2_{Mano} and DC3_{Mano}). This difference can be simply explained by the presence of the Lons Formation above the Meillon Formation, as the former acted as a seal, thus limiting the upward flow of deep hot waters. Therefore, as will be discussed below, the role of the stratigraphic architecture seems to have been primordial compared to that of the carbonate facies.

5.5.2. Late dolomitization: Interplays between faults and sedimentary breccias

In contrast to the previous cements, saddle dolomite DC4 only precipitated in association with breccias that presented a fracture geometry in the vicinity of faults (**Fig. 3**). The similarities of the parent fluids in the DC4 of the Mano and Meillon Formations suggest that these faults acted as a conduit channelizing the fluids in both units. Similar fault-controlled dolomitization has been suggested in several studies conducted in proximity ([Iriarte et al., 2012](#); [Lopez-Horgue et al., 2010](#); [Nader et al., 2012](#); [Salardon et al., 2017](#); [Shah et al., 2010](#)) and in other carbonate platforms worldwide ([Barbier et al., 2015, 2012](#); [Duggan et al., 2001](#); [Haeri-Ardakani et al., 2013a](#); [Hendry et al., 2015](#); [Koeshidayatullah et](#)

al., 2020; Martín-Martín et al., 2015; Mountjoy and Halim-Dihardja, 1991; Mozafari et al., 2019; Rustichelli et al., 2017; Stoakes, 1987; Wendte et al., 2009; Zhang et al., 2009).

However, a peculiarity of the late dolomitization in the Mail Arrouy relates to the presence of bedding parallel breccias extending from the fault zones over several hundred meters (Fig. 17). These mosaic breccias (Breccia B) pass laterally to karst-related sedimentary-collapse breccias (Breccia A). The dolomite mud that supports the fragments of sedimentary breccias was replaced by saddle dolomites with a rough irregular front, creating a mosaic breccia-like morphology with dolomite white cement (Fig. 3). Here, it is thus clear that the mosaic breccias (Breccia B) result from a process of neomorphism rather than the more commonly proposed process of hydraulic fracturing despite the textural similarities. If neomorphism has been largely studied, for example, in experiments of mineral replacement (Pedrosa et al., 2016; Putnis, 2009, 2002), to our knowledge, this is the first time that “neomorphic dolomite breccia” has been described from field observations. Nevertheless, regardless of the brecciation mechanism, saddle dolomitization is firstly fault-controlled and then locally with a stratabound geometry considering the horizontal distribution of karstification and sedimentary breccias.

5.6. Impact of the geodynamic context on the diagenetic record

5.6.1. Pre-rifting and salt tectonics

The first RD1 dolomitizations were associated with shallow burial to emersion, enabled by the inflow of seawater during the Late Jurassic and Early Cretaceous emersion. Massive seawater dolomitization directly resulted from the combined effect of a regional uplift and the initiation of salt doming in the *Chaînon Béarnais* linked to the early stage of rifting (Canérot et al., 2005; Canérot and Lenoble, 1993; Izquierdo-Llavall et al., 2020; James and Canérot, 1999; Labaume and Teixell, 2020). The seawater influx was likely favored by rift-related faulting both in the basement and at the crest of the anticlines formed above the salt domes (e.g., Fischer et al., 2013; Moragas et al., 2020).

5.6.2. Syn-rift and diapirism

In the Meillon Formation, the massive RD2_{Meillon} dolomitization, dated to 107 +/- 5.6 Ma as well as the dolomite cements DC2_{Meillon} and DC3_{Meillon}, filling pores, fractures, and breccias exhibit post-Neocomian to Albian ages, resulting from the circulation of Triassic evaporite-derived water (Fig. 17B). The inflow of these fluids occurred during the syn-rift period, characterized by a gradual increase in the geothermal gradient due to the crustal thinning, beginning with mantle exhumation, volcanic activity, and in the cover layer, the rise of salt diapirs and ridges in response to the faulting of the sedimentary cover (Brinkmann and Lögters, 1968; Canérot et al., 2005; Clerc et al., 2015; Corre et al., 2016; Golberg and Leyreloup, 1990; Izquierdo-Llavall et al., 2020; Jammes et al., 2010a; Labaume and Teixell, 2020; Lagabrielle et al., 2010). The upflow of hot water could have been favored by the rise of the salt diapir due to the enhanced focused fluid flow along the impervious diapir boundaries and the enclosing rocks as well as the accumulation of heat at the top of the structure that generates thermal convection (Fig. 17B; Grunnaleite and Mosbron, 2019; e.g., Jackson and Hudec, 2017 and references therein; Jensen, 1983; Kaiser et al., 2011; Mello et al., 1995; Selig and Wallick, 1966).

In the Mano Formation, the lack of recrystallization related to the circulation of Triassic evaporite-derived water is due to stratigraphic compartmentalization. Only dolomite cements (DC2_{Mano} and DC3_{Mano}) precipitated in the entire Mano Formation during the syn-rift due to the circulation of clay-derived water under the hydrothermal regime. Although the upflow of hot water was probably favored by the rise of salt diapir as in the Meillon Formation, it was limited to the compartmentalized Mano Formation (Fig. 17B).

The last dolomite DC4, also precipitated during the Albian, records the highest temperatures observed in the diagenetic cements, which is consistent with the high temperatures measured in the host rock (Corre, 2017; Izquierdo-Llavall et al., 2020). This period also corresponds to the maximum growth of salt diapirs and associated halokinetic folds (Canérot et al., 2005). Following the rise of the Mail Arrouy salt wall, its progressive

welding (Labaume and Teixell, 2020) may have created fluid pathways at the contact between the salt and the enclosing rocks by means of faulting and fracturing, connecting both formations to the hot water initially present only in the lower compartment (Meillon; Fig. 17C). Crustal interaction recorded by the saddle dolomite implies that the seal formed by the Triassic salt was breached by welding, salt flow, or salt dissolution, thus allowing the ascent of basement-derived waters (Jackson and Hudec, 2017; Fig. 17C).

Therefore, tectonics exerted strong control on the fluid circulation and associated dolomitization by creating pathways through faults and fracture networks as well as along the diapir boundaries. This consequently had an important effect on the diagenetic evolution of the carbonate platform in accordance with other studies conducted in similar tectonic settings (Callot et al., 2010; Gonzalez et al., 2012; Roure et al., 2010, 2005; Vilasi et al., 2009).

5.6.3. Post-rift and Pyrenean compression

Dolomite cements are followed by the precipitation of quartz, which likely occurred during the post-rift stage (Fig. 16). At that time, the burial temperature gradually decreases but remained high due to a blanketing effect (Vacherat et al., 2014). More locally, FIs demonstrate that the parent water became more diluted, which, combined with the temperature decrease, probably favored the transition from a dolomite- to quartz-saturated composition. The lower contribution of salt to the water composition could be explained by the continued salt evacuation related to the ongoing diapirism during the post-rift phase (Fig. 17D).

The last identified cements are calcites, which filled fractures and breccias. The precipitation temperatures recorded by the FIs are the lowest of all cements ($T < 150^{\circ}\text{C}$), testifying to the exhumation of the area during the Pyrenean shortening. However, chlorinity increases significantly compared to quartz, suggesting a renewed interaction with evaporites. During the Pyrenean compression, salt tectonic structures resumed through squeezing, while some of them were thrust (Canérot et al., 2005; Izquierdo-Llavall et al., 2020). The reactivation of these existing structures may have generated the pumping and expulsion of

basinal brines at the origin of the calcite cementation (Fig. 17E). The presence of squeegee-type flow is consistent with the observation of Salardon et al. (2017) and several other studies on fold and thrust belts (Al-Aasm et al., 2019; Beaudoin et al., 2014; Machel and Cavell, 1999; Oliver, 1986; Roure et al., 2010).

5.7. Implications for exploration

More than 90% of the dolomite identified in the Mano and Meillon Formations concern RD1_{Mano} and RD2_{Meillon}, which formed from fluids with distinct geochemical characteristics and at different ages, likely due to the presence of Lons Limestones between both formations. Replacive dolomitization was thus controlled at a large scale by the sedimentary architecture of the carbonate platform, resulting in the development of two largely unconnected dolomite reservoirs. Except for the last episode of dolomite cementation DC4, compartmentalization was effective during all the subsequent records of cement precipitation, from the syn-rift to the inversion stages. Influencing the reservoir diagenesis, compartmentalization effects should also be considered in hydrocarbon migration.

Whereas dolomitization in the Mano Formation can be explained by the seepage of marine-derived water, the influx of deep hot water is required in the Meillon Formation. These fluids most likely originated from the large layer of pre-rift salt located below the carbonate platform. Significant heat caused by the thinning of the passive margin during the syn-rift stage may have triggered an upward fluid flow by thermal convection. The combination of a thick salt layer and an abnormal heat flux resulted in the complete dolomitization of a reservoir unit associated with gas generation and storage in the Aquitaine Basin (Biteau et al., 2006). This also led to the development of drains with dyke-like brecciated conduits as well as saddle dolomite geobodies. Thus, hyperextended passive margins might be important targets in the exploration of reservoirs, provided that thick salt layers were deposited. The combined presence of a carbonate platform in this hot context close to the evaporites could have generated large volumes of dolomites, thus releasing essential porosity for the storage of georesources, even if reservoirs in this context can also be

affected by dolomite cementation by blocking previously created porosity. This case study clearly demonstrates the usefulness of applying multidisciplinary and integrated workflows to better understand the evolution of complex diagenetic systems such as salt-rich hyper-thinned passive margins.

6. Conclusion

The diagenetic evolution of the dolomitized Jurassic carbonate platform of the northwestern Pyrenees, which comprises two major oil and gas reservoir analogues (Mano and Meillon Formations), was studied here in detail from the outcrops of the *Chaînons Béarnais*. The main features of their diagenetic history, especially the conditions of dolomitization, may be summarized as follows:

1. Massive limestone dolomitization, which comprises the main volume of dolomite in the area, was generated in near-surface to shallow burial conditions in both carbonate reservoirs. This was primarily controlled by the carbonate facies, and thus, by the depositional environments and vertical stacking.
2. This dolomitization occurred coevally in the Mano and Meillon Formations at about ~135 Ma, beginning with the seepage of marine-derived water that interacted with clay and/or groundwater in normal thermal conditions, thus allowing for the regional uplift and the early reactive salt diapirism.
3. The influx of hot basinal brines by thermal convection interacted with underlying Triassic evaporites and remobilized early dolomites, resulting in a massive dolomite recrystallization of the Meillon Formation at around ~106 Ma. This dolomitization was triggered by crustal thinning and the associated thermal anomaly generated during the Early Cretaceous rifting. It was probably enhanced by the rise of salt diapir. This dolomitization highlighted the compartmentalization of the two reservoirs.
4. Two additional dolomite cementation stages are recorded in the residual porosity and tectonic veins of the still compartmentalized formations. Precipitation occurred at

temperatures above $\sim 150^{\circ}\text{C}$ during the Albian. Whereas the cements in the Meillon Formation still record the contribution from dissolved Triassic evaporites, in the Mano Formation, they precipitated from low salinity water, probably resulting from clay dehydration. In this case, Mg was probably supplied mostly by the earlier massive dolomites.

5. At the same time during the Albian, a last saddle dolomite cement precipitated in the vicinity of faults associated with breccias. It formed from the same highly saline, hot ($T > 250^{\circ}\text{C}$), crustal-derived waters possibly mixed with mantle-derived fluids in both formations. The connection between the reservoirs was then restored as a result of the faulting and active diapirism related to Early Cretaceous rifting. In the Mano Formation, these basinal brines locally seeped into sedimentary breccias, generating the stratabound replacement of the dolomite.

6. Subsequent quartz and calcite cements, formed at a lower temperature ($T < 200^{\circ}\text{C}$), record the restauration of the reservoir compartmentalization in a post-rift to inversion context.

This case study represents a comprehensive and data-rich example of the multi-phase dolomitization of a carbonate platform in a complex geodynamic setting evolving from pre-rift to hyperextension and then collision. This provides evidence of the major control exerted by rifting, combined with the presence of diapiric salt, on dolomitization. Likewise, ancient carbonate platforms on modern salt-rich passive margins may have been massively dolomitized, thus forming potential targets for exploration.

Acknowledgments

Geoffrey Motte benefited from a PhD grant funded by Total EP-R&D as part of the Fluids geological research project. Laurent Guy is kindly thanked for his support and introduction to the field. Laurent Lambert and his colleagues from BGM *Centre Scientifique et Technique Jean Féger TOTAL* are thanked for providing access to their facilities. Guillaume

1266 Barré and Stephen Centrella are warmly thanked for their fruitful discussions. The authors
1267 also acknowledge the suggestions and comments of the associate editor Marco Brandano
1268 and the reviewers Juan Diego Martín Martín and Mar Moragas, which greatly improved the
1269 quality of the manuscript.

References

- Adam, J.E., Rhodes, M.L., 1960. Dolomitization By Seepage Refluxion. Am. Assoc. Pet. Geol. Bull. 44, 1912–1920. <https://doi.org/10.1306/bc74368d-16be-11d7-8645000102c1865d>
- Adams, A., Diamond, L.W., Aschwanden, L., 2019. Dolomitization by hypersaline reflux into dense groundwaters as revealed by vertical trends in strontium and oxygen isotopes: Upper Muschelkalk, Switzerland. Sedimentology 66, 362–390. <https://doi.org/10.1111/sed.12530>
- Al-Aasm, I.S., Mrad, C., Packard, J., 2019. Fluid compartmentalization of Devonian and Mississippian dolostones, Western Canada Sedimentary Basin: Petrologic and geochemical evidence from fracture mineralization. Can. J. Earth Sci. 56, 265–305. <https://doi.org/10.1139/cjes-2018-0226>
- Albarède, F., Michard-Vitrac, A., 1978. Datation du métamorphisme des terrains secondaires des Pyrénées par la méthodes ^{39}Ar - ^{40}Ar et ^{87}Rb - ^{87}Sr . Ses relations avec les péridotites associées. Bull. Société Géologique Fr. 20, 681–687.
- Azambre, B., Rossy, M., 1976. Le magmatisme alcalin d'âge crétacé dans les Pyrénées occidentales et l'Arc basque ; ses relations avec le métamorphisme et la tectonique. Bull. Société Géologique Fr. 18, 1725–1728.
- Azambre, B., Rossy, M., Albarède, F., 1992. Petrology of the Alkaline Magmatism from the Cretaceous North-Pyrenean Rift-Zone (France and Spain). Eur. J. Mineral. 4, 813–834.
- Banner, J.L., 1995. Application of the trace element and isotope geochemistry of strontium to studies of carbonate diagenesis. Sedimentology 42, 805–824.
- Barale, L., Bertok, C., Talabani, N.S., D'Atri, A., Martire, L., Piana, F., Prétat, A., 2016. Very hot, very shallow hydrothermal dolomitization: An example from the Maritime Alps (North-West Italy – South-East France). Sedimentology 63, 2037–2065. <https://doi.org/10.1111/sed.12294>
- Barbier, M., Floquet, M., Hamon, Y., Callot, J.-P., 2015. Nature and distribution of diagenetic

1297 phases and petrophysical properties of carbonates: The Mississippian Madison
 1298 Formation (Bighorn Basin, Wyoming, USA). *Mar. Pet. Geol.* 67, 230–248.
 1299 <https://doi.org/10.1016/j.marpetgeo.2015.05.026>

1300 Barbier, M., Hamon, Y., Callot, J.-P., Floquet, M., Daniel, J.-M., 2012. Sedimentary and
 1301 diagenetic controls on the multiscale fracturing pattern of a carbonate reservoir: The
 1302 Madison Formation (Sheep Mountain, Wyoming, USA). *Mar. Pet. Geol.* 29, 50–67.
 1303 <https://doi.org/10.1016/j.marpetgeo.2011.08.009>

1304 Barbier, M., Hamon, Y., Doligez, B., Callot, J.-P., Floquet, M., Daniel, J.-M., 2011. Simulation
 1305 stochastique couplée faciès et diagenèse. L'exemple de la diagenèse précoce dans la
 1306 Formation Madison (Wyoming, USA). *Oil Gas Sci. Technol.* 67, 123–145.
 1307 <https://doi.org/10.2516/ogst/2011009>

1308 Bathurst, R.G.C., 1971. Carbonate sediments and their diagenesis, *Developments in*
 1309 *Sedimentology* 12.

1310 Beaudoin, N., Bellahsen, N., Lacombe, O., Emmanuel, L., Pironon, J., 2014. Crustal-scale
 1311 fluid flow during the tectonic evolution of the Bighorn Basin (Wyoming, USA). *Basin Res.*
 1312 26, 403–435. <https://doi.org/10.1111/bre.12032>

1313 Beckert, J., Vandeginste, V., John, C.M., 2015. Exploring the geological features and
 1314 processes that control the shape and internal fabrics of late diagenetic dolomite bodies
 1315 (Lower Khuff equivalent - Central Oman Mountains). *Mar. Pet. Geol.* 68, 325–340.
 1316 <https://doi.org/10.1016/j.marpetgeo.2015.08.038>

1317 Biehl, B.C., Reuning, L., Schoenherr, J., Lüders, V., Kukla, P.A., 2016. Impacts of
 1318 hydrothermal dolomitization and thermochemical sulfate reduction on secondary
 1319 porosity creation in deeply buried carbonates: A case study from the Lower Saxony
 1320 Basin, northwest Germany. *Am. Assoc. Pet. Geol. Bull.* 100, 597–621.
 1321 <https://doi.org/10.1306/01141615055>

1322 Biteau, J.-J., Le Marrec, A., Le Vot, M., Masset, J.-M., 2006. The Aquitaine Basin. *Pet.*
 1323 *Geosci.* 12, 247–273. <https://doi.org/10.1144/1354-079305-674>

1324 Braithwaite, C.J.R., Rizzi, G., Darke, G., 2004. The geometry and petrogenesis of dolomite

1325 hydrocarbon reservoirs: introduction. *Geom. Petrog. Dolomite Hydrocarb. Reserv. Geol.*
1326 *Soc. London Spec. Publ.* 235, 1–6. <https://doi.org/10.1144/GSL.SP.2004.235.01.01>

1327 Brauer, J.S., Baker, P.A., 1984. Experimental hydrothermal dedolomitization. *Am. Assoc.*
1328 *Pet. Geol. Bull.* 68, 456–457.

1329 Breesch, L., Swennen, R., Vincent, B., Ellison, R., Dewever, B., 2010. Dolomite cementation
1330 and recrystallisation of sedimentary breccias along the Musandam Platform margin
1331 (United Arab Emirates). *J. Geochemical Explor.* 106, 34–43.
1332 <https://doi.org/10.1016/j.gexplo.2010.02.005>

1333 Brinkmann, R., Lögters, H., 1968. Diapirs in western Pyrenees and foreland, Spain.
1334 *Diapirism Diapirs, AAPG Spec. Vol.* 275–292.

1335 Burke, E.A.J., 2001. Raman microspectrometry of fluid inclusions. *Lithos* 55, 139–158.
1336 [https://doi.org/10.1016/S0024-4937\(00\)00043-8](https://doi.org/10.1016/S0024-4937(00)00043-8)

1337 Bustillo, M.A., 2010. Chapter 3 Silicification of Continental Carbonates, in: *Developments in*
1338 *Sedimentology*. Elsevier, pp. 153–178. [https://doi.org/10.1016/S0070-4571\(09\)06203-7](https://doi.org/10.1016/S0070-4571(09)06203-7)

1339 Butler, G.P., Harris, P.M., St. C. Kendall, C.G., 1982. Recent evaporites from the Abu Dhabi
1340 coastal flats. *Depos. diagenetic spectra evaporites SEPM core Work.* 3, Calgary, June
1341 1982 33–64. <https://doi.org/10.2110/cor.82.01.0033>

1342 Callot, J.-P., Breesch, L., Guilhaumou, N., Roure, F., Swennen, R., Vilasi, N., 2010. Paleo-
1343 fluids characterisation and fluid flow modelling along a regional transect in Northern
1344 United Arab Emirates (UAE). *Arab. J. Geosci.* 3, 413–437.
1345 <https://doi.org/10.1007/s12517-010-0233-z>

1346 Canérot, J., Hudec, M.R., Rockenbauch, K., 2005. Mesozoic diapirism in the Pyrenean
1347 orogen: Salt tectonics on a transform plate boundary. *Am. Assoc. Pet. Geol. Bull.* 89,
1348 211–229. <https://doi.org/10.1306/09170404007>

1349 Canérot, J., Lenoble, J.-L., 1993. Diapirisme crétacé sur la marge ibérique des Pyrénées
1350 occidentales : exemple du pic de Lauriolle ; comparaison avec l'Aquitaine, les Pyrénées
1351 centrales et orientales. *Bull. Société Géologique Fr.* 164, 719–726.

1352 Canérot, J., Lenoble, J.-L.J.-L., Marchand, D., Thierry, J., 1990. Nouveau schéma de

1353 corrélations stratigraphiques du Dogger-Malm dans les Pyrénées occidentales
 1354 françaises. *Comptes rendus l'Académie des Sci.* 311, 1337–1343.

1355 Canérot, J., Majesté-Menjoulas, C., Ternet, Y., 1999. Le cadre stratigraphique et
 1356 géodynamique des altérites et des bauxites sur la marge ibérique des Pyrénées
 1357 occidentales (France). *C. R. Acad. Sc. Paris* 328, 451–456.

1358 Cantrell, D., Swart, P.K., Hagerty, R., 2004. Genesis and characterization of dolomite, Arab-
 1359 D Reservoir, Ghawar field, Saudi Arabia. *GeoArabia* 9, 11–36.

1360 Carmichael, S.K., Ferry, J.M., McDonough, W.F., 2008. Formation of replacement dolomite
 1361 in the Latemar carbonate buildup, dolomites, Northern Italy: Part 1. Field relations,
 1362 mineralogy, and geochemistry. *Am. J. Sci.* 308, 851–884.
 1363 <https://doi.org/10.2475/07.2008.03>

1364 Castéras, M., Canérot, J., Paris, J., Tisin, D., Azambre, M., Alimen, H., 1970. Carte
 1365 géologique de la France au 1/50 000: Feuille d'Oloron Sainte Marie. BRGM Orléans, Fr.

1366 Caumon, M.-C., Dubessy, J., Robert, P., Tarantola, A., 2013. Fused-silica capillary capsules
 1367 (FSCCs) as reference synthetic aqueous fluid inclusions to determine chlorinity by
 1368 Raman spectroscopy. *Eur. J. Mineral.* 25, 755–763. [https://doi.org/10.1127/0935-](https://doi.org/10.1127/0935-1221/2013/0025-2280)
 1369 [1221/2013/0025-2280](https://doi.org/10.1127/0935-1221/2013/0025-2280)

1370 Caumon, M.-C., Tarantola, A., Mosser-Ruck, R., 2015. Raman spectra of water in fluid
 1371 inclusions: I. Effect of host mineral birefringence on salinity measurement. *J. Raman*
 1372 *Spectrosc.* 46, 969–976. <https://doi.org/10.1002/jrs.4708>

1373 Chaudhuri, S., Clauer, N., 1992. Signatures of radiogenic isotopes in deep subsurface
 1374 waters in continents. *Isot. Signatures Sediment. Rec.* 43, 497–529.

1375 Chen, Y.X., Schertl, H.P., Zheng, Y.F., Huang, F., Zhou, K., Gong, Y.Z., 2016. Mg–O
 1376 isotopes trace the origin of Mg-rich fluids in the deeply subducted continental crust of
 1377 Western Alps. *Earth Planet. Sci. Lett.* 456, 157–167.
 1378 <https://doi.org/10.1016/j.epsl.2016.09.010>

1379 Choquette, P.W., Hiatt, E.E., 2008. Shallow-burial dolomite cement: a major component of
 1380 many ancient sucrosic dolomites. *Sedimentology* 55, 423–460.

1381 <https://doi.org/10.1111/j.1365-3091.2007.00908.x>

1382 Choukroune, P., 1992. Tectonic evolution of the Pyrenees. *Annu. Rev. Earth Planet. Sci.* 20,
1383 143–158.

1384 Choukroune, P., 1976. Structure et évolution tectonique de la zone nord-Pyrénéenne :
1385 Analyse de la déformation dans une portion de chaîne à schistosité sub-verticale.
1386 Mémoires la société géologique Fr. 127, 1–116.

1387 Choukroune, P., Le Pichon, X., Seguret, M., Sibuet, J., 1973. Bay of Biscay and Pyrenees.
1388 *Earth Planet. Sci. Lett.* 18, 109–118.

1389 Choukroune, P., Roure, F., Pinet, B., 1990. Main results of the ECORS Pyrenees profile.
1390 *Tectonophysics* 173. [https://doi.org/10.1016/0040-1951\(90\)90234-Y](https://doi.org/10.1016/0040-1951(90)90234-Y)

1391 Clerc, C., Lagabrielle, Y., 2014. Thermal control on the modes of crustal thinning leading to
1392 mantle exhumation: Insights from the cretaceous pyrenean hot paleomargins. *Tectonics*
1393 33, 1340–1359. <https://doi.org/10.1002/2013TC003471>

1394 Clerc, C., Lagabrielle, Y., Labaume, P., Ringenbach, J.C., Vauchez, A., Nalpas, T.,
1395 Bousquet, R., Ballard, J.F., Lahfid, A., Fourcade, S., 2016. Basement - Cover
1396 decoupling and progressive exhumation of metamorphic sediments at hot rifted margin.
1397 Insights from the Northeastern Pyrenean analog. *Tectonophysics* 686, 82–97.
1398 <https://doi.org/10.1016/j.tecto.2016.07.022>

1399 Clerc, C., Lahfid, A., Monié, P., Lagabrielle, Y., Chopin, C., Poujol, M., Boulvais, P.,
1400 Ringenbach, J.C., Masini, E., de Saint Blanquat, M., 2015. High-temperature
1401 metamorphism during extreme thinning of the continental crust: A reappraisal of the
1402 North Pyrenean passive paleomargin. *Solid Earth* 6, 643–668.
1403 <https://doi.org/10.5194/se-6-643-2015>

1404 Combes, P.-J., Peybernès, B., Leyreloup, A.F., 1998. Altérites et bauxites, témoins des
1405 marges européenne et ibérique des Pyrénées occidentales au Jurassique supérieur -
1406 Crétacé inférieur, à l'ouest de la vallée d'Ossau (Pyrénées-Atlantiques, France). *C. R.*
1407 *Acad. Sc. Paris* 327, 271–278.

1408 Corre, B., 2017. La bordure nord de la plaque ibérique à l'Albo-Cénomanién. *Architecture*

1409 d'une marge passive de type ductile (Chaînons Béarnais, Pyrénées Occidentales).
 1410 Université de Rennes 1.

1411 Corre, B., Boulvais, P., Boiron, M.-C., Lagabriele, Y., Marasi, L., Clerc, C., 2018. Fluid
 1412 circulations in response to mantle exhumation at the passive margin setting in the north
 1413 Pyrenean zone , France. *Mineral. Petrol.* 0, 0. <https://doi.org/10.1007/s00710-018-0559->
 1414 x

1415 Corre, B., Lagabriele, Y., Labaume, P., Fourcade, S., Clerc, C., Balle, M., 2016. Deformation
 1416 associated with mantle exhumation in a distal, hot passive margin environment : New
 1417 constraints from the Sarailé Massif (Chaînons Béarnais, North-Pyrenean Zone).
 1418 *Comptes rendus - Geosci.* 348, 279–289. <https://doi.org/10.1016/j.crte.2015.11.007>

1419 Cox, K.G., 1989. The role of mantle plumes in the development of continental drainage
 1420 patterns. *Nature* 342, 873–877. <https://doi.org/10.1038/342873a0>

1421 Croizé, D., Renard, F., Gratier, J.P., 2013. Compaction and Porosity Reduction in
 1422 Carbonates: A Review of Observations, Theory, and Experiments, in: *Advances in*
 1423 *Geophysics.* pp. 181–238. <https://doi.org/10.1016/B978-0-12-380940-7.00003-2>

1424 Davies, G.R., Smith Jr, L.B., 2006. Structurally controlled hydrothermal dolomite reservoir
 1425 facies: An overview. *Am. Assoc. Pet. Geol. Bull.* 90, 1641–1690.
 1426 <https://doi.org/10.1306/05220605164>

1427 Debure, M., Lassin, A., Marty, N.C., Claret, F., Virgone, A., Calassou, S., Gaucher, E.C.,
 1428 2019. Thermodynamic evidence of giant salt deposit formation by serpentinization: an
 1429 alternative mechanism to solar evaporation. *Sci. Rep.* 9. <https://doi.org/10.1038/s41598->
 1430 019-48138-9

1431 Deffeyes, K.S., Lucia, J.F., Weyl, P.K., 1965. Dolomitization of Recent and Plio-Pleistocene
 1432 Sediments By Marine Evaporite Waters on Bonaire, Netherlands Antilles. *Soc. Econ.*
 1433 *Paleontol. Mineral. Spec. Publ.* 13, 71–88. <https://doi.org/10.2110/pec.65.07.0071>

1434 Di Cuia, R., Riva, A., Scifoni, A., Moretti, A., Spötl, C., Caline, B., 2011. Dolomite
 1435 characteristics and diagenetic model of the Calcarei Grigi Group (Asiago Plateau,
 1436 Southern Alps - Italy): An example of multiphase dolomitization. *Sedimentology* 58,

1437 1347–1369. <https://doi.org/10.1111/j.1365-3091.2010.01212.x>

1438 Douville, E., Bienvenu, P., Charlou, J.L., Donval, J.P., Fouquet, Y., Appriou, P., Gamo, T.,
 1439 1999. Yttrium and rare earth elements in fluids from various deep-sea hydrothermal
 1440 systems. *Geochim. Cosmochim. Acta* 63, 627–643.

1441 Douville, E., Charlou, J.L., Oelkers, E.H., Bienvenu, P., Jove Colon, C.F., Donval, J.P.,
 1442 Fouquet, Y., Prieur, D., Appriou, P., 2002. The rainbow vent fluids (36° 14'N, MAR): the
 1443 influence of ultramafic rocks and phase separation on trace metal content in Mid-Atlantic
 1444 Ridge hydrothermal fluids. *Chem. Geol.* 184, 37–48.

1445 Drost, K., Chew, D., Petrus, J.A., Scholze, F., Woodhead, J.D., Schneider, J.W., Harper,
 1446 D.A.T., 2018. An Image Mapping Approach to U-Pb LA-ICP-MS Carbonate Dating and
 1447 Applications to Direct Dating of Carbonate Sedimentation. *Geochemistry, Geophys.*
 1448 *Geosystems* 19, 4631–4648. <https://doi.org/https://doi.org/10.1029/2018GC007850>

1449 Dubessy, J., Lhomme, T., Boiron, M.-C., Rull, F., 2002. Determination of chlorinity in
 1450 aqueous fluids using Raman spectroscopy of the stretching band of water at room
 1451 temperature: Application to fluid inclusions. *Appl. Spectrosc.* 56, 99–106.
 1452 <https://doi.org/10.1366/0003702021954278>

1453 Ducoux, M., Jolivet, L., Callot, J.-P., Aubourg, C., Masini, E., Lahfid, A., Homonnay, E.,
 1454 Cagnard, F., Gumiaux, C., Baudin, T., 2019. The Nappe des Marbres Unit of the
 1455 Basque-Cantabrian Basin: The Tectono-thermal Evolution of a Fossil Hyperextended
 1456 Rift Basin. *Tectonics* 38, 3881–3915. <https://doi.org/10.1029/2018TC005348>

1457 Duggan, J.P., Mountjoy, E.W., Stasiuk, L.D., 2001. Fault-controlled dolomitization at Swan
 1458 Hills Simonette oil field (Devonian), deep basin west-central Alberta, Canada.
 1459 *Sedimentology* 48, 301–323.

1460 Dunham, R.J., 1962. Classification of Carbonate Rocks According to Depositional Textures,
 1461 in: *Classification of Carbonate Rocks--A Symposium*. pp. 108–121.

1462 Elias Bahnan, A., 2019. Circulation des fluides et diagenèse du système pétrolier de Lacq :
 1463 Impact de l'évolution géodynamique. Université de Lorraine.

1464 Elias Bahnan, A., Carpentier, C., Pironon, J., Ford, M., Ducoux, M., Barré, G., Mangelot, X.,

1465 Gaucher, E.C., 2020. Impact of geodynamics on fluid circulation and diagenesis of
 1466 carbonate reservoirs in a foreland basin: Example of the Upper Lacq reservoir
 1467 (Aquitaine basin, SW France). *Mar. Pet. Geol.* 111, 676–694.
 1468 <https://doi.org/10.1016/j.marpetgeo.2019.08.047>
 1469 Embry, A.F., Klován, E.J., 1971. The Upper Devonian stratigraphy of northeastern Banlts
 1470 Island has. *Bull. Can. Pet. Geol.* 19, 730–781.
 1471 Fauré, P., 2002. Le Lias des Pyrénées tome 2 Partie 2.
 1472 Fischer, M.P., Kenroy, P.R., Smith, A.P., 2013. Fluid Systems around Salt Diapirs *. *Search*
 1473 *Discov. Artic.*
 1474 Frezzotti, M.L., Tecce, F., Casagli, A., 2012. Raman spectroscopy for fluid inclusion analysis.
 1475 *J. Geochemical Explor.* 112, 1–20. <https://doi.org/10.1016/j.gexplo.2011.09.009>
 1476 Friedman, I., O’Neil, J.R., 1977. Data of Geochemistry Sixth Edition. *Geol. Surv. Prof. Pap.*
 1477 440-KK, 1–117.
 1478 Gao, G., Land, L.S., Elmore, R.D., 1995. Multiple episodes of dolomitization in the Arbuckle
 1479 Group, Arbuckle Mountains, South-Central Oklahoma: field, petrographic and,
 1480 geochemical evidence. *J. Sediment. Petrol.* A65, 321–331.
 1481 Garaguly, I., Varga, A., Raucsik, B., Schubert, F., Czuppon, G., Frei, R., 2018. Pervasive
 1482 early diagenetic dolomitization , subsequent hydrothermal alteration , and late stage
 1483 hydrocarbon accumulation in a Middle Triassic carbonate sequence (Szeged Basin ,
 1484 SE Hungary). *Mar. Pet. Geol.* 98, 270–290.
 1485 <https://doi.org/10.1016/j.marpetgeo.2018.07.024>
 1486 Gisquet, F., Lamarche, J., Floquet, M., Borgomano, J., Masse, J.-P.P., Caline, B., 2013.
 1487 Three-dimensional structural model of composite dolomite bodies in folded area (upper
 1488 jurassic of the Etoile massif, southeastern France). *Am. Assoc. Pet. Geol. Bull.* 97,
 1489 1477–1501. <https://doi.org/10.1306/04021312016>
 1490 Golberg, J.M., Leyreloup, A.F., 1990. High temperature-low pressure Cretaceous
 1491 metamorphism related to crustal thinning (Eastern North Pyrenean Zone, France).
 1492 *Contrib. to Mineral. Petrol.* 104, 194–207. <https://doi.org/10.1007/BF00306443>

1493 Goldhammer, R.K., 1997. Compaction and decompaction algorithms for sedimentary
1494 carbonates. *J. Sediment. Res.* 67, 26–35.

1495 Goldstein, R.H., Reynolds, T.J., 1994. Systematics of fluid inclusions in diagenetic minerals,
1496 Society for Sedimentary Geology. <https://doi.org/10.2110/scn.94.31>

1497 Gong, Z., Langereis, C.G., Mullender, T.A.T., 2008. The rotation of Iberia during the Aptian
1498 and the opening of the Bay of Biscay. *Earth Planet. Sci. Lett.* 273, 80–93.
1499 <https://doi.org/10.1016/j.epsl.2008.06.016>

1500 Gonzalez, E., Ferket, H., Callot, J.-P., Guilhaumou, N., Ortuno, S., Roure, F., 2012.
1501 Paleoburial, hydrocarbon generation, and migration in the Córdoba Platform and
1502 Veracruz Basin: Insights from fluid inclusion studies and two-dimensional (2D) basin
1503 modeling. *Soc. Econ. Paleontol. Mineral. Spec. Publ.* 103, 167–186.
1504 <https://doi.org/10.2110/sepmsp.103.167>

1505 Gregg, J.M., Sibley, D.F., 1987. Classification of Dolomite Rock Texture. *J. Sediment. Petrol.*
1506 57, 967–975.

1507 Grimaldi, M.-H., 1988. La dolomie tidale du Jurassique terminal des Pyrénées occidentales
1508 Sédimentologie, Diagenèse polyphasée et contexte dynamique, Tome 1.

1509 Grunnaleite, I., Mosbron, A., 2019. On the significance of salt modelling-example from
1510 modelling of salt tectonics, temperature and maturity around salt structures in Southern
1511 North Sea. *Geosci.* 9. <https://doi.org/10.3390/geosciences9090363>

1512 Guo, C., Chen, D., Qing, H., Dong, S., Li, G., Wang, D., Qian, Y., Liu, C., 2016. Multiple
1513 dolomitization and later hydrothermal alteration on the Upper Cambrian-Lower
1514 Ordovician carbonates in the northern Tarim Basin, China. *Mar. Pet. Geol.* 72, 295–316.
1515 <https://doi.org/10.1016/j.marpetgeo.2016.01.023>

1516 Haeri-Ardakani, O., Al-Aasm, I.S., Coniglio, M., 2013a. Petrologic and geochemical attributes
1517 of fracture-related dolomitization in Ordovician carbonates and their spatial distribution
1518 in southwestern Ontario, Canada. *Mar. Pet. Geol.* 43, 409–422.
1519 <https://doi.org/10.1016/j.marpetgeo.2012.12.006>

1520 Haeri-Ardakani, O., Al-Aasm, I.S., Coniglio, M., 2013b. Fracture mineralization and fluid flow

1521 evolution: An example from Ordovician-Devonian carbonates, southwestern Ontario,
 1522 Canada. *Geofluids* 13, 1–20. <https://doi.org/10.1111/gfl.12003>

1523 Hallam, A., 2001. A review of the broad pattern of Jurassic sea-level changes and their
 1524 possible causes in the light of current knowledge. *Palaeogeogr. Palaeoclimatol.*
 1525 *Palaeoecol.* 167, 23–37. [https://doi.org/https://doi.org/10.1016/S0031-0182\(00\)00229-7](https://doi.org/https://doi.org/10.1016/S0031-0182(00)00229-7)

1526 Haq, B.U., Hardenbol, J., Vail, P.R., 1987. Chronology of Fluctuating Sea Levels Since the
 1527 Triassic. *Science* (80-.). 235, 1156–1167.

1528 Hardie, L.A., 1987. Perspectives. Dolomitization: a critical view of some current views. *J.*
 1529 *Sediment. Petrol.* 57, 166–183. [https://doi.org/10.1306/212f8ad5-2b24-11d7-](https://doi.org/10.1306/212f8ad5-2b24-11d7-8648000102c1865d)
 1530 [8648000102c1865d](https://doi.org/10.1306/212f8ad5-2b24-11d7-8648000102c1865d)

1531 Hart, N.R., Stockli, D.F., Lavier, L.L., Hayman, N.W., 2017. Thermal evolution of a
 1532 hyperextended rift basin, Mauléon Basin, western Pyrenees. *Tectonics* 36, 1103–1128.
 1533 <https://doi.org/10.1002/2016TC004365>

1534 Hendry, J.P., Gregg, J.M., Shelton, K.L., Somerville, I.D., Crowley, S.F., 2015. Origin,
 1535 characteristics and distribution of fault-related and fracture-related dolomitization:
 1536 Insights from Mississippian carbonates, Isle of Man. *Sedimentology* 62, 717–752.
 1537 <https://doi.org/10.1111/sed.12160>

1538 Hesse, R., 1987. Selective and reversible carbonate—silica replacements in Lower
 1539 Cretaceous carbonate-bearing turbidites of the Eastern Alps. *Sedimentology* 34, 1055–
 1540 1077. <https://doi.org/10.1111/j.1365-3091.1987.tb00592.x>

1541 Heydari, E., 1997. Hydrotectonic models of burial diagenesis in platform carbonates based
 1542 on formation water geochemistry in north american sedimentary basins. *Soc. Sediment.*
 1543 *Geol.* 57, 53–79.

1544 Hill, C.A., Polyak, V.J., Asmerom, Y., P. Provencio, P., 2016. Constraints on a Late
 1545 Cretaceous uplift, denudation, and incision of the Grand Canyon region, southwestern
 1546 Colorado Plateau, USA, from U-Pb dating of lacustrine limestone. *Tectonics* 35, 896–
 1547 906. <https://doi.org/10.1002/2016TC004166>

1548 Hoareau, G., Claverie, F., Pecheyran, C., Paroissin, C., Motte, G., Chailan, O., Girard, J.,

1549 n.d. Direct U-Pb dating of carbonates from micron scale fsLA-ICPMS images using
 1550 robust regression. *Geochronology* in press. <https://doi.org/10.5194/gchron-2020-10>
 1551 Horita, J., 2014. Oxygen and carbon isotope fractionation in the system dolomite – water –
 1552 CO₂ to elevated temperatures. *Geochim. Cosmochim. Acta* 129, 111–124.
 1553 <https://doi.org/10.1016/j.gca.2013.12.027>
 1554 Illing, L.V., 1964. Penecontemporary Dolomite in the Persian Gulf. *Am. Assoc. Pet. Geol.*
 1555 *Bull.* 48, 532–533.
 1556 Illing, L.V., 1959. Deposition and diagenesis of some Upper Palaeozoic carbonate sediments
 1557 in Western Canada. *World Pet. Congr.* January.
 1558 Incerpi, N., Manatschal, G., Martire, L., Gerdes, A., Bertok, C., 2020. Characteristics and
 1559 timing of hydrothermal fluid circulation in the fossil Pyrenean hyperextended rift system:
 1560 new constraints from the Chaînons Béarnais (W Pyrenees). *Int. J. Earth Sci.*
 1561 <https://doi.org/10.1007/s00531-020-01852-6>
 1562 Iriarte, E., Lopez-Horgue, M.A., Schroeder, S., Caline, B., 2012. Interplay between fracturing
 1563 and hydrothermal fluid flow in the Ason Valley hydrothermal dolomites (Basque –
 1564 Cantabrian Basin, Spain). *Geol. Soc. London Spec. Publ.* 370, 207–227.
 1565 <https://doi.org/http://dx.doi.org/10.1144/SP370.10>
 1566 Izquierdo-Llavall, E., Menant, A., Aubourg, C., Callot, J.-P.J.-P., Hoareau, G., Lahfid, A.,
 1567 Camps, P., Pere, E., 2020. Pre-orogenic folds and syn-orogenic basement tilts in an
 1568 inverted hyperextended margin : the northern Pyrenees case study. *Tectonics* 39.
 1569 Jackson, M.P.A., Hudec, M.R., 2017. *Salt Tectonics*.
 1570 James, N.P., Choquette, P.W., 1984. Diagenesis 9 -. Limestones - The meteoric diagenetic
 1571 environment. *Geosci. Canada* 11, 161–194.
 1572 James, V., 1998. La plate-forme carbonatée ouest-pyrénéenne au Jurassique moyen et
 1573 supérieur : Stratigraphie séquentielle, stades d'évolution, relations avec la subsurface
 1574 en Aquitaine méridionale.
 1575 James, V., Canérot, J., 1999. Diapirisme et structuration post-triasique des Pyrénées
 1576 occidentales et de l'Aquitaine méridionale (France). *Eclogae Geol. Helv* 92, 63–72.

1577 Jammes, S., Lavier, L.L., Manatschal, G., 2010a. Extreme crustal thinning in the Bay of
 1578 Biscay and the Western Pyrenees: From observations to modeling. *Geochemistry,*
 1579 *Geophys. Geosystems* 11. <https://doi.org/10.1029/2010GC003218>
 1580 Jammes, S., Manatschal, G., Lavier, L.L., Masini, E., 2009. Tectonosedimentary evolution
 1581 related to extreme crustal thinning ahead of a propagating ocean: Example of the
 1582 western Pyrenees. *Tectonics* 28, 1–24. <https://doi.org/10.1029/2008TC002406>
 1583 Jammes, S., Tiberi, C., Manatschal, G., 2010b. 3D architecture of a complex transcurrent rift
 1584 system: The example of the Bay of Biscay-Western Pyrenees. *Tectonophysics* 489,
 1585 210–226. <https://doi.org/10.1016/j.tecto.2010.04.023>
 1586 Jensen, P.K., 1983. Calculations on the thermal conditions around a salt diapir. *Geophys.*
 1587 *Prospect.* 31, 481–489. <https://doi.org/10.1111/j.1365-2478.1983.tb01064.x>
 1588 Jochum, K.P., Weis, U., Stoll, B., Kuzmin, D., Yang, Q., Raczek, I., Jacob, D.E., Stracke, A.,
 1589 Birbaum, K., Frick, D.A., Günther, D., Enzweiler, J., 2011. Determination of reference
 1590 values for NIST SRM 610-617 glasses following ISO guidelines. *Geostand.*
 1591 *Geoanalytical Res.* 35, 397–429. <https://doi.org/10.1111/j.1751-908X.2011.00120.x>
 1592 Jochum, K.P., Wilson, S.A., Abouchami, W., Amini, M., Chmeleff, J., Eisenhauer, A., Hegner,
 1593 E., Iaccheri, L.M., Kieffer, B., Krause, J., McDonough, W.F., Mertz-Kraus, R., Raczek, I.,
 1594 Rudnick, R.L., Scholz, D., Steinhöfel, G., Stoll, B., Stracke, A., Tonarini, S., Weis, D.,
 1595 Weis, U., Woodhead, J.D., 2010. GSD-1G and MPI-DING Reference Glasses for In Situ
 1596 and Bulk Isotopic Determination. *Geostand. Geoanalytical Res.* 35, 193–226.
 1597 <https://doi.org/10.1111/j.1751-908X.2010.00114.x>
 1598 Jonas, L., Müller, T., Dohmen, R., Baumgartner, L.P., Putlitz, B., 2015. Transport-controlled
 1599 hydrothermal replacement of calcite by Mg-carbonates. *Geology* 43, 779–783.
 1600 <https://doi.org/10.1130/G36934.1>
 1601 Jourdon, A., Mouthereau, F., Le Pourhiet, L., Callot, J.-P., 2020. Topographic and Tectonic
 1602 Evolution of Mountain Belts Controlled by Salt Thickness and Rift Architecture.
 1603 *Tectonics* 39. <https://doi.org/10.1029/2019TC005903>
 1604 Kaczmarek, S.E., Sibley, D.F., 2011. On the evolution of dolomite stoichiometry and cation

1605 order during high-temperature synthesis experiments: An alternative model for the
 1606 geochemical evolution of natural dolomites. *Sediment. Geol.* 240, 30–40.
 1607 <https://doi.org/10.1016/j.sedgeo.2011.07.003>

1608 Kaiser, B.O., Cacace, M., Scheck-Wenderoth, M., Lewerenz, B., 2011. Characterization of
 1609 main heat transport processes in the Northeast German Basin: Constraints from 3-D
 1610 numerical models. *Geochemistry, Geophys. Geosystems* 12, 1–17.
 1611 <https://doi.org/10.1029/2011GC003535>

1612 Kim, S.T., Mucci, A., Taylor, B.E., 2007. Phosphoric acid fractionation factors for calcite and
 1613 aragonite between 25 and 75 °C: Revisited. *Chem. Geol.* 246, 135–146.
 1614 <https://doi.org/10.1016/j.chemgeo.2007.08.005>

1615 Koeshidayatullah, A., Corlett, H., Stacey, J., Swart, P.K., Boyce, A., Robertson, H., Whitaker,
 1616 F., Hollis, C., 2020. Evaluating new fault-controlled hydrothermal dolomitization models:
 1617 Insights from the Cambrian Dolomite, Western Canadian Sedimentary Basin.
 1618 *Sedimentology*. <https://doi.org/10.1111/sed.12729>

1619 Krupp, R.E., 2005. Formation and chemical evolution of magnesium chloride brines by
 1620 evaporite dissolution processes - Implications for evaporite geochemistry. *Geochim.*
 1621 *Cosmochim. Acta* 69, 4283–4299. <https://doi.org/10.1016/j.gca.2004.11.018>

1622 Labaume, P., Teixell, A., 2020. Evolution of salt structures of the Pyrenean rift (Chaînons
 1623 Béarnais, France): From hyper-extension to tectonic inversion. *Tectonophysics* 785.
 1624 <https://doi.org/10.1016/j.tecto.2020.228451>

1625 Lagabrielle, Y., Bodinier, J.-L., 2008. Submarine reworking of exhumed subcontinental
 1626 mantle rocks: field evidence from the Lherz peridotites, French Pyrenees. *Terra Nov.*
 1627 20, 11–21. <https://doi.org/10.1111/j.1365-3121.2007.00781.x>

1628 Lagabrielle, Y., Clerc, C., Vauchez, A., Lahfid, A., Labaume, P., Azambre, B., Fourcade, S.,
 1629 Dautria, J., 2016. Very high geothermal gradient during mantle exhumation recorded in
 1630 mylonitic marbles and carbonate breccias from a Mesozoic Pyrenean palaeomargin
 1631 (Lherz area, North Pyrenean, France). *Comptes rendus - Geosci.* 348, 290–300.
 1632 <https://doi.org/10.1016/j.crte.2015.11.004>

1633 Lagabrielle, Y., Labaume, P., De Saint Blanquat, M., 2010. Mantle exhumation, crustal
 1634 denudation, and gravity tectonics during Cretaceous rifting in the Pyrenean realm (SW
 1635 Europe): Insights from the geological setting of the Iherzolite bodies. *Tectonics* 29, 1–
 1636 26. <https://doi.org/10.1029/2009TC002588>
 1637 Land, L.S., 1998. Failure to precipitate dolomite at 25 °C from dilute solution despite 1000-
 1638 fold oversaturation after 32 years. *Aquat. Geochemistry* 4, 361–368.
 1639 <https://doi.org/10.1023/A:1009688315854>
 1640 Land, L.S., 1985. The origin of massive dolomite. *J. Geol. Educ.* 33, 112–125.
 1641 <https://doi.org/10.5408/0022-1368-33.2.112>
 1642 Land, L.S., 1980. The isotopic and trace element geochemistry of dolomite: The state of the
 1643 art. *Soc. Econ. Paleontol. Mineral.* 28, 87–110.
 1644 Land, L.S., 1973. Contemporaneous dolomitization of Middle Pleistocene reefs by meteoric
 1645 water, North Jamaica. *Bull. Mar. Sci.* 23, 64–92.
 1646 Land, L.S., Prezbindowski, D.R., 1981. The origin and evolution of saline formation water,
 1647 lower cretaceous carbonates, South-Central Texas, U.S.A. *Dev. Water Sci.* 54, 51–74.
 1648 [https://doi.org/10.1016/S0167-5648\(08\)70595-1](https://doi.org/10.1016/S0167-5648(08)70595-1)
 1649 Lenoble, J.-L., 1992. Les plates-formes carbonatées ouest-pyrénéennes du Dogger à
 1650 l'Albien : Stratigraphie séquentielle et évolution géodynamique. Université Paul Sabatier
 1651 de Toulouse (Sciences).
 1652 Lenoble, J.-L., Canérot, J., 1992. La lame extrusive de Pont Suzon (Zone Nord-Pyrénéenne
 1653 en Vallée d'Aspe) : reprise pyrénéenne d'une ride diapirique transverse d'âge crétacé.
 1654 *C. R. Acad. Sc. Paris* 314, 387–391.
 1655 Lescoutre, R., Tugend, J., Brune, S., Masini, E., Manatschal, G., 2019. Thermal Evolution of
 1656 Asymmetric Hyperextended Magma-Poor Rift Systems: Results From Numerical
 1657 Modeling and Pyrenean Field Observations, *Geochemistry, Geophysics, Geosystems*.
 1658 <https://doi.org/10.1029/2019GC008600>
 1659 Longstaffe, F.J., 1987. Stable isotope studies of diagenetic processes. In *Stable isotope*
 1660 *geochemistry of low temperature processes. Short Course Handb.* 13, 187–257.

1661 Lopez-Horgue, M.A., Iriarte, E., Schröder, S., Fernandez-Mendiola, P.A., Caline, B.,
 1662 Corneyllie, H., Frémont, J., Sudrie, M., Zerti, S., 2010. Structurally controlled
 1663 hydrothermal dolomites in Albian carbonates of the Ason valley, Basque Cantabrian
 1664 Basin, Northern Spain. *Mar. Pet. Geol.* 27, 1069–1092.
 1665 <https://doi.org/10.1016/j.marpetgeo.2009.10.015>
 1666 Lovering, T.S., 1969. The origin of hydrothermal and low temperature dolomite. *Econ. Geol.*
 1667 64, 743–754. <https://doi.org/10.2113/gsecongeo.64.7.743>
 1668 Lukoczki, G., Haas, J., Gregg, J.M., Machel, H.G., Kele, S., John, C.M., 2018. Multi-phase
 1669 dolomitization and recrystallization of Middle Triassic shallow marine-peritidal
 1670 carbonates from the Mecsek Mts. (SW Hungary), as inferred from petrography, carbon,
 1671 oxygen, strontium and clumped isotope data. *Mar. Pet. Geol.*
 1672 <https://doi.org/10.1016/j.marpetgeo.2018.12.004>
 1673 Machel, H.G., 2004. Concepts and models of dolomitization: a critical reappraisal. *Geol. Soc.*
 1674 *London Spec. Publ.* 235, 7–63. <https://doi.org/10.1144/GSL.SP.2004.235.01.02>
 1675 Machel, H.G., Cavell, P.A., 1999. Low-flux, tectonically-induced squeegee fluid flow (“hot
 1676 flash”) into the Rocky Mountain Foreland Basin. *Bull. Can. Pet. Geol.* 47, 510–533.
 1677 Machel, H.G., Mountjoy, E.W., 1986. Chemistry and Environments of Dolomitization - A
 1678 Reappraisal. *Earth Sci. Rev.* 23, 175–222. [https://doi.org/10.1016/0012-8252\(86\)90017-](https://doi.org/10.1016/0012-8252(86)90017-6)
 1679 6
 1680 Martín-Martín, J.D., Travé, A., Gomez-Rivas, E., Salas, R., Sizun, J.-P., Vergés, J., Corbella,
 1681 M., Stafford, S.L., Alfonso, P., 2015. Fault-controlled and stratabound dolostones in the
 1682 Late Aptian--earliest Albian Benassal Formation (Maestrat Basin, E Spain): Petrology
 1683 and geochemistry constrains. *Mar. Pet. Geol.* 65, 83–102.
 1684 <https://doi.org/10.1016/j.marpetgeo.2015.03.019>
 1685 Masini, E., Manatschal, G., Tugend, J., Mohn, G., Flament, J.-M., 2014. The tectono □
 1686 sedimentary evolution of a hyper □ extended rift basin: the example of the Arzacq –
 1687 Mauléon rift system (Western Pyrenees, SW France). *Int. J. Earth Sci.* 103, 1569–1596.
 1688 <https://doi.org/10.1007/s00531-014-1023-8>

1689 McArthur, J.M., Howarth, R.J., Bailey, T.R., 2001. Strontium Isotope Stratigraphy : LOWESS
 1690 Version 3 : Best Fit to the Marine Sr-Isotope Curve for 0 – 509 Ma and Accompanying
 1691 Look-up Table for Deriving Numerical Age. *J. Geol.* 109, 155–170.
 1692 McHargue, T.R., Price, R.C., 1982. Dolomite from Clay in Argillaceous or Shale-Associated
 1693 Marine Carbonates. *J. Sediment. Petrol.* 52, 873–886.
 1694 Mello, U.T., Karner, G.D., Anderson, R.N., 1995. Role of salt in restraining the maturation of
 1695 subsalt source rocks. *Mar. Pet. Geol.* 12, 697–716. [https://doi.org/10.1016/0264-](https://doi.org/10.1016/0264-8172(95)93596-V)
 1696 [8172\(95\)93596-V](https://doi.org/10.1016/0264-8172(95)93596-V)
 1697 Montanez, I.P., 1994. Late diagenetic dolomitization of Lower Ordovician, Upper Knox
 1698 carbonates: a record of the hydrodynamic evolution of the southern Appalachian Basin.
 1699 *Am. Assoc. Pet. Geol. Bull.* 78, 1210–1239. [https://doi.org/10.1306/a25feab3-171b-](https://doi.org/10.1306/a25feab3-171b-11d7-8645000102c1865d)
 1700 [11d7-8645000102c1865d](https://doi.org/10.1306/a25feab3-171b-11d7-8645000102c1865d)
 1701 Moore, C., Wade, W.J., 2013. Carbonate diagenesis: Introduction and tools. *Dev.*
 1702 *Sedimentol.* 67, 67–89. <https://doi.org/10.1016/B978-0-444-53831-4.00005-7>
 1703 Moragas, M., Baqués, V., Travé, A., Martín-Martín, J.D., Saura, E., Messenger, G., Hunt, D.,
 1704 Vergés, J., 2020. Diagenetic evolution of lower Jurassic platform carbonates flanking
 1705 the Tazoult salt wall (Central High Atlas, Morocco). *Basin Res.* 32, 546–566.
 1706 <https://doi.org/10.1111/bre.12382>
 1707 Morrow, D.W., 1982. Descriptive field classification of sedimentary and diagenetic breccia
 1708 fabrics in carbonate rocks. *Bull. Can. Pet. Geol.* 30, 227–229.
 1709 Mountjoy, E.W., Halim-Dihardja, M.K., 1991. Multiple phase fracture and fault-controlled
 1710 burial dolomitization, Upper Devonian Wabamun Group, Alberta. *J. Sediment. Petrol.*
 1711 61, 590–612.
 1712 Mountjoy, E.W., Qing, H., McNutt, R.H., 1992. Strontium isotopic composition of Devonian
 1713 dolomites, Western Canada Sedimentary Basin: significance of sources of dolomitizing
 1714 fluids. *Appl. Geochemistry* 7, 59–75. [https://doi.org/10.1016/0883-2927\(92\)90015-U](https://doi.org/10.1016/0883-2927(92)90015-U)
 1715 Mouthereau, F., Filleaudeau, P.Y., Vacherat, A., Pik, R., Lacombe, O., Fellin, M.G.,
 1716 Castelltort, S., Christophoul, F., Masini, E., 2014. Placing limits to shortening evolution

1717 in the Pyrenees: Role of margin architecture and implications for the Iberia/Europe
 1718 convergence. *Tectonics* 33, 2283–2314. <https://doi.org/10.1002/2014TC003663>

1719 Mozafari, M., Swennen, R., Balsamo, F., El Desouky, H., Storti, F., Taberner, C., Desouky,
 1720 H. El, Storti, F., Taberner, C., 2019. Fault-controlled dolomitization in the Montagna dei
 1721 Fiori Anticline (Central Apennines, Italy): Record of a dominantly pre-orogenic fluid
 1722 migration. *Solid Earth Discuss.* 10, 1355–1383. <https://doi.org/10.5194/se-2018-136>

1723 Muñoz, J.A., 1992. Evolution of a continental collision belt: ECORS-Pyrenees crustal
 1724 balanced cross-section. *Thrust Tectonics* 235–246. [https://doi.org/10.1007/978-94-011-](https://doi.org/10.1007/978-94-011-3066-0_21)
 1725 [3066-0_21](https://doi.org/10.1007/978-94-011-3066-0_21)

1726 Nader, F.H., López-Horgue, M.A., Shah, M.M., Dewit, J., Garcia, D., Swennen, R., Iriarte, E.,
 1727 Muchez, P., Caline, B., 2012. Les dolomies hydrothermales de Ranero (Albien, Vallée
 1728 de la Karrantza, nord-ouest de l’Espagne): Conséquences sur les modèles génétiques.
 1729 *Oil Gas Sci. Technol.* 67, 9–29. <https://doi.org/10.2516/ogst/2011165>

1730 Nader, F.H., Swennen, R., 2004. The hydrocarbon potential of Lebanon: New insights from
 1731 regional correlations and studies of Jurassic dolomitization. *J. Pet. Geol.* 27, 253–275.
 1732 <https://doi.org/10.1111/j.1747-5457.2004.tb00058.x>

1733 Nader, F.H., Swennen, R., Ellam, R.M., 2004. Reflux stratabound dolostone and
 1734 hydrothermal volcanism-associated dolostone: A two-state dolomitization model
 1735 (Jurassic, Lebanon). *Sedimentology* 51, 339–360. [https://doi.org/10.1111/j.1365-](https://doi.org/10.1111/j.1365-3091.2004.00629.x)
 1736 [3091.2004.00629.x](https://doi.org/10.1111/j.1365-3091.2004.00629.x)

1737 Oliver, J., 1986. Fluids expelled tectonically from orogenic belts: their role in hydrocarbon
 1738 migration and other geologic phenomena. *Geology* 14, 99–102.
 1739 [https://doi.org/10.1130/0091-7613\(1986\)14<99:FETFOB>2.0.CO;2](https://doi.org/10.1130/0091-7613(1986)14<99:FETFOB>2.0.CO;2)

1740 Pedrosa, E.T., Putnis, C. V., Putnis, A., 2016. The pseudomorphic replacement of marble by
 1741 apatite: The role of fluid composition. *Chem. Geol.* 425, 1–11.
 1742 <https://doi.org/10.1016/j.chemgeo.2016.01.022>

1743 Péré, P., 1989. La formation dolomitique du Mailh Arrouy Dogger Kimméridgien inférieur
 1744 (Etude à l’affleurement dans les Chaînon béarnais du réservoir gazéifère de Meillon).

1745 Pyrénées occidentales (France). Sédimentation, Structuration, Diagenèses. Université
 1746 de Pau et des Pays de l'Adour.

1747 Péré, P., 1987. Dolomitisations et diagenèses successives avec passage au
 1748 métamorphisme: dolomies callovo-oxfordiennes des Pyrénées occidentales, France. C.
 1749 R. Acad. Sc. Paris 305, 391–395.

1750 Peterson, K., Lerche, I., 1995. Quantification of thermal anomalies in sediments around salt
 1751 structures. *Geothermics* 24, 253–268.

1752 Pinto, V.H., Manatschal, G., Karpoff, A.M., Ulrich, M., Viana, A.R., 2017. Seawater storage
 1753 and element transfer associated with mantle serpentinization in magma-poor rifted
 1754 margins: A quantitative approach. *Earth Planet. Sci. Lett.* 459, 227–237.
 1755 <https://doi.org/10.1016/j.epsl.2016.11.023>

1756 Piper, D.Z., 1974. Rare earth elements in the sedimentary cycle: A summary. *Chem. Geol.*
 1757 14, 285–304. [https://doi.org/10.1016/0009-2541\(74\)90066-7](https://doi.org/10.1016/0009-2541(74)90066-7)

1758 Puigdefàbregas, C., Souquet, P., 1986. Tecto-sedimentary cycles and depositional
 1759 sequences of the Mesozoic and Tertiary from the Pyrenees. *Tectonophysics* 129, 173–
 1760 203. [https://doi.org/10.1016/0040-1951\(86\)90251-9](https://doi.org/10.1016/0040-1951(86)90251-9)

1761 Putnis, A., 2009. Mineral replacement reactions. *Rev. Mineral. Geochemistry* 70, 87–124.
 1762 <https://doi.org/10.2138/rmg.2009.70.3>

1763 Putnis, A., 2002. Mineral replacement reactions: from macroscopic observations to
 1764 microscopic mechanisms. *Mineral. Mag.* 66, 689–708.
 1765 <https://doi.org/10.1180/0026461026650056>

1766 Quesnel, B., Boiron, M.-C., Cathelineau, M., Truche, L., Rigaudier, T., Bardoux, G., Agrinier,
 1767 P., De Saint Blanquat, M., Masini, E., Gaucher, E.C., 2019. Nature and Origin of
 1768 Mineralizing Fluids in Hyperextensional Systems: The Case of Cretaceous Mg
 1769 Metasomatism in the Pyrenees. *Geofluids*. <https://doi.org/10.1155/2019/7213050>

1770 Railsback, L.B., Hood, E.C., 2001. A survey of multi-stage diagenesis and dolomitization of
 1771 Jurassic limestones along a regional shelf-to-basin transect in the Ziz Valley, Central
 1772 High Atlas Mountains, Morocco. *Sediment. Geol.* 139, 285–317.

1773 [https://doi.org/10.1016/S0037-0738\(00\)00164-0](https://doi.org/10.1016/S0037-0738(00)00164-0)

1774 Renard, S., Pironon, J., Sterpenich, J., Lescanne, M., Gaucher, E.C., 2018. Diagenesis in
 1775 Mesozoic carbonate rocks in the North Pyrénées (France) from mineralogy and fluid
 1776 inclusion analysis: example of ROusse reservoir and caprock. *Chem. Geol.*
 1777 <https://doi.org/10.1016/j.chemgeo.2018.06.017>

1778 Révillon, S., Jouet, G., Bayon, G., Rabineau, M., Dennielou, B., Hémond, C., Berné, S.,
 1779 2011. The provenance of sediments in the Gulf of Lions, western Mediterranean Sea.
 1780 *Geochemistry, Geophys. Geosystems* 12. <https://doi.org/10.1029/2011GC003523>

1781 Roberts, N.M.W., Rasbury, E.T., Parrish, R.R., Smith, C.J., Horstwood, M.S.A., Condon,
 1782 D.J., 2017. A calcite reference material for LA-ICP-MS U-Pb geochronology.
 1783 *Geochemistry, Geophys. Geosystems* 18, 2807–2814.
 1784 <https://doi.org/10.1002/2016GC006784>.Received

1785 Rollion-Bard, C., Blamart, D., Cuif, J.P., Juillet-Leclerc, A., 2003. Microanalysis of C and O
 1786 isotopes of azooxanthellate and zooxanthellate corals by ion microprobe. *Coral Reefs*
 1787 22, 405–415. <https://doi.org/10.1007/s00338-003-0347-9>

1788 Rollion-Bard, C., Marin-Carbonne, J., 2011. Determination of SIMS matrix effects on oxygen
 1789 isotopic compositions in carbonates. *J. Anal. At. Spectrom.* 26, 1285–1289.
 1790 <https://doi.org/10.1039/c0ja00213e>

1791 Rosenbaum, G., Lister, G.S., Duboz, C., 2002. Relative motions of Africa, Iberia and Europe
 1792 during Alpine orogeny. *Tectonophysics* 359, 117–129.

1793 Rosenbaum, J., Sheppard, S.M.F., 1986. An isotopic study of siderites dolomites and
 1794 ankerites at high temperatures. *Geochim. Cosmochim. Acta* 50, 1147–1150.
 1795 [https://doi.org/10.1016/0016-7037\(86\)90396-0](https://doi.org/10.1016/0016-7037(86)90396-0)

1796 Roure, F., Andriessen, P., Callot, J.P., Faure, J.L., Ferket, H., Gonzales, E., Guilhaumou, N.,
 1797 Lacombe, O., Malandain, J., Sassi, W., Schneider, F., Swennen, R., Vilasi, N., 2010.
 1798 The use of palaeo-thermo-barometers and coupled thermal, fluid flow and pore-fluid
 1799 pressure modelling for hydrocarbon and reservoir prediction in fold and thrust belts.
 1800 *Geol. Soc. Spec. Publ.* 348, 87–114. <https://doi.org/10.1144/SP348.6>

1801 Roure, F., Swennen, R., Schneider, F., Faure, J.L., Ferket, H., Guilhaumou, N., 2005.
 1802 Incidence and Importance of Tectonics and Natural Fluid Migration on Reservoir
 1803 Evolution in Foreland Fold-and-Thrust Belts. *Oil Gas Sci. Technol. - Rev. IFP* 60, 67–
 1804 106.

1805 Rustichelli, A., Iannace, A., Tondi, E., Di Celma, C., Cilona, A., Giorgioni, M., Parente, M.,
 1806 Girundo, M., Invernizzi, C., 2017. Fault-controlled dolomite bodies as palaeotectonic
 1807 indicators and geofluid reservoirs: New insights from Gargano Promontory.
 1808 *Sedimentology* 64, 1871–1900. <https://doi.org/10.1111/ijlh.12426>

1809 Salardon, R., Carpentier, C., Bellahsen, N., Pironon, J., France-Lanord, C., 2017.
 1810 Interactions between tectonics and fluid circulations in an inverted hyper-extended
 1811 basin: Example of mesozoic carbonate rocks of the western North Pyrenean Zone
 1812 (Chaînons Béarnais, France). *Mar. Pet. Geol.* 80, 563–586.
 1813 <https://doi.org/10.1016/j.marpetgeo.2016.11.018>

1814 Saspiturry, N., 2019. Evolution sédimentaire, structurale et thermique d'un rift hyper-aminci:
 1815 de l'héritage post-hercynien à l'inversion alpine Exemple du bassin de Mauléon
 1816 (Pyrénées). Université Bordeaux Montaigne.

1817 Saspiturry, N., Razin, P., Baudin, T., Serrano, O., Issautier, B., Lasseur, E., Allanic, C.,
 1818 Thinon, I., Leleu, S., 2019. Symmetry vs asymmetry of a hyper-thinned rift: Example of
 1819 the Mauleon Basin. *Mar. Pet. Geol.* 104, 86–105.

1820 Scholle, P.A., Ulmer-Scholle, D.S., 2003. A Color Guide Petrography of carbonate rocks:
 1821 Grains, textures, porosity, diagenesis.

1822 Selig, F., Wallick, G.C., 1966. Temperature distribution in salt domes and surrounding
 1823 sediments. *Geophysics* XXXI, 346–361.

1824 Shah, M.M., Nader, F.H., Dewit, J., Swennen, R., Garcia, D., 2010. Fault-related
 1825 hydrothermal dolomites in Cretaceous carbonates (Cantabria, northern Spain): Results
 1826 of petrographic, geochemical and petrophysical studies. *Bull. la Soc. Geol. Fr.* 181,
 1827 391–407. <https://doi.org/10.2113/gssgfbull.181.4.391>

1828 Sharp, I., Gillespie, P., Morsalnezhad, D., Taberner, C., Karpuz, R., Vergés, J., Horbury, A.,

1829 Pickard, N., Garland, J., Hunt, D., 2010. Stratigraphic architecture and fracture-
 1830 controlled dolomitization the Cretaceous Khami and Bangestan groups: An outcrop case
 1831 study, Zagros Mountains, Iran. *Geol. Soc. Spec. Publ.* 329, 343–396.
 1832 <https://doi.org/10.1144/SP329.14>
 1833 Sibley, D.F., Nordeng, S.H., Borkowski, M.L., 1994. Dolomitization kinetics in hydrothermal
 1834 bombs and natural settings. *J. Sediment. Res. A Sediment. Petrol. Process.* 630–637.
 1835 <https://doi.org/10.1306/d4267e29-2b26-11d7-8648000102c1865d>
 1836 Sibuet, J.-C., Srivastava, S.P., Spakman, W., 2004. Pyrenean orogeny and plate kinematics.
 1837 *J. Geophys. Res.* 109, 1–18. <https://doi.org/10.1029/2003JB002514>
 1838 Spencer-Cervato, C., Mullis, J., 1992. Chemical study of tectonically controlled hydrothermal
 1839 dolomitization: an example from the Lessini mountains, Italy. *Geol. Rundschau* 81, 347–
 1840 370. <https://doi.org/10.1007/BF01828603>
 1841 Stoakes, F., 1987. Fault controlled dolomitization of the Wabamum Group, Tangle Field,
 1842 Peace River Arch, Alberta. *Devonian Lithofacies Reserv. Styles Alberta 13th CSPG*
 1843 *Core Conf. Disp.*
 1844 Teixell, A., Labaume, P., Ayarza, P., Espurt, N., de Saint Blanquat, M., Lagabrielle, Y., 2018.
 1845 Crustal structure and evolution of the Pyrenean-Cantabrian belt: A review and new
 1846 interpretations from recent concepts and data. *Tectonophysics* 724–725, 146–170.
 1847 <https://doi.org/10.1016/j.tecto.2018.01.009>
 1848 Teixell, A., Labaume, P., Lagabrielle, Y., 2016. The crustal evolution of the west-central
 1849 Pyrenees revisited: Inferences from a new kinematic scenario. *Comptes Rendus -*
 1850 *Geosci.* 348, 257–267. <https://doi.org/10.1016/j.crte.2015.10.010>
 1851 Tortola, M., Al-Aasm, I.S., Crowe, R., 2020. Diagenetic pore fluid evolution and
 1852 dolomitization of the Silurian and Devonian carbonates, Huron Domain of southwestern
 1853 Ontario: Petrographic, geochemical and fluid inclusion evidence. *Minerals* 10.
 1854 <https://doi.org/10.3390/min10020140>
 1855 Tostevin, R., Shields, G.A., Tarbuck, G.M., He, T., Clarkson, M.O., Wood, R.A., 2016.
 1856 Effective use of cerium anomalies as a redox proxy in carbonate-dominated marine

1857 settings. *Chem. Geol.* 438, 146–162. <https://doi.org/10.1016/j.chemgeo.2016.06.027>

1858 Tugend, J., Manatschal, G., Kuszniir, N.J., 2015. Spatial and temporal evolution of
 1859 hyperextended rift systems: Implication for the nature, kinematics, and timing of the
 1860 Iberian-European plate boundary. *Geology* 43, 15–18.
 1861 <https://doi.org/10.1130/G36072.1>

1862 Tugend, J., Manatschal, G., Kuszniir, N.J., Masini, E., Mohn, G., Thion, I., 2014. Formation
 1863 and deformation of hyperextended rift systems: Insights from rift domain mapping in the
 1864 Bay of Biscay-Pyrenees. *Tectonics* 33, 1239–1276.
 1865 <https://doi.org/10.1002/2014TC003529>.Received

1866 Vacherat, A., Mouthereau, F., Pik, R., Bellahsen, N., Gautheron, C., Bernet, M., Daudet, M.,
 1867 Balansa, J., Tibari, B., Pinna Jamme, R., Radal, J., 2016. Rift-to-collision transition
 1868 recorded by tectonothermal evolution of the northern Pyrenees. *Tectonics* 35, 907–933.
 1869 <https://doi.org/10.1002/2015TC004016>

1870 Vacherat, A., Mouthereau, F., Pik, R., Bernet, M., Gautheron, C., Masini, E., Le Pourhiet, L.,
 1871 Tibari, B., Lahfid, A., 2014. Thermal imprint of rift-related processes in orogens as
 1872 recorded in the Pyrenees. *Earth Planet. Sci. Lett.* 408, 296–306.
 1873 <https://doi.org/10.1016/j.epsl.2014.10.014>

1874 Veizer, J., Ala, D., Azmy, K., Bruckschen, P., Buhl, D., Bruhn, F., Carden, G.A.F., Diener, A.,
 1875 Ebner, S., Godderis, Y., Jasper, T., Korte, C., Pawellek, F., Podlaha, O.G., Strauss, H.,
 1876 1999. $^{87}\text{Sr}/^{86}\text{Sr}$, $\delta^{13}\text{C}$ and $\delta^{18}\text{O}$ evolution of Phanerozoic seawater. *Chem. Geol.* 161,
 1877 59–88.

1878 Veizer, J., Prokoph, A., 2015. Temperatures and oxygen isotopic composition of Phanerozoic
 1879 oceans. *Earth Sci. Rev.* 146, 92–104. <https://doi.org/10.1016/j.earscirev.2015.03.008>

1880 Vergés, J., Millán, H., Roca, E., Muñoz, J.A., Marzo, M., Cirés, J., Bezemer, T. Den,
 1881 Zoetemeijer, R., Cloetingh, S., 1995. Eastern Pyrenees and related foreland basins:
 1882 pre-, syn- and post-collisional crustal-scale cross-sections. *Mar. Pet. Geol.* 12, 903–915.
 1883 [https://doi.org/10.1016/0264-8172\(95\)98854-X](https://doi.org/10.1016/0264-8172(95)98854-X)

1884 Vermeesch, P., 2020. Unifying the U–Pb and Th–Pb methods: joint isochron regression and

1885 common Pb correction. *Geochronology* 2, 119–131. [https://doi.org/10.5194/gchron-2-](https://doi.org/10.5194/gchron-2-119-2020)
 1886 119-2020
 1887 Vermeesch, P., 2018. IsoplotR: A free and open toolbox for geochronology. *Geosci. Front.* 9,
 1888 1479–1493. <https://doi.org/10.1016/j.gsf.2018.04.001>
 1889 Vilasi, N., Malandain, J., Barrier, L., Callot, J.-P., Amrouch, K., Guilhaumou, N., Lacombe,
 1890 O., Muska, K., Roure, F., Swennen, R., 2009. From outcrop and petrographic studies to
 1891 basin-scale fluid flow modelling: The use of the Albanian natural laboratory for
 1892 carbonate reservoir characterisation. *Tectonophysics* 474, 367–392.
 1893 <https://doi.org/10.1016/j.tecto.2009.01.033>
 1894 Warren, J., 2000. Dolomite: occurrence, evolution and economically important associations.
 1895 *Earth-Science Rev.* 52, 1–81. [https://doi.org/10.1016/S0012-8252\(00\)00022-2](https://doi.org/10.1016/S0012-8252(00)00022-2)
 1896 Wendte, J., Chi, G., Al-Aasm, I.S., Sargent, D., 2009. Fault/fracture controlled hydrothermal
 1897 dolomitization and associated diagenesis of the Upper Devonian Jean Marie Member
 1898 (Redknife Formation) in the July Lake area of northeastern British Columbia. *Bull. Can.*
 1899 *Pet. Geol.* 57, 275–322. <https://doi.org/10.2113/gscpgbull.57.3.275>
 1900 Wendte, J., Dravis, J.J., Stasiuk, L.D., Qing, H., Moore, S.L.O., Ward, G., 1998. High-
 1901 temperature saline (thermoflux) dolomitization of Devonian Swan Hills platform and
 1902 bank carbonates, Wild River area, west-central Alberta. *Bull. Can. Pet. Geol.* 46, 210–
 1903 265.
 1904 White, T., Al-Aasm, I.S., 1997. Hydrothermal dolomitization of the Mississippian Upper
 1905 Debolt Formation, Sikanni gas field, northeastern British Columbia, Canada. *Bull. Can.*
 1906 *Pet. Geol.* 45, 297–316.
 1907 Wierzbicki, R., Dravis, J.J., Al-Aasm, I.S., Harland, N., 2006. Burial dolomitization and
 1908 dissolution of Upper Jurassic Abenaki platform carbonates, Deep Panuke reservoir,
 1909 Nova Scotia, Canada. *Am. Assoc. Pet. Geol. Bull.* 90, 1843–1861.
 1910 <https://doi.org/10.1306/03200605074>
 1911 Wilkinson, M., Crowley, S.F., Marshall, J.D., 1992. Model for the evolution of oxygen isotope
 1912 ratios in the pore fluids of mudrocks during burial. *Mar. Pet. Geol.* 9, 98–105.

- 1913 Wright, P. V., 1992. A revised classification of limestones. *Sediment. Geol.* 76, 177–185.
- 1914 [https://doi.org/10.1016/0037-0738\(92\)90082-3](https://doi.org/10.1016/0037-0738(92)90082-3)
- 1915 Ye, N., Zhang, S., Qing, H., Li, Y., Huang, Q., Liu, D., 2019. Dolomitization and its impact on
- 1916 porosity development and preservation in the deeply burial Lower Ordovician carbonate
- 1917 rocks of Tarim Basin, NW China. *J. Pet. Sci. Eng.* 182.
- 1918 <https://doi.org/10.1016/j.petrol.2019.106303>
- 1919 Zenger, D.H., Dunham, J.B., 1980. Concept and models of dolomitization. *Spec. Publ. Soc.*
- 1920 *Eng. Petrol. Mineral.* 28, 1–9.
- 1921 Zhang, J., Hu, W., Qian, Y., Wang, X., Cao, J., Zhu, J., Li, Q., Xie, X., 2009. Formation of
- 1922 saddle dolomites in Upper Cambrian carbonates, western Tarim Basin (northwest
- 1923 China): Implications for fault-related fluid flow. *Mar. Pet. Geol.* 26, 1428–1440.
- 1924 <https://doi.org/10.1016/j.marpetgeo.2009.04.004>
- 1925 Ziegler, P.A., Cloetingh, S., 2004. Dynamic processes controlling evolution of rifted basins.
- 1926 *Earth-Science Rev.* 64, 1–50. [https://doi.org/10.1016/S0012-8252\(03\)00041-2](https://doi.org/10.1016/S0012-8252(03)00041-2)
- 1927